

國立臺灣大學工學院機械工程學系

博士論文

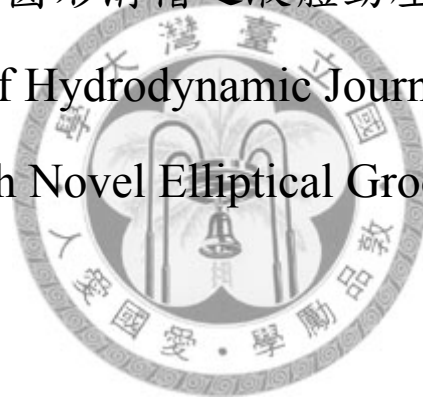
Department of Mechanical Engineering

College of Engineering

National Taiwan University

Ph.D. Dissertation

含新型橢圓形溝槽之液體動壓軸承分析
Analysis of Hydrodynamic Journal Bearings
with Novel Elliptical Grooves



陳建佑

Chien-Yu Chen

指導教授：顏瑞和 博士

Advisor: Ruey-Hor Yen, Ph.D.

中華民國 九十九 年 一 月

January, 2010



國立臺灣大學博士學位論文
口試委員會審定書
含新型橢圓形溝槽之液體動壓軸承分析
Analysis of Hydrodynamic Journal Bearings
with Novel Elliptical Grooves

本論文係陳建佑君 (D93522036) 在國立臺灣大學機械工程學系完成之博士學位論文，於民國 99 年 1 月 26 日承下列考試委員審查通過及口試及格，特此證明

口試委員：

顏 瑞 和 (簽名)

蘇 侃 (指導教授)

楊 天 祥

王 興 華

劉 正 良

系 主 任

張 所 鈞 (簽名)

誌謝

首先感謝恩師 顏瑞和教授多年的指導，老師治學嚴謹，總在辦公室做研究且不辭辛勞的指導，使學生受益匪淺。當我研究遇到瓶頸的時候，能適時的給予建議，並耐心的等待我的實驗結果。在顏老師的指導之下，學到很多論文寫作的方法，及培養執行計劃的能力。感謝顏老師對論文與投稿文章花了很多時間修改，增加其可讀性與重要性，並提供英文編修。尤其是對於本論文初稿，可說是不眠不休的修改，在此由衷的感謝。此外，更提供實驗室的豐富軟硬體資源讓我們學習。日常生活的顏老師是博學多聞，在登山領域十分專業，多次帶領實驗室同學們出遊，增長我們的見聞。

論文定稿之際，承蒙 蘇侃教授、劉正良教授、王興華教授、楊天祥教授應允擔任學生的口試委員，惠予本論文在實務上以及理論上寶貴的建議，使本論文更佳完善。在此致上深深的謝意。

感謝實驗室學長張珈進、鄭敬樺，以及同學陳任昇、洪立昕、曾裕博、李奇霖、陳彥淙、林祺峰、簡志偉、蘇炯彰、陳泰維、黃坤、黃柏銓、王彥博、王忠義、吳金瑞、黃立翔、許庭耀、張劭璋、鄭兆偉在生活與研究上的協助與分享。感謝我多年的好友，材料所的方彥翔博士在生活上的幫忙與投稿經驗的分享。感謝張天立博士在我博士生活中資格考的經驗分享與持續的鼓勵。博士班期間一路考驗重重，但有你們的關心與支持，使我的研究生生活溫暖許多。

最後，將本文的成果獻給日日辛勞的父母，感謝父母的養育之恩與關心，讓我擁有一個衣食無虞的環境與健康的身體，使我能專心致力於求學之路。感謝哥哥建宇、建璋在我離家時，代盡孝道。感謝未婚妻佩琪與我分享研究生活的酸甜苦辣，尤其是研究不順利時，成為我心靈的避風港。因為有妳的支持與包容，使我能後顧之憂地投入許多時間在研究中。感謝上天給我許多機會，讓我做了許多想做的事。希望有朝一日能拋磚引玉，對社會有所回饋與貢獻。



摘要

本文提出一種新的橢圓溝槽設計，以改善傳統含人字形溝槽頸軸承的性能。文中的第一部分，先以寬頻元素法為基礎，發展可求解含人字形溝槽頸軸承的壓力分佈與動態係數的數值程式。程式中考慮了溝槽與溝岸交接的界面，以質量守恆處理液膜不連續的問題。此外，程式擁有處理曲線溝槽形狀的彈性。結果顯示，程式解出的負載，比其他文獻的數值結果更準確。當空蝕現象發生時，採用溝槽不連續的質量守恆搭配 Elrod 算則處理空蝕現象，可以進一步改善在高偏心比之負載準確度。

本文的第二部分，提出含橢圓溝槽之新形狀的軸承，並使用上述發展的數值程式，分析其性能。橢圓溝槽軸承的負載、穩定性、洩漏量與傳統人字形溝槽軸承比較，結果顯示，本文提出的橢圓形溝槽擁有高徑向力、高負載、和低洩漏量。接著，本文找出軸承運轉時，最佳化溝槽參數，使軸承有最大的徑向力。最後，本文比較人字形、四邊溝槽、八邊溝槽、及橢圓形溝槽軸承表面的負載分布。以說明橢圓形溝槽的設計，如何增加負載。橢圓形溝槽軸承在軸向的負載分布，較人字形溝槽軸承均勻。在軸承中央處較人字形溝槽低的負載，會被軸承兩端較高的負載抵銷，於是達到較人字形溝槽高的負載。

本文的最後一部分，將橢圓形溝槽應用於可反轉的軸承上，以改善可反轉人字形溝槽的負載，並以數值方法探討性能改善的程度。橢圓溝槽可反轉軸承的負載、穩定性、耗能與傳統人字形溝槽可反轉軸承比較。比較結果顯示，橢圓形溝槽可反轉軸承的負載較高，耗能較低。橢圓溝槽可反轉軸承的高壓區不只在正轉的壓

力產生區，也在反轉需要的壓力恢復區產生。此外，比較人字形、及橢圓形溝槽可反轉軸承表面的負載分布。以說明橢圓形溝槽的設計，如何增加負載。最後，在徑向剛性係數為考量的最佳化參數之下，橢圓形溝槽可反轉軸承的穩定性比人字形溝槽可反轉軸承優異。

關鍵字:液體動壓軸承、橢圓溝槽、人字形溝槽、空蝕現象、穩定性、寬頻元素法

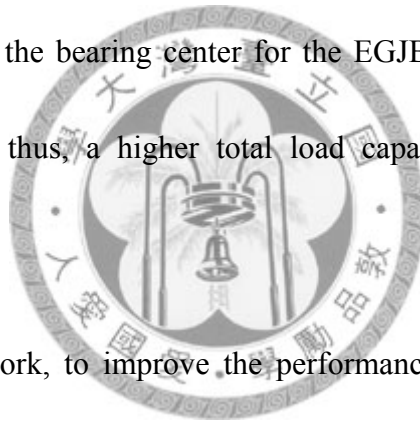


Abstract

A novel elliptical groove is proposed in this work to improve the performance of conventional journal bearings. Firstly, the present work utilizes the spectral element method to calculate the pressure distribution and dynamic coefficients of herringbone-grooved journal bearings (HGJBs), in which the thickness of the fluid film changes abruptly in the groove-ridge region. Conservation of mass is adopted to solve the problem. Additionally, the present method can be adopted for grooves with curvy geometry. It shows that for the case of HGJB, the numerical result by the present method is more accurate than the numerical results found in the literature. Furthermore, employing the present method with the Elrod's algorithm can improve the accuracy of deriving loads of HGJBs when cavitation occurs.

In the secondary part of this work, the novel elliptical grooves are proposed. This work utilizes novel elliptical grooves on a journal bearing and analyzes the characteristics of the elliptical-grooved journal bearings (EGJB) numerically. Load capacity, stability parameter, and total side leakage of the EGJB are compared with

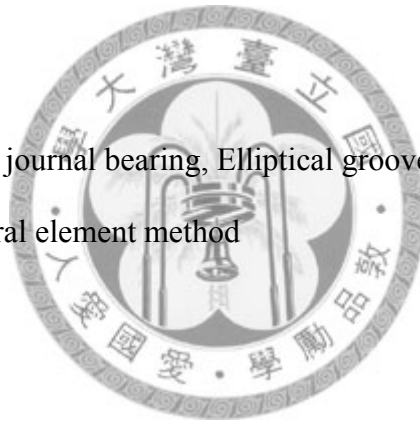
those of the HGJB. The comparison shows that the introduced EGJB have higher radial force, higher load capacity, and lower side leakage than the conventional HGJB. The optimum geometrical parameters of groove of EGJB are investigated based on the maximum radial force. Finally, the load distributions of several grooved journal bearings are compared to elucidate how elliptical grooves enhance load characteristics. The load distribution along the axial direction in EGJB is more uniform than that in the HGJB. The low load near the bearing center for the EGJB may be offset by the load away the bearing center; thus, a higher total load capacity than that of HGJB is achieved.



In the end of this work, to improve the performance of the reversible rotation grooved journal bearing (Rev-HGJB), this work utilizes elliptical grooves on a reversible rotation journal bearing (Rev-EGJB) and analyzes its characteristics numerically. Load capacity, pressure distribution, power loss, and dimensionless radial stiffness of the Rev-EGJB are compared with those of the Rev-HGJB. The comparison shows that the introduced Rev-EGJB exhibits higher load capacity and lower power loss than the Rev-HGJB. A larger high pressure region in the Rev-EGJB than that in the

Rev-HGJB is achieved not only in the pressure-generated region, but also in the pressure-restored region. Furthermore, the load distributions of the Rev-HGJB and Rev-EGJB are compared to elucidate how elliptical grooves enhance load characteristics. Ultimately, the radial stiffness of the Rev-EGJB compared with that of the Rev-HGJB with the optimum geometry is also shown to be greater; thus, the Rev-EGJB is more stable than the Rev-HGJB.

Keywords: Hydrodynamic journal bearing, Elliptical groove, Herringbone groove, Cavitation, Stability, Spectral element method



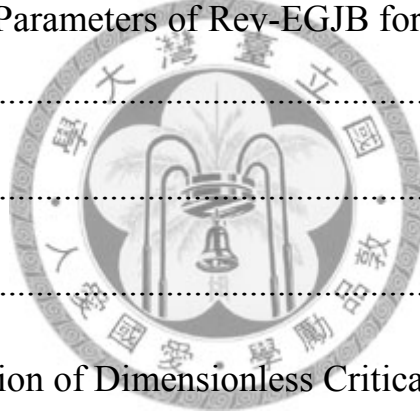


Contents

摘要	i
Abstract.....	iii
Contents	vii
List of Figures.....	x
List of Tables	xv
Nomenclature.....	xvi
1. Introduction.....	1
1-1 Current Applications of Grooved Journal Bearings.....	1
1-2 Research Needs for Groove Appearances.....	4
1-3 Stability Criteria.....	5
1-4 Cavitation Model.....	6
1-5 Analysis Methods.....	7
1-5-1 Discretization Method	7
1-5-2 Treatment at the Discontinuity of Groove-Ridge Region	9
1-6 Dissertation Outline	11
2. Governing Equations	13
2-1 Reynolds Equation.....	13
2-2 Elrod's Cavitation Algorithm.....	18
2-3 Stability Parameter.....	19
2-4 Groove Profile.....	20

3.	Numerical Method.....	23
3-1	Spatial Discretization- Spectral Element Method (SEM).....	23
3-2	Treatment in Groove-Ridge Discontinuity	30
3-2-1	For 1-D Step-Slider Bearing.....	30
3-2-2	For 2-D HGJB with Reynolds Equation.....	33
3-2-3	For 2-D HGJB with Elrod's Algorithm	36
3-3	Grid Independent Test.....	37
3-3-1	HGJB	37
3-3-2	EGJB	40
4.	Validation.....	45
4-1	Load Capacity	45
4-1-1	One-dimensional Step-Slider Bearing	45
4-1-2	Load Comparison of HGJB	47
4-1-3	Load Comparison of HGJB with Elrod's Model.....	49
4-1-4	Validation of EGJB	53
4-2	Validation of Critical Mass	56
5.	Effect of HGJB's Appearance on Stability.....	61
5-1	Effect of Change in Groove Angle on Critical mass	61
5-2	Effect of Change in Groove Depth on Critical mass	65
5-3	Effect of Change in Groove Width on Critical Mass.....	66
5-4	Efficiency of the Present Method on Critical Mass.....	67
6.	Performance Enhancement Using Elliptical Grooves.....	69
6-1	Performance of EGJB	69
6-1-1	Effect on Load Capacity	69
6-1-2	Effect on Stability	71
6-1-3	Effect on Side Leakage.....	73
6-1-4	Effect on Reducing Cavitation.....	75
6-2	Optimum Groove Parameters for Stability	78

6-3 Comparison of the Load Distribution	84
7. Performance Enhancement on Rev-EGJB.....	89
7-1 Groove Profile.....	89
7-2 Validation	91
7-3 Comparison of the Rev-EGJB and the Rev-HGJB.....	94
7-3-1 Rev-EGJB Mesh	95
7-3-2 Comparison of the Load Capacities.....	96
7-3-3 Comparison of the Pressure Distributions in the Fluid Film	99
7-4 Comparison of Power Losses.....	102
7-5 The Effect of Groove's Appearance on Radial Stiffness	103
7-6 The Optimum Parameters of Rev-EGJB for Stability	108
8. Conclusions.....	111
9. Future Work	113
References.....	A1
Appendix A Evaluation of Dimensionless Critical Mass	A5



List of Figures

Fig. 1-1-1 The reversible rotation type herringbone grooved journal bearing proposed by Kawabata et al. [6]	3
Fig. 2-1-1 Sketch of the fluid thickness for grooved bearing	13
Fig. 2-1-2 Fluid thickness in the ridge or groove regions in terms of circumferential coordinate	14
Fig. 2-4-1 Parameters of the EGJB (The grooves can be engraved on either journal or bearing surface.)	21
Fig. 3-1-1 the transformation from the local coordinate to the physical coordinate system	25
Fig. 3-1-2 The flowchart of the numerical program (solver)	29
Fig. 3-2-1 Geometry of a parallel slider bearing	31
Fig. 3-2-2 Conservation of flow rate at a groove-ridge region	35
Fig. 3-3-1 Mesh system used in the program	38
Fig. 3-3-2 Mesh system used in the program of EGJB	41
Fig. 3-3-3 Grid independent test to evaluate the load capacity of EGJB	42
Fig. 3-3-4 Grid independent test to evaluate the leakage of EGJB	43
Fig. 4-1-1 The numerical result of pressure distribution in one-dimensional slider	

bearing	47
Fig. 4-1-2 Comparison of load with studies [8, 20, 37].....	48
Fig. 4-1-3 Comparison of experimental data of reference [18] along circumference (a) axial position from centerline ($L/5D$), (b) axial position from centerline ($3L/5D$).....	50
Fig. 4-1-4 Cavitation area ratio for the Hirs' experimental case	52
Fig. 4-1-5 Pressure distributions at the axial position from the centerline $L/2D$ under various eccentricity ratios.....	53
Fig. 4-1-6 Sketch of a herringbone groove, elliptical groove, and groove with four sides.....	54
Fig. 4-1-7 Load capacities of the EGJB, HGJB, and groove journal bearing with several sides.....	55
Fig. 4-1-8 Dimensionless radial stiffness of the EGJB, HGJB, and groove journal bearing with several sides.....	56
Fig. 4-2-1 Validation of attitude angle of HGJB with Rao and Sawicki [17].....	57
Fig. 4-2-2 Comparisons of HGJBs on dynamic coefficients with Rao and Sawicki [17] at a groove angle of 70°	57
Fig. 4-2-3 Validation of dimensionless critical mass of a plain journal bearing with literature [35]	58

Fig. 4-2-4 Validation of HGJB on dimensionless critical mass	59
Fig. 5-1-1(a) Dimensionless critical mass at a groove depth ratio of 0.5.....	62
Fig. 5-1-2 (a) Dimensionless critical mass at a groove width ratio of 0.25.....	63
Fig. 6-1-1 Load capacities with various eccentricity ratios for grooved bearings	70
Fig. 6-1-2 Variations in load capacities with different eccentricity ratios for grooved journals	70
Fig. 6-1-3 Dimensionless radial stiffness of the EGJB and HGJB with various eccentricity ratios and length-diameter ratios and for a grooved bearing	72
Fig. 6-1-4 Dimensionless radial stiffness of the EGJB and HGJB with various eccentricity ratios and length-diameter ratios for grooved journals.....	73
Fig. 6-1-5(a) Dimensionless total side leakage of the EGJB and HGJB with various eccentricity ratios and length-diameter ratios for grooved journals.....	74
Fig. 6-1-6 Load of the HGJB and EGJB for a grooved journal with optimum groove parameter	76
Fig. 6-1-7 Load of the HGJB and EGJB for a grooved bearing with optimum groove parameter	77
Fig. 6-2-1(a) Dimensionless radial stiffness under a groove width ratio of 0.5 and eccentricity ratio of 0.1	80
Fig. 6-2-2(a) Dimensionless radial stiffness under a groove depth ratio of 2.0 and	

eccentricity ratio of 0.1	82
Fig. 6-3-1 The distribution of load capacity along the axial direction	85
Fig. 6-3-2 Total Side leakage of the EGJB, HGJB and grooved journal bearings with 4 and 8 sides	87
Fig. 7-1-1 The shape of the reversible rotation journal bearing with elliptical grooves	90
Fig. 7-2-1 The numerical program for the Rev-HGJB was verified using data from [6].	92
Fig. 7-2-2 The numerical program of the Rev-EGJB was validated by increasing the number of groove sides of the Rev-HGJB	94
Fig. 7-3-1 The mesh system used in the program for Rev-EGJB	96
Fig. 7-3-2 Comparison of the load capacities of the conventional HGJB, Rev-HGJB, and Rev-EGJB with the increase of the eccentricity ratio (grooved journal).....	97
Fig. 7-3-3 The load capacity of the Rev-HGJB and Rev-EGJB with grooved bearing for $L/D = 1, 2$	99
Fig. 7-3-4 The pressure distributions of fluid film of a Rev-EGJB and of a Rev-HGJB under the operating conditions in Fig. 7-3-2 ($\epsilon=0.3$)	100
Fig. 7-3-5 The load per unit length along y direction	102
Fig. 7-5-1 The influences of elliptical axis ratio of region 1 and region 2 on	

dimensionless radial stiffness 105

Fig. 7-5-2 The influences of groove depth on dimensionless radial stiffness 106

Fig. 7-5-3 The effects of groove width on dimensionless radial stiffness..... 107

Fig. 7-5-4 The effect of bearing length of region 2 on dimensionless radial stiffness108



List of Tables

Table 3-3-1 Design parameters of the HGJB.....	38
Table 3-3-2 Grid independent test on dimensionless critical mass (appendix A)at groove angle of 20°, groove depth ratio of 1.0, groove width ratio of 0.5, and at eccentricity ratio of 0.7.....	39
Table 5-4-1 The CPU time needed to obtain the load capacity of a bearing with 8 grooves on the stationary surface, at an eccentricity ratio of 0.5 for various nodal points (groove angle=40°).....	68
Table 6-1-1 The Cavitation ratio of the HGJB and EGJB for a grooved journal with optimum groove parameter.....	77
Table 6-1-2 The Cavitation ratio of the HGJB and EGJB for a grooved bearing with optimum groove parameter.....	78
Table 6-2-1 Design parameters of the EGJB.....	79
Table 7-3-1 Parameters of the Rev-GJB (grooved member rotation)	95
Table 7-4-1 Comparison of the power loss of the Rev-HGJB and Rev-EGJB.....	103
Table 7-6-1 the values of the optimum groove parameters for grooved journal	109

Nomenclature

c	clearance (m)
c_g	groove depth (m)
D	bearing diameter (m)
D_{ij}	dimensionless damping coefficient
e	eccentricity (m)
g	switch function
h	film thickness (m)
K_{ij}	dimensionless stiffness coefficient
L	length of journal bearing (m)
L_1, L_2, L_3	length of bearing of region 1, 2, 3 (m)
L_a, L_b	length of elliptical axis of x, y direction (m)
M_{cr}	dimensionless critical mass
N_g	the number of groove
p	pressure (N/m ²)



\bar{p} dimensionless pressure, $(\frac{p}{\mu\omega}(\frac{c}{r})^2)$

p_a ambient pressure (N/m²)

p_{cav} the pressure in cavitation (N/m²)

q'_i volume flow rate (m³/s)

r radius of journal bearing (m)

u velocity of step-slider bearing (m/s)

W load (N)

\bar{W} dimensionless load capacity, $(\frac{W}{\mu\omega r^2}(\frac{c}{r})^2)$

W_r radial load (N)

W_t tangential load (N)

x circumferential coordinate (m)

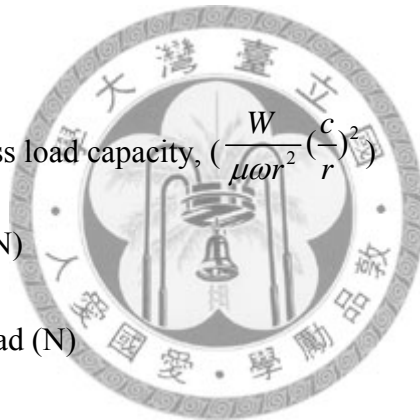
y coordinate in axial direction (m)

α groove angle (deg)

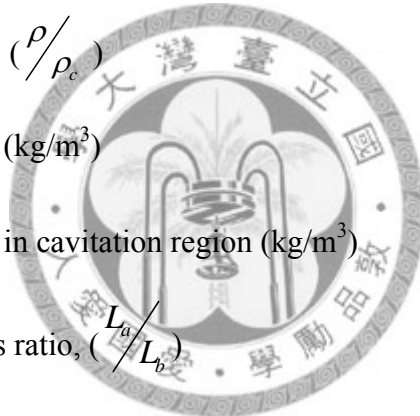
β bulk modulus (N/m²)

Γ groove depth ratio, (c_g / c)

δ groove width ratio, $(\frac{\delta_g}{\delta_g + \delta_r})$



δ_g	groove width (m)
δ_r	ridge width (m)
ε	eccentricity ratio
ϕ	circumferential coordinate (rad)
λ_k	diameter to length ratio, $(2r/L)$
μ	coefficient of viscosity ($N \cdot s/m^2$)
θ	density ratio, (ρ/ρ_c)
ρ	fluid density (kg/m^3)
ρ_c	fluid density in cavitation region (kg/m^3)
τ	elliptical axis ratio, (L_a/L_b)
τ_1, τ_2, τ_3	elliptical axis ratio of region 1, 2, 3
ω	angular velocity (rad/s)



1. Introduction

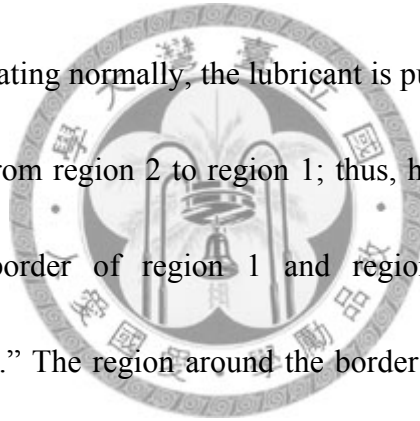
1-1 Current Applications of Grooved Journal Bearings

Hydrodynamic bearings are representative devices because of their low noise, low friction and high shock resistance, and they have several applications in data storage devices such as DVD and hard disk drive spindles [1, 2]. As data storage requirements of large capacities have increased markedly, improving the recording density in hard disk drive applications is essential. Conventional disk drive motors are supported by a bearing comprised of metal balls between a rotor and shaft. Thus, if any ball is defective, track misregistration occurs [3]. Hence, a spindle motor requires a non-contact bearing system to meet the demand of low non-repeatable runout of a spindle. Herringbone grooves on the journal bearing are used to increase spindle stiffness [4]. These grooves can distribute shock responses over an entire bearing, and thereby enhance mechanical damping of a bearing system. Herringbone-grooved journal bearings (HGJBs) also prevent contact between rotating and stationary parts. Moreover, adding herringbone grooves to the journal bearing allows lubricants to be pumped into the bearing, reducing

side leakage of the oil film [5]. Therefore, herringbone-grooved journal bearings (HGJBs) have been commonly employed in the computer information storage industry to provide for high rpm performance, such as that required for HD and DVD drives.

To widen the applications of HGJBs, Kawabata et al. [6] proposed a novel reversible rotation HGJB that can be rotated clockwise or counterclockwise. The helical grooves on the surface of journal are engraved with three regions, as shown in Fig.

1-1-1 When the shaft is rotating normally, the lubricant is pumped into the bearing from region 1 to region 2 and from region 2 to region 1; thus, high pressure is generated in the region around the border of region 1 and region 2, which is called the “pressure-generated region.” The region around the border of region 2 and region 3 is restored as the shaft rotates reversely for the purpose of pressure, and is called the “pressure-restored region.”



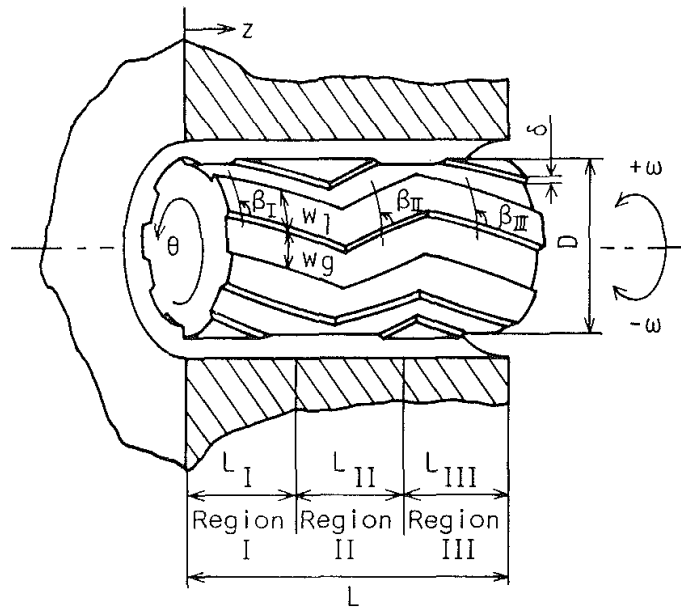


Fig. 1-1-1 The reversible rotation type herringbone grooved journal bearing proposed by Kawabata et al. [6]

In contrast, when the shaft is rotating reversely, the lubricant is pushed into the bearing from region 3 to region 2 and from region 2 to region 3. Thus, the reversible rotation HGJB is beneficial for load when the spindle motor rotates in the opposite direction, since it prevents the “no load capacity” condition when the shaft is rotated in the reverse direction. However, the load capacity of this bearing is only 70% of that of the conventional HGJB. In addition, few studies [7, 8] have investigated the characteristics of the reversible rotation HGJB. Therefore, the investigation of reversible rotation journal bearings with grooves is clearly warranted.

1-2 Research Needs for Groove Appearances

Although using HGJBs can improve stability characteristics, the smaller load capacity of HGJBs than that of plain journal bearings is a significant disadvantage. Therefore, some studies investigated ways to improve the herringbone groove profile. Kawabata *et al.* [6] proposed a novel reversible rotation HGJB that can be rotated clockwise or counterclockwise. However, the load capacity of this bearing is roughly 70% of that of the conventional HGJB. Junmei *et al.* [8], who studied the performance of asymmetrical HGJBs with a cavitation effect, concluded that a symmetrical groove pattern has the highest load capacity. Leuthold *et al.* [9] applied a sinusoidal groove pattern to a bearing. However, they did not assess the performance of this bearing. Liu *et al.* [10] presented the multi-step hydrodynamic grooved journal bearing. In contrast to conventional HGJBs, they developed an HGJB with a single set of helical grooves. The load capacity and stability of the multi-step HGJB are better than that of a HGJB.

On the other hand, some researchers improved the rectangular profile of herringbone grooves. Kang *et al.* [11] proposed a HGJB with circular-step grooves instead of rectangular grooves. They demonstrated that the circular-profile HGJB has

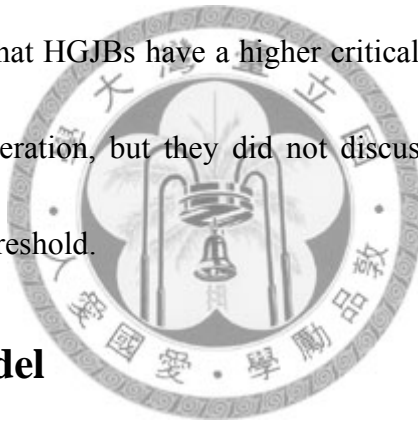
approximately 10% higher load capacity than a HGJB with a rectangular profile for eccentricity ratios up to 0.5. Gad *et al.*[12] found that for the circular groove profile in convergence over the step, the exit surface is approximately inclined, thereby reducing pumping capability. To overcome pressure losses of an abrupt step, they introduced a beveled-step groove profile for the HGJB, and increased load capacity and stability. Hence, to improve HGJB performance, one can investigate groove geometry.

Most studies mentioned employed straight-line grooves, which is similar to the herringbone groove. Few studies have examined a journal bearing with curved grooves. Additionally, no study has analyzed numerically or experimentally the improved effects of curved grooves. Therefore, investigations of journal bearing with curved grooves are warranted.

1-3 Stability Criteria

Many researchers have written programs to numerically analyze the stability of a journal bearing. Kirk and Gunter [13] determined the stability of the journal bearing system by the Routh-Hurwitz criterion, and examined the roots of the characteristic equation of the system. Similarly, if the journal bearing is perturbed at the equilibrium

position, then the threshold of operation for stability, the critical mass, can be obtained by solving the eigenvalue of equations of motion [14]. However, only a few studies have discussed critical mass and its relation to the stability of HGJBs. For instance, Bonneau and Absi [15] discussed the relationship between stiffness coefficients and the grooves, but they did not calculate the critical mass. Zirkelback and San Andrés [16] also made no mention of the relationship between groove angle and critical mass. Rao and Sawiski [17] showed that HGJBs have a higher critical speed than do plain journal bearings for concentric operation, but they did not discuss how the shape of groove might affect the stability threshold.



1-4 Cavitation Model

Lubricants are widely used in fluid film bearing to reduce friction and wear, provide load capacity. In the region of local converging film thickness, the hydrodynamic pressure rises to a peak and then decreases to ambient values at the side and trailing edges of the thin film; In zones where the film thickness locally increases, the fluid pressure may drop to ambient or below to its vapor pressure leading to the release of dissolved gases within the lubricant or lubricant vaporization.

As is known, cavitation phenomenon is important in liquid-lubricated journal bearings. The calculation of hydrodynamic force is dependent on the film model used, especially at high eccentricities. Some film models treat the cavitation in a simple way. For example, π -film theory (half-sommerfeld) and Swift-Stieber boundary condition.

Elrod and Adams introduced a computational scheme that mimics JFO theory[18], which is called “Elrod’s algorithm”. It avoids the complex program to trace the boundary between grid points. The algorithm incorporates a switch function and satisfy the mass continuity and the JFO theory. Relatively, JFO theory and Elrod’s algorithm are preferable methods to account for cavitation boundary conditions for hydrodynamic liquid-lubricated bearing. Lee *et. al* [19] and Jang and Chang[20] analyzed the HGJBs with cavitation based on these theories. This work employs the Elrod’s algorithm to account for the cavitation condition.

1-5 Analysis Methods

1-5-1 Discretization Method

When grooves on a journal bearing are curved or have a complex geometry, the Reynolds equation must be solved using numerical methods with geometric flexibility.

Generally, the finite element method (FEM) was adopted for spatial discretization. However, most interpolation functions used in an element are low-order polynomials. Thus, the solutions obtained by the FEM converge algebraically as the number of elements increases.

In 1984, Patera [21] proposed the spectral element method (SEM) by combining geometric flexibility of the FEM with the rapid convergence of the spectral method. The SEM is highly accurate and can discretize the domain into curvy geometries. The variables of computational domain are represented as high-order Lagrangian interpolants that improve the accuracy of solution in space with exponential convergence. For spatial discretization in curved geometries, Patera used an isoparametric mapping from the physical curvilinear quadrilaterals into the local standard elements [22]. Additionally, Schneidesch and Deville [23], who also solved the problem of curvy geometries, generated the curvilinear grid of quadrangle subdomains using Gordon transfinite interpolation[24].

Some studies have dealt with curved geometries using the SEM. Most studies are solved the circular geometry via flow problems between rotating cylinders [22, 25], of

cosine channel flow [23], and of two-dimensional compressible flow [26]. Additionally, the curved elements using the SEM are developed to solve three-dimensional flow problems [27, 28]. Therefore, spatial discretization using the SEM can be employed to analyze the improved effects of curved grooves on a journal bearing.

1-5-2 Treatment at the Discontinuity of Groove-Ridge Region

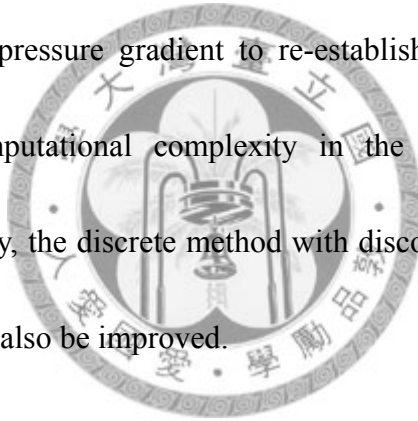
Many researchers have investigated the performance of HGJBs. In previous studies, the pressure distribution of the fluid film in the groove-ridge region was obtained by applying the narrow groove theory (NGT). NGT assumes that the number of grooves is infinite, such that the pressure distribution can be regarded as essentially linear along the grooves. Vohr and Chow [29] analyzed the herringbone-grooved gas-lubricated journal bearing using NGT, but manufacturing journals or sleeves with as many grooves as are required would be very expensive. Additionally, NGT overestimated the bearing load when the number of grooves was less than 16 [15], and when the number of grooves exceeds 16, the correct results can only be obtained at a low eccentricity. Hence, numerical methods that can be applied to bearings with a finite number of grooves must be developed.

In the 1990s, the number of investigations of bearings with finite numbers of HGJBs increased rapidly. Bonneau and Absi [15] presented a numerical study of gas herringbone grooved journal bearings that had a small number of herringbone grooves and analyzed the domain of validity of the NGT. Zirkelback and San Andrés [16] used finite element method to analyze HGJB pressure distribution and dynamic force coefficients. Faria [30] present a way to analyze HGJBs by combining the finite element method with high-order shape functions.

Only a few researchers have yet mentioned the issue of film thickness discontinuities in HGJBs with a finite number of grooves. Most of these studies have involved the application of a finite difference method (FDM) for discretization. For example, Kang *et al.* [11] used staggered nodes to avoid a violent change in film thickness, while Jang and Chang [20] investigated HGJBs by combining the finite volume method with Elrod's cavitation algorithm. The latter mentioned the incompatibility of Cartesian coordinates with grooves. Junmei *et al.* [8] assumed that the groove-ridge boundary was a slope because of the viscosity of the fluid film. However, this assumption was not accurate in practice, and the work also revealed the

shortcoming of the use of the FDM in processing the groove-ridge region.

The finite volume method has also been applied to solve the groove-ridge discontinuity problem. Arghir *et al.* [31] considered film discontinuities with a conserved flow rate, and applied the method to thrust bearing. Hernandez and Boudet [32] analyzed spiral groove gas seals, taking into consideration the continuity of normal mass flow at the groove boundaries of discontinuities. However, they used the equality relations of pressure and pressure gradient to re-establish the continuity of coupled nodes, which added computational complexity in the regions of film thickness discontinuities. Accordingly, the discrete method with discontinuity at the groove-ridge boundaries in HGJBs must also be improved.



1-6 Dissertation Outline

Firstly, the current work presents an approach for calculating the pressure distribution in, and dynamic coefficients of, HGJBs, that takes into consideration the fluid film discontinuity. Because of the abrupt change in the fluid film thickness in the groove-ridge region, conservation of mass was employed to solve this problem. To calculate the pressure distribution of the fluid film and carefully treat the cavitation

phenomenon, this work also combines the groove-ridge treatment in the Elrod's algorithm. The results are compared with experimental and computational results published in several studies. The comparison shows that the method can be employed to satisfactorily analyze HGJBs.

Secondly, this work proposes a novel elliptical-grooved journal bearing (EGJB) for data storage devices. A numerical program is used to analyze the appearance and characteristics of the EGJB. To calculate the pressure distribution of a fluid film, the Reynolds equation was solved using the SEM. Load capacity, the stability parameter, and side leakages of the EGJB are compared with those of the HGJB. The EGJB's configuration, which maximizes radial force, is investigated. Finally, the load distributions of several grooved journal bearings are compared to elucidate how elliptical grooves enhance load characteristics.

Finally, this work employs the elliptical groove on a reversible rotation journal bearing. The load distributions of the reverse rotation grooved journal bearings are compared to elucidate how elliptical grooves enhance load characteristics. Then, the Rev-EGJB's configuration, which maximizes radial force, is investigated.

2. Governing Equations

2-1 Reynolds Equation

Fig. 2-1-1 shows the coordinate system and geometry of a HGJB. The curvature of the film in the journal bearings is neglected. Since the film thickness is much less than the radius of the bearing, the fluid film can be unwrapped into a plane. The Reynolds equation for steady-state, laminar, isothermal, and incompressible flow is:

$$\frac{1}{r^2} \frac{\partial}{\partial \phi} \left[\frac{h^3}{12\mu} \frac{\partial p}{\partial \phi} \right] + \frac{\partial}{\partial y} \left[\frac{h^3}{12\mu} \frac{\partial p}{\partial y} \right] = \frac{\omega}{2} \frac{\partial h}{\partial \phi}, \quad (2-1)$$

where the coordinate system (ϕ, y) is fixed to the bearing.

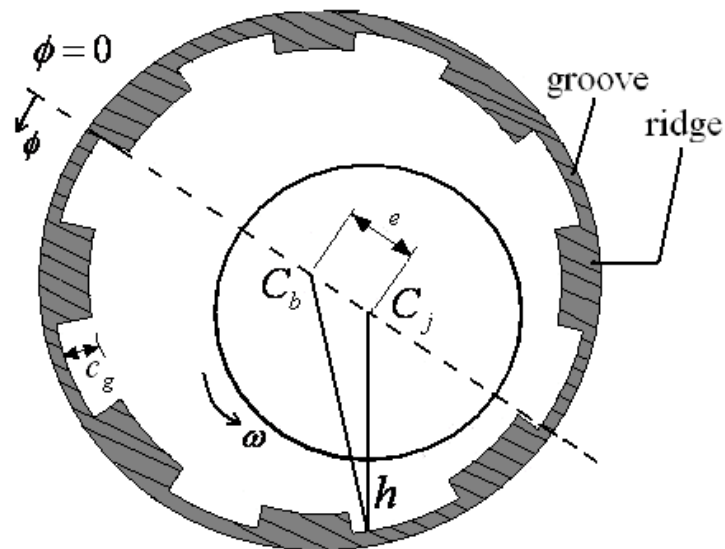


Fig. 2-1-1 Sketch of the fluid thickness for grooved bearing

Fluid thickness in the ridge or groove regions in terms of circumferential coordinate is shown in Fig. 2-1-2. The fluid thickness in the ridge and the groove regions in circumferential coordinates are:

$$h = c(1 + \varepsilon \cos \phi) \quad \text{in the ridge,} \quad (2-2a)$$

$$\text{and } h = c_g + c(1 + \varepsilon \cos \phi) \quad \text{in the groove.} \quad (2-2b)$$

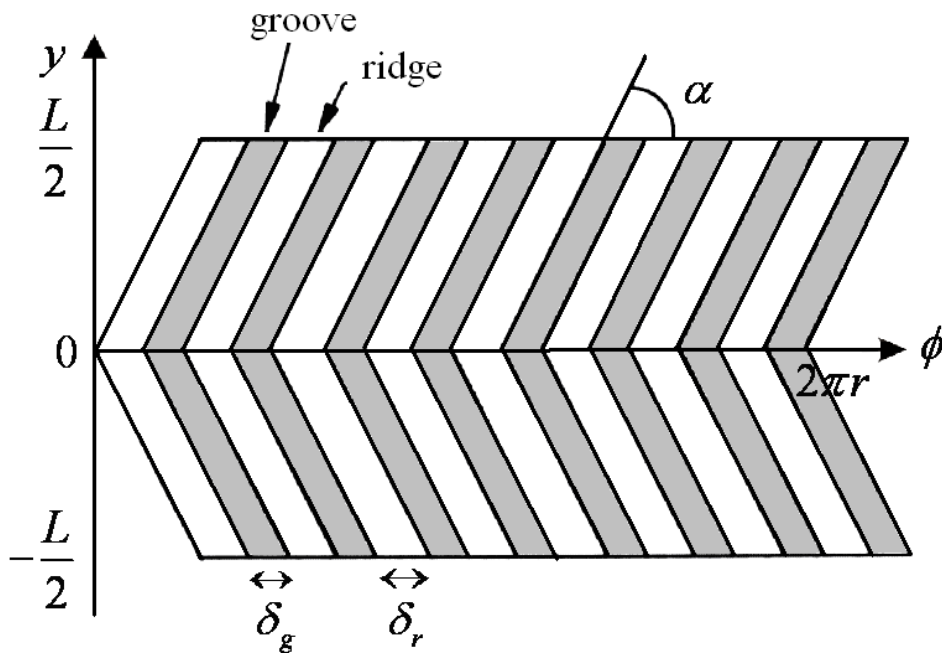


Fig. 2-1-2 Fluid thickness in the ridge or groove regions in terms of circumferential coordinate

However, for a smooth bearing, the film thickness changes as the grooved journal rotates. This problem can be solved by assuming that the groove journal is stationary

and the smooth bearing is rotating in the direction opposite to that of the groove journal

[16]. Thus, the Reynolds equation for a smooth bearing is

$$\frac{1}{r^2} \frac{\partial}{\partial \phi} \left[\frac{h^3}{12\mu} \frac{\partial p}{\partial \phi} \right] + \frac{\partial}{\partial y} \left[\frac{h^3}{12\mu} \frac{\partial p}{\partial y} \right] = -\frac{\omega}{2} \frac{\partial h}{\partial \phi}, \quad (2-3)$$

where the coordinate system (ϕ, y) is fixed to the journal.

The pressure field is continuous in the circumferential direction

$$p(\phi, y) = p(\phi + 2\pi, y), \quad (2-4)$$

and the cavitation algorithm is based on Reynolds condition

$$\bar{p}_{cav} = -1 \text{ or } 0 \quad \text{and} \quad \left. \frac{\partial p}{\partial \phi} \right|_{cav} = 0 \quad (2-5)$$

Oil film rupture may not occur in the fluid film of HGJBs when there is high pressure in the bearing and the lubricant supply is sufficient. In this case, the cavitation pressure is zero. However, as some part of the oil film is under negative pressure, the influence of negative pressure on the oil film rupture region cannot be disregarded.

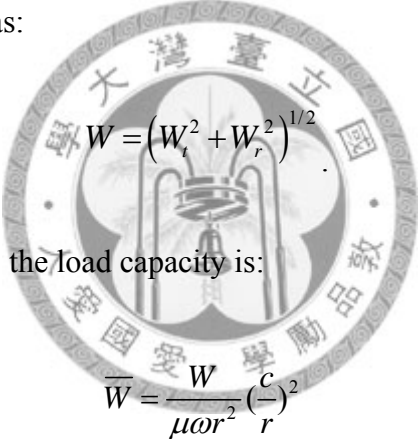
The pressure boundary conditions at bearing edges are $p\left(\phi, \frac{L}{2}\right) = p\left(\phi, -\frac{L}{2}\right) = 0$.

Once Eq. (2-1) has been solved for the pressure in the equilibrium state, the radial and tangential loads can be obtained by integrating the pressure over the bearing area, as follows:

$$W_t = \int_A pr \sin(\pi - \phi) dy d\phi \quad (2-6a)$$

$$W_r = \int_A pr \cos(\pi - \phi) dy d\phi \quad (2-6b)$$

The load can be expressed as:

$$W = (W_t^2 + W_r^2)^{1/2} \quad (2-7)$$


In dimensionless form, the load capacity is:

$$\bar{W} = \frac{W}{\mu \omega r^2} \left(\frac{c}{r}\right)^2 \quad (2-8)$$

Also the load distribution along the axial direction can be obtained by integrating the pressure force circumferentially

$$W' = \left[\left(\int_0^{2\pi} pr \sin(\pi - \phi) d\phi \right)^2 + \left(\int_0^{2\pi} pr \cos(\pi - \phi) d\phi \right)^2 \right]^{1/2} \quad (2-9)$$

and its dimensionless form, the distribution of dimensionless load capacity, is

$$\overline{W'} = \frac{W'}{\mu\omega r^2} \left(\frac{c}{r}\right)^2 \quad (2-10)$$

Side leakage, which is induced by the pressure gradient in the direction of bearing length, can be obtained by integrating the pressure gradient and film thickness over the circumferential direction. Side leakage from the front end and the rear end are given by

$$q_1 = -2r \int_0^{2\pi} \left(\frac{h^3}{12\mu} \frac{\partial p}{\partial y} \right)_{y=L/2} d\phi \quad (2-11a)$$

$$q_2 = -2r \int_0^{2\pi} \left(\frac{h^3}{12\mu} \frac{\partial p}{\partial y} \right)_{y=-L/2} d\phi \quad (2-11b)$$

The total side leakage is then given by

$$q = |q_1| + |q_2| \quad (2-12)$$

Notably, the magnitude of the front end and the rear side leakage are the same for symmetrically grooved patterns, but are different for asymmetrically grooved patterns.

In a dimensionless form, total side leakage is

$$\overline{q} = \frac{2\pi q}{rcL\omega} \quad (2-13)$$

2-2 Elrod's Cavitation Algorithm

Hirayama *et. al*[33] indicated that cavitation may largely influence pressure distribution. To carefully deal with the cavitation phenomenon, the Elrod's cavitation algorithm is applied in many studies and is found to preserve mass conservation throughout the entire fluid film. This section illustrates that the present treatment of groove-ridge discontinuity can also be included in the Reynolds equation with Elrod's algorithm[34].



The modified Reynolds Equation, introduced by Elrod, is written as:

$$\frac{\partial}{\partial x} \left(\frac{\rho_c h^3}{12\mu} g \beta \frac{\partial \theta}{\partial x} \right) + \frac{\partial}{\partial y} \left(\frac{\rho_c h^3}{12\mu} g \beta \frac{\partial \theta}{\partial y} \right) = \rho_c \frac{\partial(\theta h)}{\partial t} + \rho_c \frac{u}{2} \frac{\partial(\theta h)}{\partial x} \quad (2-14)$$

where θ is the density ratio of fluid density ρ divided by fluid density in the cavitation region ρ_c , β is the bulk modulus, and g is a switch function in the flow field with

$$g = \begin{cases} 1 & \text{for full-film region} \\ 0 & \text{for cavitation region} \end{cases} \quad (2-15)$$

In Elrod's algorithm, JFO theory was incorporated into a single Reynolds equation valid on both the full film and cavitation zones. A switch function g allows satisfaction of the boundary conditions at the cavitation interface in the full film and cavitation regions.

The pressure can be obtained from fluid density:

$$P = P_{cav} + g\beta \ln(\theta) \quad (2-16)$$

Thus, the load capacity can be obtained from the Eq.(2-6) to Eq.(2-8).

2-3 Stability Parameter

This study discusses stability using the dimensionless radial stiffness, which was employed by Vohr and Chow [29], and Gad *et al.* [12]. The definition of dimensionless radial stiffness is

$$\bar{F}_R = \frac{2\pi\bar{W} \cos \phi}{\varepsilon} \quad (2-17)$$

The large radial force parameter is able to restrain the centrifugal force, which is produced from whirling phenomena [29].

2-4 Groove Profile

Fig. 2-4-1 shows the shape of the elliptical grooves. Because variation in elliptical shape affects the pressure distribution of a fluid film, this work varies the elliptical axis ratio to determine how the shapes of elliptical grooves affect EGJB performance. The equation of elliptical grooves is

$$\frac{(x-x_0)^2}{L_a^2} + \frac{(y-y_0)^2}{L_b^2} = 1 \quad (2-18)$$

where the center of the ellipse is at (x_0, y_0) , and L_a and L_b are the axis length in the x-direction and y-direction, respectively. The elliptical axis ratio τ is $\frac{L_a}{L_b}$.

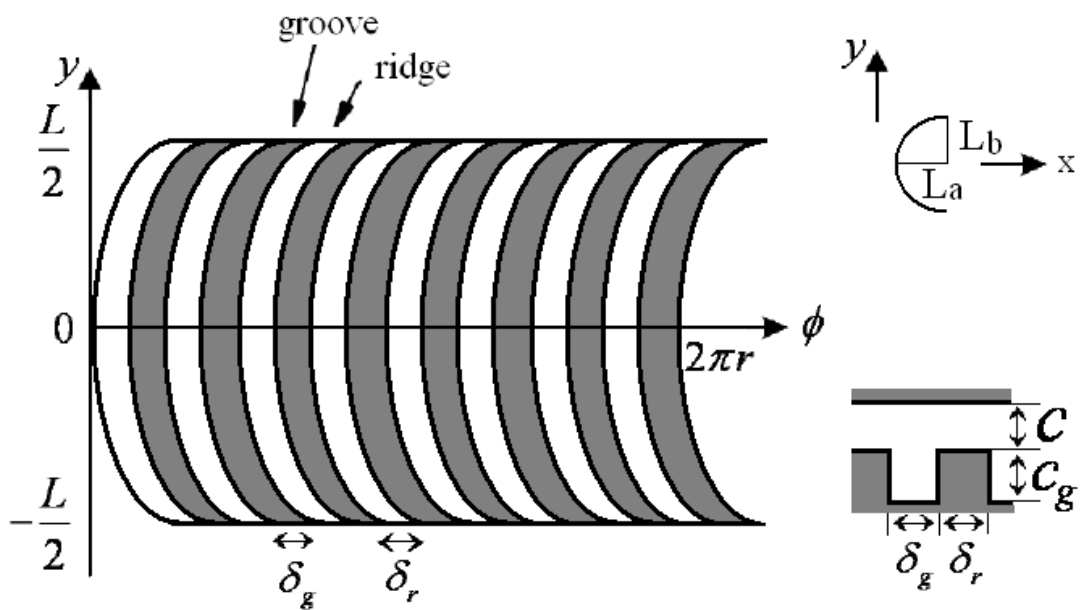


Fig. 2-4-1 Parameters of the EGJB (The grooves can be engraved on either journal or bearing surface.)

The appearance of the elliptical groove is equivalent to a herringbone groove with a groove angle of 90° at the bearing center and groove angle of 0° at both ends, meaning that the groove angle decreases gradually from the center in the direction of bearing length. Instead of a straight-line groove, the elliptical groove is adopted to improve the performance of grooved journal bearings.



3. Numerical Method

This chapter introduces the numerical method used in the program, which solves the Reynolds Equation. The spatial discretization of fluid film is shown in Section 3-1. The analysis at the groove-ridge discontinuity of 1-D and 2-D bearing is written in Section 3-2. Finally, the grid independence test is validated in Section 3-3.

3-1 Spatial Discretization- Spectral Element Method (SEM)

The SEM, a high accuracy and efficiency method, is used to discretize the Reynolds equations for HGJB. The Reynolds equations can be written as


$$\nabla \cdot (h^3 \nabla p) - 6\mu_0 u_j \frac{\partial h}{\partial x} = 0 \quad \text{in } \Omega; \quad \nabla = \frac{\partial}{\partial x} \vec{e}_x + \frac{\partial}{\partial y} \vec{e}_y, \quad (3-1)$$

where Ω is the computational domain.

Assume that $v = \delta p$ is the test function of p , and multiply Eq. (3-1) by v with weighted residual method, the first term of Eq. (3-1) yields:

$$\int_{\Omega} \nabla \cdot (h^3 \nabla p) v d\Omega = \int_S v (h^3 \nabla p) \cdot d\vec{S} - \int_{\Omega} (h^3 \nabla p) \cdot (\nabla v) d\Omega \quad (3-2)$$

where S is the boundary of computational domain. Substitute Eq. (3-2) into Eq. (3-1),

the weighted-integral form can be derived as :

$$\int_{\Omega} (h^3 \nabla p) \cdot (\nabla v) d\Omega = \int_s v (h^3 \nabla p) \cdot d\bar{S} - \int_{\Omega} \left(6\mu_0 U \frac{\partial h}{\partial x} \right) v d\Omega \quad (3-3)$$

the first term of RHS is the flow rate on the boundary.

For solving flow field in complex geometries, SEM is provided to divide the flow elements Ω into k spectral elements,

$$\Omega = \bigcup_{k=1}^K \Omega_k \quad (3-4)$$

Fig. 3-1-1 shows the transformation from the local coordinate $\Omega_i(x,y)$ to the physical coordinate system $\hat{\Omega}(r,s)$ of a square region. The mapping function of each of the spectral elements is

$$(x, y) \in \Omega_i \Rightarrow \hat{\Omega}(r, s) \in \Lambda \times \Lambda, \Lambda = [-1, 1] \quad (3-5)$$

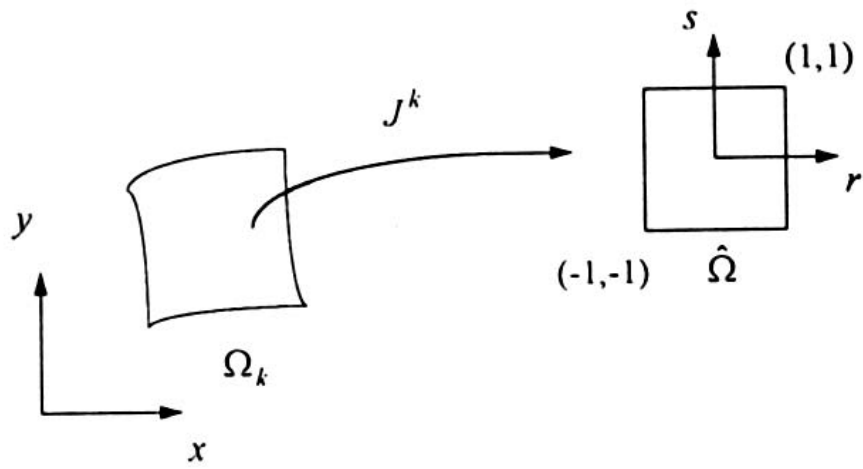


Fig. 3-1-1 the transformation from the local coordinate to the physical coordinate system



and its Jacobian of transformation can be written as :

$$J \equiv \begin{vmatrix} \frac{\partial x}{\partial r} & \frac{\partial y}{\partial r} \\ \frac{\partial x}{\partial s} & \frac{\partial y}{\partial s} \end{vmatrix}$$

Thus we can derive

$$\frac{\partial r}{\partial x} = \frac{1}{J} \frac{\partial y}{\partial s}, \quad \frac{\partial s}{\partial x} = -\frac{1}{J} \frac{\partial y}{\partial r}, \quad \frac{\partial r}{\partial y} = -\frac{1}{J} \frac{\partial x}{\partial s}, \quad \frac{\partial s}{\partial y} = \frac{1}{J} \frac{\partial x}{\partial r} \quad (3-6)$$

Rewrite the Eq. (3-3) in terms of local coordinates :

$$\sum_{k=1}^K \int_{\hat{\Omega}} \frac{1}{J^k} (\hat{\nabla} v^k) \cdot (h^3 \hat{\nabla} p^k) dr ds = - \sum_{k=1}^K \int_{\hat{\Omega}} v^k f^k J^k dr ds \quad (3-7)$$

where

$$f = \left(6\mu_0 U \frac{\partial h}{\partial x} \right)$$

$$\text{and } \hat{\nabla} = \left(\frac{\partial y}{\partial s} \frac{\partial}{\partial r} - \frac{\partial y}{\partial r} \frac{\partial}{\partial s} \right) \bar{e}_x + \left(\frac{\partial x}{\partial r} \frac{\partial}{\partial s} - \frac{\partial x}{\partial s} \frac{\partial}{\partial r} \right) \bar{e}_y \quad (3-8)$$

The pressure P is approximated by

$$p(x, y)|_{\Omega^k} = \sum_{m=0}^N \sum_{n=0}^N p_{mn}^k h_m(r) h_n(s) \quad (3-9)$$

where p_{mn}^k is an approximate pressure of nodal point (m,n) in the k-th element, and

$h_i(\zeta)$ is orthogonal Lagrangian interpolants of degrees n. It satisfies the property

$$h_i(\zeta_j) = \delta_{ij} \quad (3-10)$$

$$\frac{dh_j}{dr}(\zeta_i) = D_{ij} \quad (3-11)$$

h_i is unity at a single point, and are zero at all other Gauss–Lobatto Legendre points.

The points ζ_i are the collocation points, and its quadrature weights is defined by

the relationship

$$\xi_0 = -1, \xi_N = 1, \xi_j (j = 1, \dots, N-1) \text{ zeroes of } L'_N \quad (3-12)$$

$$\rho_p = \frac{2}{N(N+1)} \frac{1}{[L'_N(\xi_p)]^2} \quad j = 0, \dots, N \quad (3-13)$$

Similarly, the test function v can be shown by Lagrangian interpolation function

$$v(x, y)|_{\Omega^k} = h_i(r)h_j(s) \quad (3-14)$$

Substitute u and v into Eq. (3-7), and obtain

$$\widehat{\nabla} p^k(\xi_i, \xi_j) = \widehat{\nabla}_{ijmn}^k p_{mn}^k \quad \widehat{\nabla} v^k(\xi_i, \xi_j) = \widehat{\nabla}_{ijpq}^k v_{pq}^k \quad (3-15)$$

with

$$\widehat{\nabla}_{ijmn}^k = [(\partial y / \partial s)_{ij}^k D_{im} \delta_{jn} - (\partial y / \partial r)_{ij}^k D_{im} \delta_{jn}] \bar{e}_x + [(\partial x / \partial r)_{ij}^k D_{im} \delta_{jn} - (\partial x / \partial s)_{ij}^k D_{im} \delta_{jn}] \bar{e}_y$$

Then Eq. (3-7) can be derived in the form of tensor product :

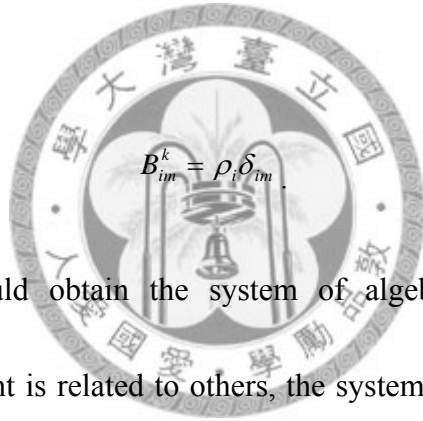
$$\sum_{k=1}^K \sum_{m=0}^N \sum_{n=0}^N (A_{ijmn}^{x,k} + A_{ijmn}^{y,k}) (h_{ijmn}^k)^3 p_{mn}^k = \sum_{k=1}^K \sum_{m=0}^N \sum_{n=0}^N J_{ij}^k B_{im}^k B_{jn}^k f_{mn}^k \quad (3-16)$$

with

$$A_{ijmn}^{x,k} = \rho_p \rho_q \frac{1}{J_{pq}^k} [(y_s)_{pq}^2 D_{pi} D_{pm} \delta_{nq} + (y_r)_{pq}^2 D_{qj} D_{qn} \delta_{mp} + (y_s y_r)_{pq}^2 D_{pi} D_{qn} \delta_{mp} + (y_s y_r)_{pq}^2 D_{qj} D_{pm} \delta_{nq}] \quad (3-17)$$

$$A_{ijmn}^{y,k} = \rho_p \rho_q \frac{1}{J_{pq}^k} [(x_s)_{pq}^2 D_{pi} D_{pm} \delta_{nq} + (x_r)_{pq}^2 D_{qj} D_{qn} \delta_{mp} + (x_s x_r)_{pq}^2 D_{pi} D_{qn} \delta_{mp} + (x_s x_r)_{pq}^2 D_{qj} D_{pm} \delta_{nq}] \quad (3-18)$$

and



$B_{im}^k = \rho_i \delta_{im}$ (3-19)

In this way, we could obtain the system of algebraic equations. Since the collocation point in element is related to others, the system matrix is dense. This work employs the conjugate gradient method (CGM) to solve this system. Fig. 3-1-2 shows the flowchart used in this work.

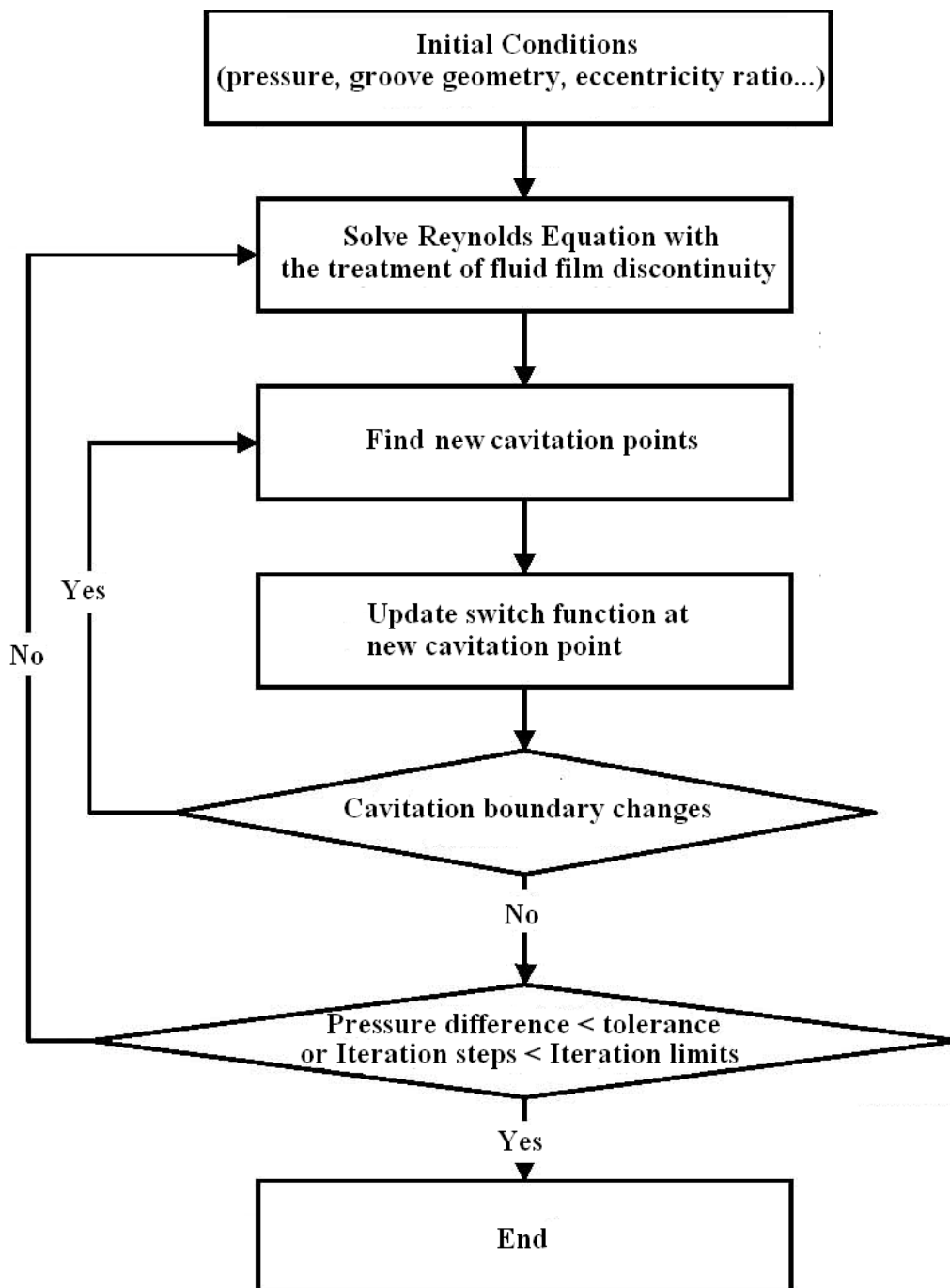


Fig. 3-1-2 The flowchart of the numerical program (solver)

3-2 Treatment in Groove-Ridge Discontinuity

3-2-1 For 1-D Step-Slider Bearing

Firstly, a one-dimensional step-slider bearing, shown in Fig. 3-2-1, is analyzed in detail. The analysis demonstrates the way to deal with the abrupt change in the thickness of the fluid film in the groove-ridge region of a grooved journal bearing. The length of the step-slider is L . The discontinuity is assumed to be in the middle of the step-slider. The film thickness is $h_0 + s_h$ in the groove region, and h_0 in the ridge region.



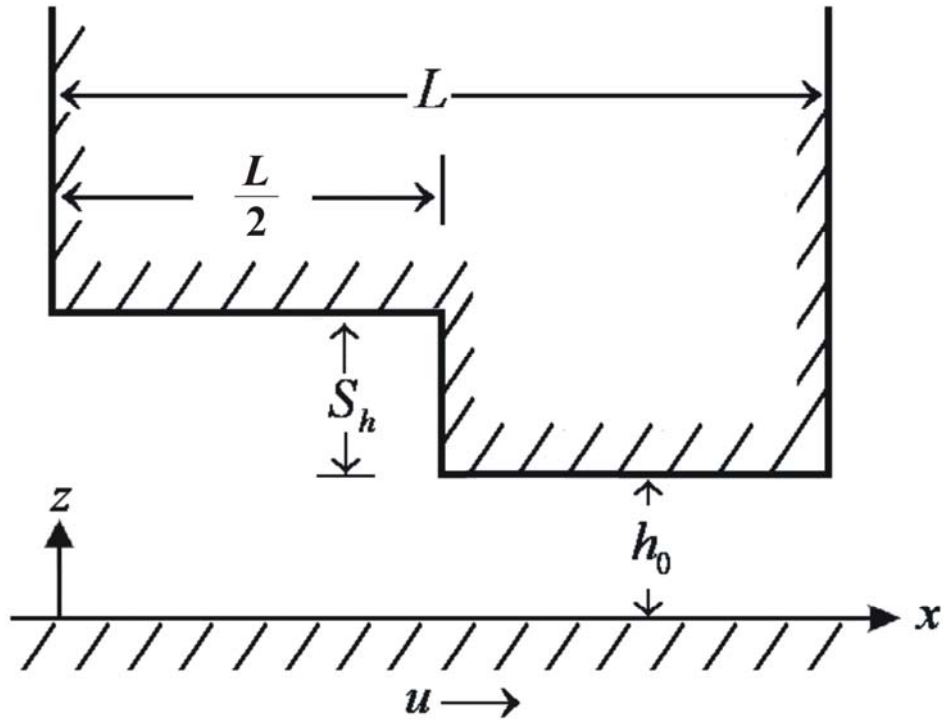


Fig. 3-2-1 Geometry of a parallel slider bearing

The governing equation is solved using the SEM, in which the approximate solution within a typical element is of the form:

$$p^e = \sum_{j=1}^n p_j^e \varphi_j(x) \quad (3-20)$$

where p_j^e is the value of p^e at the j -th node of the element, and $\varphi_j(x)$ is the Lagrange interpolation function.

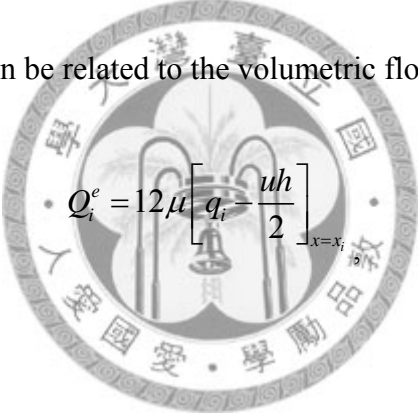
The first step is to derive the nodal equation. Based on the Galerkin formulation, the weighting function is equal to the expansion base of the pressure. The weighted integrated form of the element with boundaries x_A and x_B is:

$$\sum_{j=1}^n k_{ij}^e p_j^e = Q_i^e \quad (3-21)$$

where

$$k_{ij} = \int_{x_A}^{x_B} -\frac{d\phi_i}{dx} \left(h^3 \frac{d\phi_j}{dx} \right) dx \quad (3-22)$$

The boundary term can be related to the volumetric flow rate by [35]



$$Q_i^e = 12\mu \left[q_i - \frac{uh}{2} \right]_{x=x_i} \quad (3-23)$$

where

$$q_i = \left[-\frac{h^3}{12\mu} \frac{dp}{dx} + \frac{uh}{2} \right]_{x=x_i} \quad (3-24)$$

is the volumetric flow rate obtained from the continuity equation. Thus, the boundary term of each node i can be written as:

$$Q_i^e = \begin{cases} - \left[h^3 \frac{dp}{dx} \right]_{x=x_1}^e, & i = 1 \\ \left[h^3 \frac{dp}{dx} \right]_{x=x_n}^e, & i = n \\ 0, & \text{others} \end{cases} \quad (3-25)$$

The next step is to assemble the elemental equations into a global equation. The balance of the boundary terms at the connecting nodes can be simplified by imposing the balance of flow rate across the interface of the element:

$$\begin{aligned} Q^{e,e+1} &= Q_n^e + Q_1^{e+1} \\ &= 6\mu u \left[h \Big|_{x=x_1}^{e+1} - h \Big|_{x=x_n}^e \right] \\ &= \begin{cases} 0 & \text{for the node without a step height} \\ 6\mu s_h u & \text{for the node with a step height } s_h \end{cases} \end{aligned} \quad (3-26)$$

3-2-2 For 2-D HGJB with Reynolds Equation

The two-dimensional governing equation for HGJB is solved by the SEM, following the procedure used for the one-dimensional instance above. Discontinuity in the groove-ridge region of a two-dimensional HGJB is modeled with two adjacent elements, as shown in Fig. 3-2-2. The volume flow rate at point p, located at the interface between element 1 and element 2, can be expressed as:

$$q_{1x} = -\frac{h^3}{12\mu} \frac{\partial p}{\partial x} \Big|_{e=1} + \frac{uh}{2}, \quad q_{1y} = -\frac{h^3}{12\mu} \frac{\partial p}{\partial y} \Big|_{e=1} \quad (3-27)$$

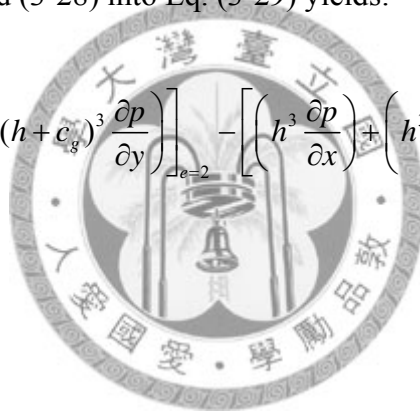
$$q_{2x} = -\frac{(h+c_g)^3}{12\mu} \frac{\partial p}{\partial x} \Big|_{e=2} + \frac{u(h+c_g)}{2}, \quad q_{2y} = -\frac{(h+c_g)^3}{12\mu} \frac{\partial p}{\partial y} \Big|_{e=2} \quad (3-28)$$

Conservation of volume flow rate at point p yields:

$$q_{1x} + q_{1y} = q_{2x} + q_{2y} \quad (3-29)$$

Substituting Eqs. (3-27) and (3-28) into Eq. (3-29) yields:

$$\left[\left((h+c_g)^3 \frac{\partial p}{\partial x} \right) + \left((h+c_g)^3 \frac{\partial p}{\partial y} \right) \right]_{e=2} - \left[\left(h^3 \frac{\partial p}{\partial x} \right) + \left(h^3 \frac{\partial p}{\partial y} \right) \right]_{e=1} = 6\mu c_g u \quad (3-30)$$



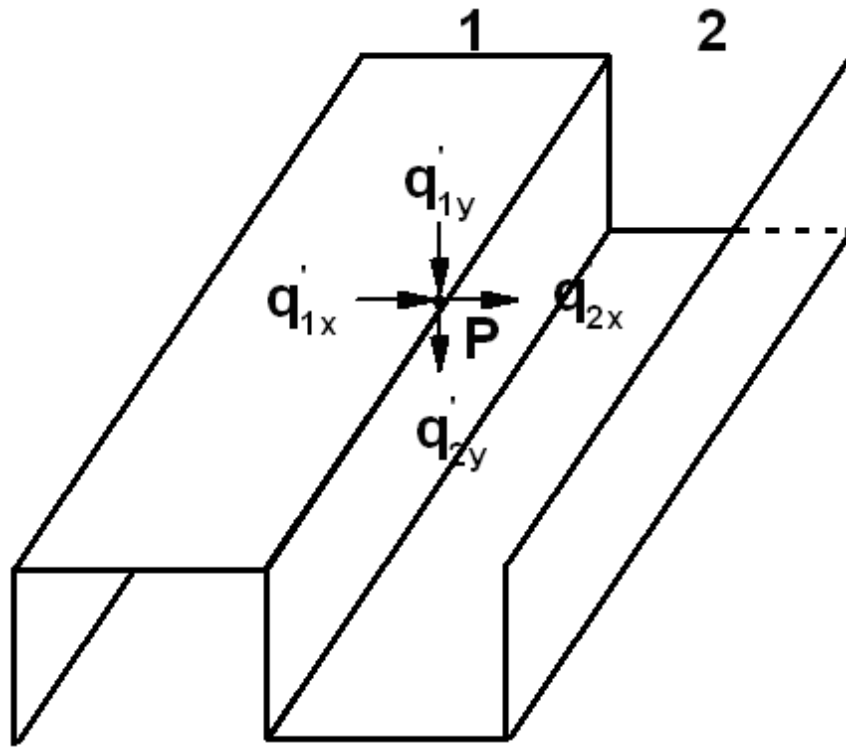


Fig. 3-2-2 Conservation of flow rate at a groove-ridge region

Therefore, the difference between the boundary terms of two neighboring elements at the groove-ridge region is given by:

$$Q^{e,e+1} = \int 6\mu c_g \bar{u} \cdot d\bar{L}_e, \quad (3-31)$$

where the length of two adjacent elements is L_e .

The boundary terms at the interface nodes, depicted by Eq. (3-26) or Eq. (3-31),

can also be applied to the finite element method, which is a special case of the SEM. From the code development point of view, it is evident that a code written for the plain journal bearing and for either the finite element or the SEM can be readily revised to adapt to grooved journal bearings. The present method can also be adopted for grooves with curvy geometry. The author have previously analyze the characteristics of an elliptic groove based on the present method [36].

3-2-3 For 2-D HGJB with Elrod's Algorithm

The method of conservation of volume flow rate at point p with two adjacent elements is already shown in section 3-2-1 and 3-2-2. with the Reynolds equation. Similarly, based on the modified Reynolds equation, conservation of volume flow rate with two adjacent elements can be derived. The volume flow rate at point p, located at the interface between element 1 and element 2, are :

$$q'_{1x} = -\frac{h^3}{12\mu} g\beta \frac{\partial\theta}{\partial x}\Big|_{e=1} + \theta \frac{uh}{2}, \quad q'_{1y} = -\frac{h^3}{12\mu} g\beta \frac{\partial\theta}{\partial y}\Big|_{e=1} \quad (3-32)$$

$$q'_{2x} = -\frac{(h+c_g)^3}{12\mu} g\beta \frac{\partial\theta}{\partial x}\Big|_{e=2} + \theta \frac{u(h+c_g)}{2}, \quad q'_{2y} = -\frac{(h+c_g)^3}{12\mu} g\beta \frac{\partial\theta}{\partial y}\Big|_{e=2} \quad (3-33)$$

By the conservation of volume flow rate at point p from Eq. (3-29), the difference

between the boundary terms of two neighboring elements at the groove-ridge region is obtained, considering the Elrod's algorithm, as follows:

$$\left[\left\{ \left((h+c_g)^3 \frac{\partial \theta}{\partial x} \right) + \left((h+c_g)^3 \frac{\partial \theta}{\partial y} \right) \right\} g \beta \right]_{e=2} - \left[\left\{ \left(h^3 \frac{\partial \theta}{\partial x} \right) + \left(h^3 \frac{\partial \theta}{\partial y} \right) \right\} g \beta \right]_{e=1} = 6\theta\mu c_g u \quad (3-34)$$

Therefore, the difference between the boundary terms of two neighboring elements at the groove-ridge region is given by:

$$Q^{e,e+1} = \int 6\theta\mu c_g \vec{u} \cdot d\vec{L}_e \quad (3-35)$$


3-3 Grid Independent Test

3-3-1 HGJB

In this work, the element we used in the first groove was taken apart in the circumferential direction and treated as a periodic boundary. Therefore, the simulation was performed with nine grooves and eight ridges, with a total of 17 elements in the circumferential direction and eight elements in the axial direction. Table 3-3-1 presents the geometrical parameters of the HGJBs. Fig. 3-3-1 displays the mesh system that was used in the program.

Table 3-3-1 Design parameters of the HGJB

Clearance, c	6×10^{-6} (m)
Radius, r	0.002 (m)
Length, L	0.004 (m)
Fluid viscosity, μ	0.00124 (Pa·s)
Number of grooves	8
Groove depth ratio, Γ	1.0
Groove width ratio, δ	0.5
Journal speed, ω	5000 (rpm)
Groove location	on bearing

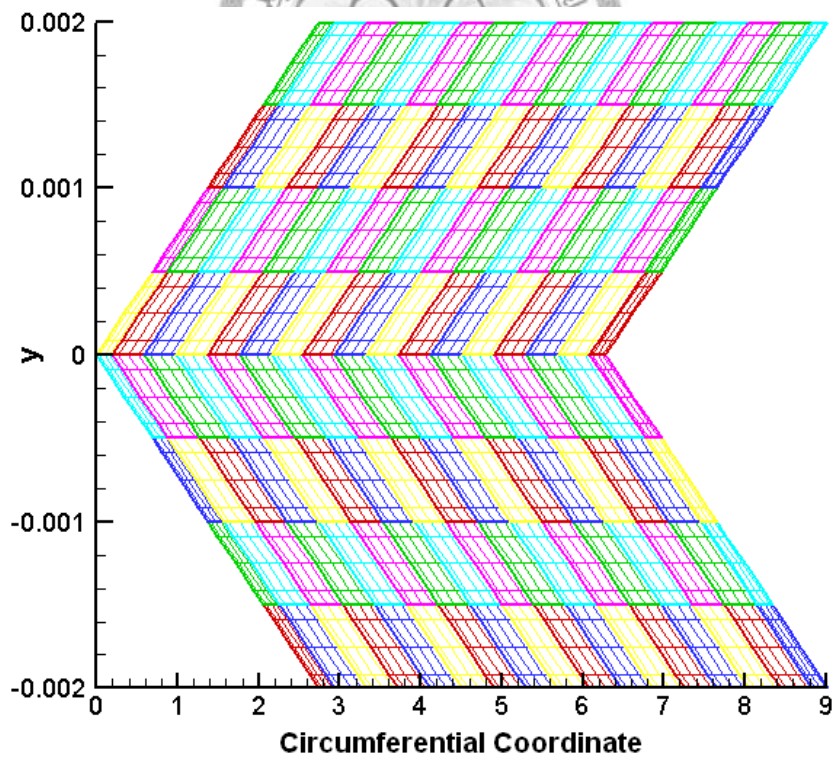


Fig. 3-3-1 Mesh system used in the program

Before the HGJBs were analyzed, a sufficient number of grids in the computational domain had to be established. The following operating conditions were used: groove angle = 20 degrees, groove depth ratio = 1.0, groove width ratio = 0.5, eccentricity ratio = 0.7, and diameter to length ratio = 1.

Table 3-3-2 presents the critical masses (appendix A) evaluated using various nodes. As the number of nodes increases, the critical masses asymptotically approach a constant. The deviation of critical mass of seven nodes per element from that of nine nodes is very small, and so seven nodes were adopted to analyze the HGJBs.

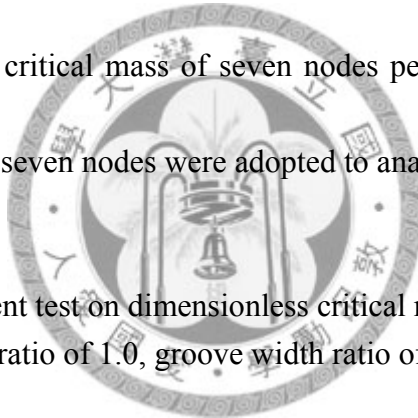


Table 3-3-2 Grid independent test on dimensionless critical mass (appendix A) at groove angle of 20°, groove depth ratio of 1.0, groove width ratio of 0.5, and at eccentricity ratio of 0.7

Number of Nodes	Dimensionless Critical Mass	Deviation
3	18.83	-2.03%
4	18.85	-1.93%
5	18.99	-1.20%
6	19.09	-0.68%
7	19.19	-0.16%
8	19.22	0.00%
9	19.22	

3-3-2 EGJB

This work used curvilinear elements to discretize the elliptical grooves, and mapped the physical curvilinear quadrilaterals into local standard elements isoparametrically [22] in this numerical program. The elements used in the first groove were taken apart in the circumferential direction, and treated as a periodic boundary. Therefore, a simulation was performed with a total of 17 elements in the circumferential direction and 8 elements in the axial direction. Fig. 3-3-2 shows the mesh system used in the program for EGJB.



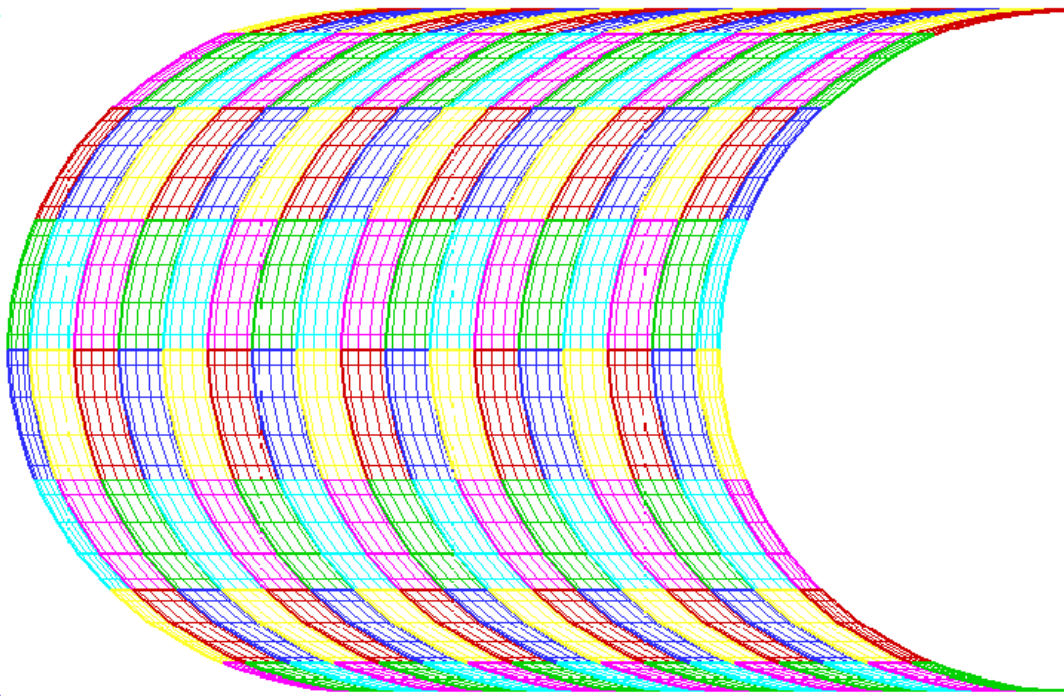


Fig. 3-3-2 Mesh system used in the program of EGJB

Before the EGJBs are examined, whether the number of nodes in the computational domain is sufficient must be determined. Operating conditions are elliptical axis ratio of 1.5, groove depth ratio of 1.0, groove width ratio of 0.5, and eccentricity ratio of 0.7.

Fig. 3-3-3 and Fig. 3-3-4 present load capacity and side leakage of EGJB evaluated using various nodes. As the number of nodes per dimension for an element increases, load capacities asymptotically approach a constant. The difference in load capacity with

8 nodes and 10 nodes is very small; thus, 8 nodes were used to analyze the EGJB.

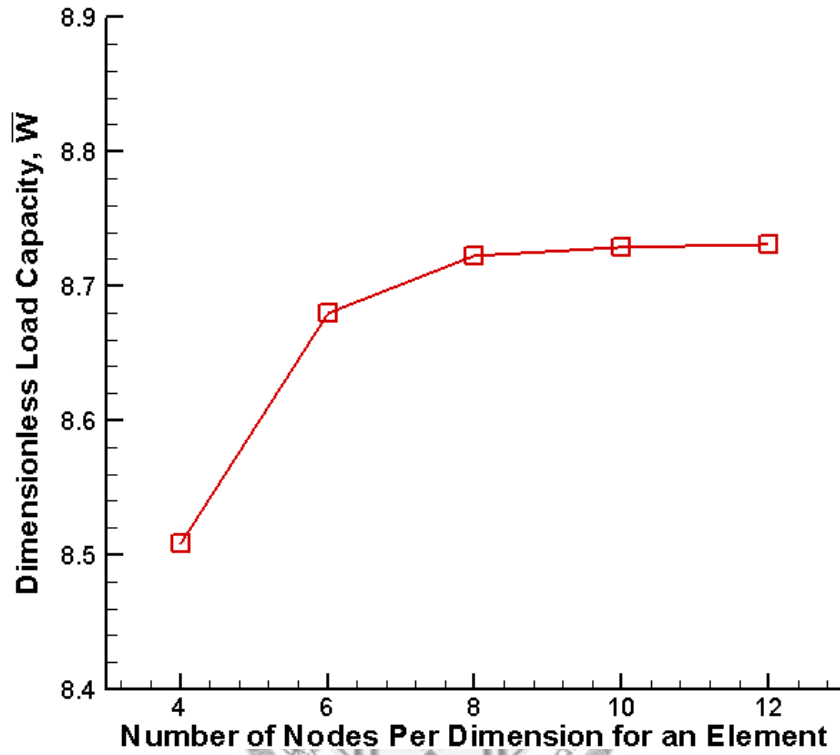


Fig. 3-3-3 Grid independent test to evaluate the load capacity of EGJB

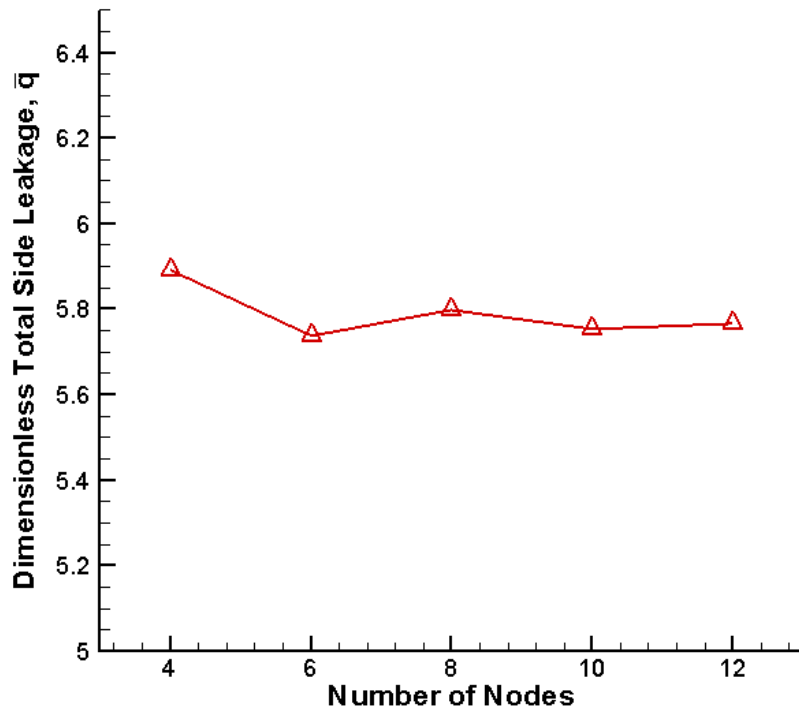


Fig. 3-3-4 Grid independent test to evaluate the leakage of EGJB



4. Validation

This work firstly verifies the numerical programs for a 1-D slider bearing and for the HGJB in section 4-1 when there is a simple cavitation account in the fluid film. Secondly, the numerical program of the HGJB with Elrod's algorithm is validated in section 4-2. Ultimately, the numerical program of the EGJB is validated.

4-1 Load Capacity

4-1-1 One-dimensional Step-Slider Bearing

The numerical results were compared with the analytical solution for a step with an infinitely wide Rayleigh step bearing. The governing equation for a one-dimensional slider bearing is written as:

$$\frac{d}{dx} \left[\frac{h^3}{12\mu} \frac{dp}{dx} \right] = \frac{u}{2} \frac{dh}{dx} \quad (4-1)$$

The equation above can be solved by the SEM mentioned in the previous section. The parameters used were: $s_h = 1.0 \times 10^{-2} m$, $h_o = 5.0 \times 10^{-3} m$, $L = 1.0 m$, $u = 20 m/s$, and the number of grid cells used was 17. Notably, two elements, the groove element and the ridge element, are used to balance the boundary terms.

To compare the pressure distribution calculated, the central difference method was also employed here to discretize the slider bearing. To demonstrate the effect of the treatment at the discontinuity on the accuracy of pressure, there are two ways to deal with the discontinuity. One is to obtain the derivative of the film thickness with respect to length in the region of the discontinuity by treating the groove-ridge boundary as a slope, as was done by Junmei *et al.* [8]. The other is to apply the conservation of mass at the discontinuity.

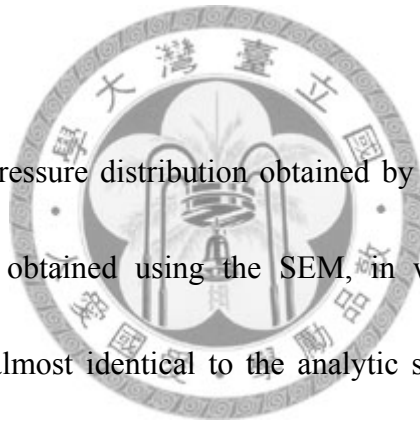


Fig. 4-1-1 plots the pressure distribution obtained by the SEM and by the FDM. The pressure distribution obtained using the SEM, in which the treatment at the discontinuity is taken, is almost identical to the analytic solution [35]. It can also be seen that the pressure distribution is 12% less accurate when using the FDM without the treatment that considers the conservation of mass at the discontinuity. However, when using the FDM with the treatment at the discontinuity, the pressure distribution is as accurate as that obtained using SEM.

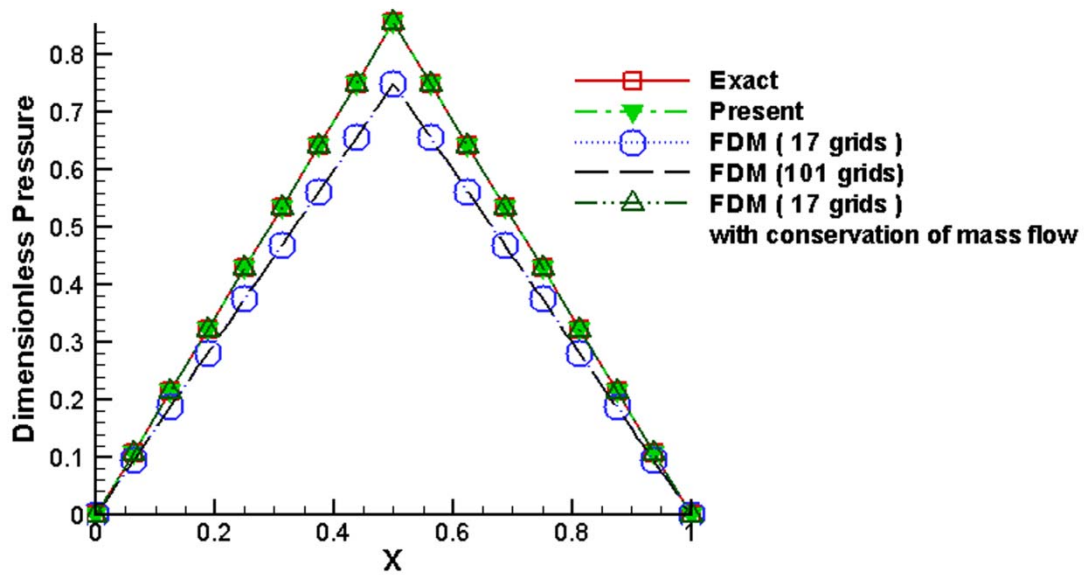


Fig. 4-1-1 The numerical result of pressure distribution in one-dimensional slider bearing

4-1-2 Load Comparison of HGJB

The numerically determined load of HGJB with the Reynolds equation can be verified as follows. For this case, this work simply adopts the Reynolds condition at the edge of the cavitation region. Fig. 4-1-2 shows a comparison of bearing load capacities with the experimental data presented by Hirs [37]. The present method, in which the groove-ridge discontinuity treatment is considered, is accurate in solving the load of the HGJBs except for the case of the load capacity at above the eccentricity ratio 0.6. The discrepancies may result from the occurrence of cavitation, which will be discussed in the next section.

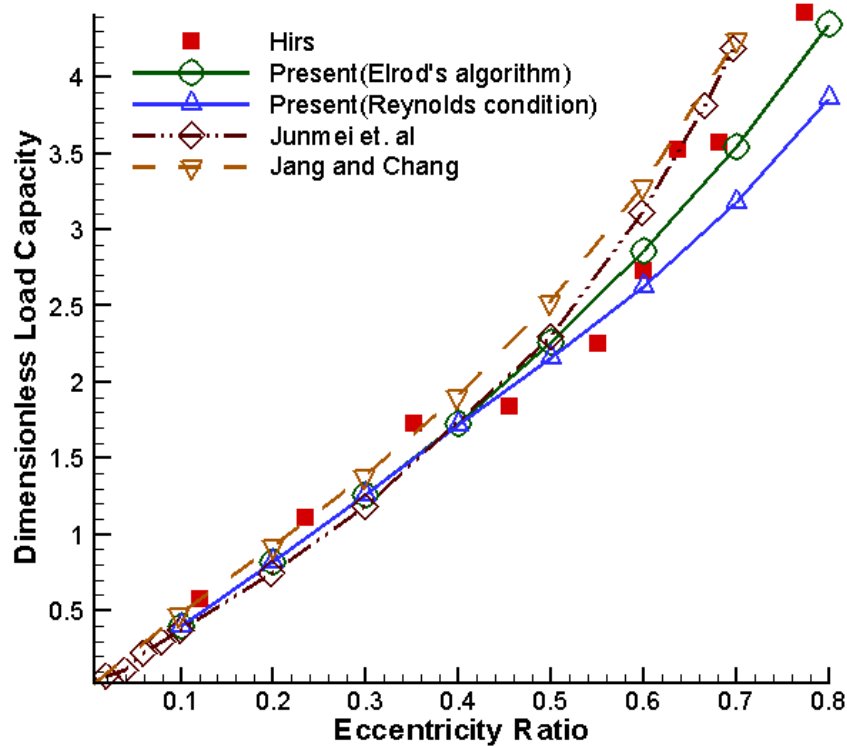


Fig. 4-1-2 Comparison of load with studies [8, 20, 37]

Therefore, by validating the one-dimensional slider bearing and the HGJB, it can be concluded that the present method – the SEM incorporating the treatment at the discontinuity by considering conservation of mass – can be applied to correctly determine the pressure distribution of the fluid film.

On the other hand, the numerical program was verified experimentally using a prototype spindle motor built in the laboratory. The study [10] designed the geometry of

a novel multi-step HGJB using our numerical program for HGJB, then the study showed that the multi-step HGJB has the required load capacity.

4-1-3 Load Comparison of HGJB with Elrod's Model

The numerical program for a plain journal bearing is first discussed to verify the accuracy of pressure distribution considering a cavitation analysis. The HGJB with cavitation appearance is then tested to verify the accuracy of numerically determined loads when the conservation of mass flow rate in a discontinuous fluid film is applied with Elrod's algorithm.

4-1.3.1 Load of a plain journal bearing with cavitation

Fig. 4-1-3 shows the comparison of the pressure distributions for a plain journal bearing using the present method incorporating the Elrod's algorithm and the experimental data presented by Jakobsson and Floberg [18]. It can be seen that the agreement is very good. Thus, the present code incorporating the Elrod's algorithm can handle the cavitation problem correctly.

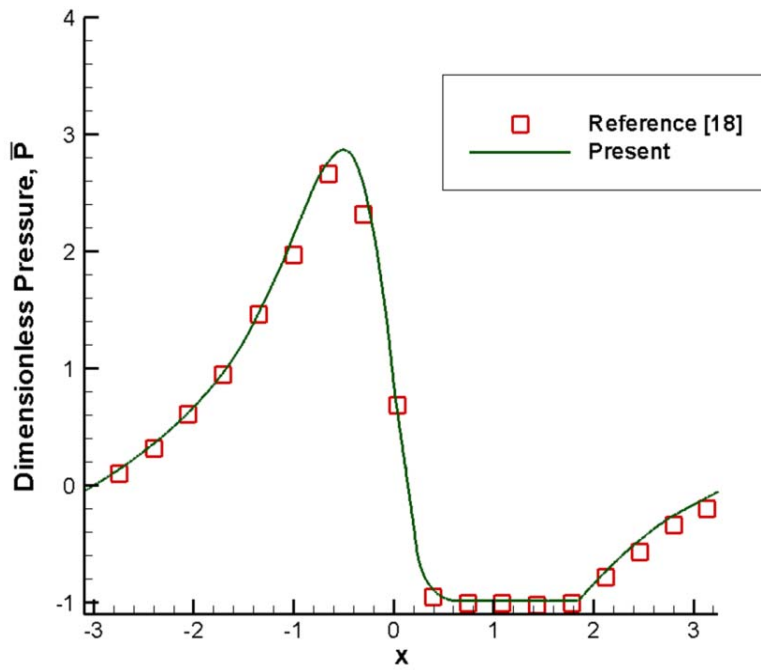
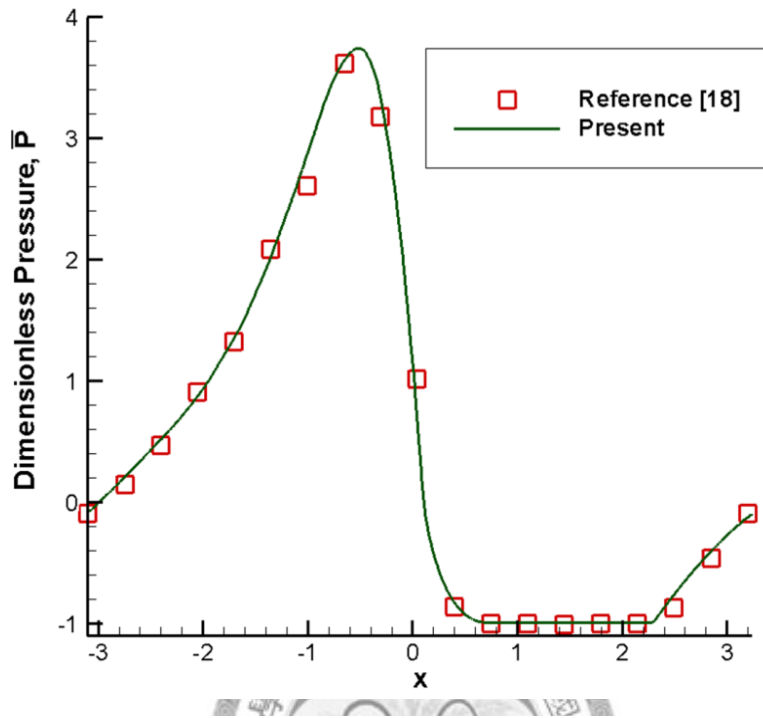
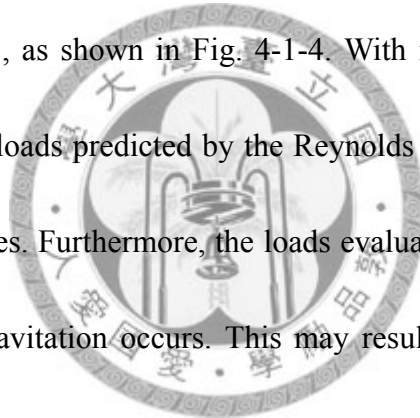


Fig. 4-1-3 Comparison of experimental data of reference [18] along circumference (a) axial position from centerline ($L/5D$), (b) axial position from centerline ($3L/5D$)

4-1.3.2 Load of a HGJB with cavitation

Fig. 4-1-2 shows a comparison of bearing load capacities, computed numerically by various methods. The present method, in which the groove-ridge discontinuity is considered, is more accurate in solving the load of the HGJBs than are the other numerical methods [8, 20]. Notably, other studies [8, 20] also applied Elrod's algorithm to the analysis of cavitation. For the case of Hirs' experiment, cavitation appears above an eccentricity ratio of 0.3, as shown in Fig. 4-1-4. With increases in the eccentricity ratio, the discrepancies of loads predicted by the Reynolds condition are greater due to the cavitation zone increases. Furthermore, the loads evaluated by the present treatment are more accurate when cavitation occurs. This may result from the consideration of conservation of mass at the groove-ridge region and at the cavitation inception concurrently by Elrod's algorithm. Further investigation is needed to understand this coupling effect.



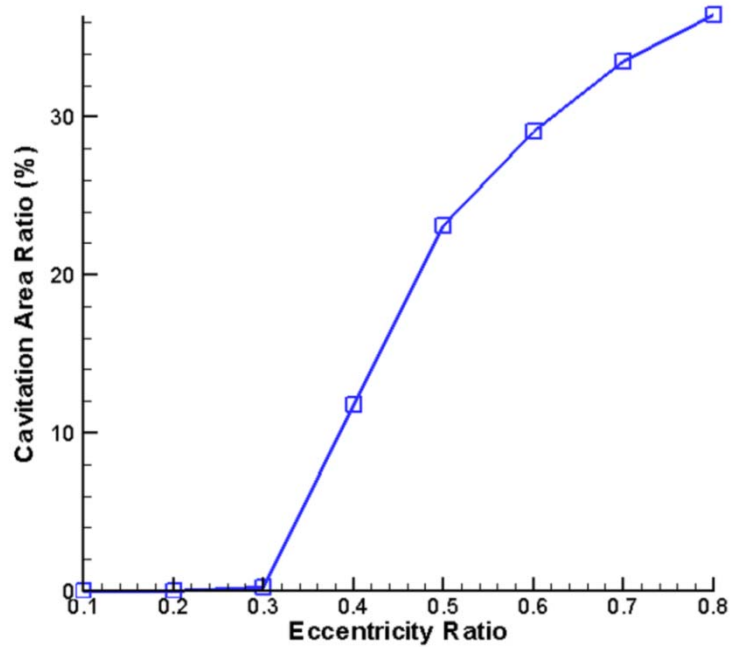


Fig. 4-1-4 Cavitation area ratio for the Hirs' experimental case

Fig. 4-1-5 plots the pressure distributions at the axial position from centerline $L/2$ of various eccentricity ratios, and indicates why cavitation occurs above the eccentricity ratio 0.3. As the eccentricity increases, the hydrodynamic pressure rises gradually in the converging film region and drops gradually to the ambient pressure or below its vapor pressure due to lubricant vaporization. Therefore, employing the present method with

Elrod's algorithm can improve the accuracy of calculating loads of HGJBs when cavitation occurs.

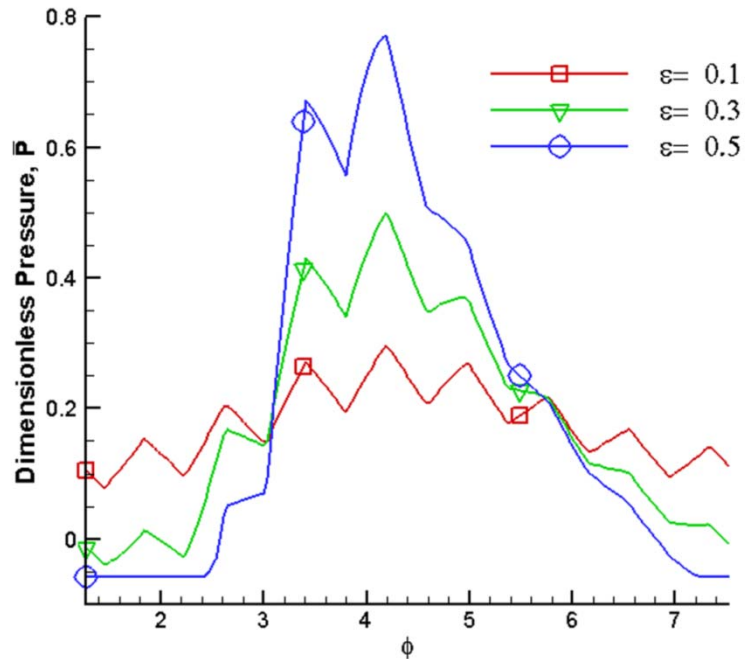


Fig. 4-1-5 Pressure distributions at the axial position from the centerline $L/2D$ under various eccentricity ratios

In summary, when cavitation does not occur, applying the groove-ridge discontinuity treatment show a good agreement with the data of Hirs. Furthermore, incorporating the Elrod's algorithm also gives a significant agreement when cavitation occurs. Thus, the proposed method can be employed with HGJBs.

4-1-4 Validation of EGJB

After the numerical program for the HGJB was validated, the numerical program of

the EGJB is validated here. Because no study has determined the performance of an EGJB numerically or experimentally, this study validates the EGJB program based on the numerical results of the HGJB program.

This work increases the number of groove sides of the HGJB to resemble the elliptical grooves asymptotically. To derive a groove of four sides, this work creates corner points of groove first. The corner points are obtained by dividing journal length into equal four parts, and inputs y-coordinates of these points into the elliptical groove equation. In the end, connect all corner points on a groove (Fig. 4-1-6). Similarly, a grooved journal bearing with 8 sides is obtained in this manner. Notably, when the number of groove sides increases, the shape of the grooved journal bearing is close to that of an ellipse.

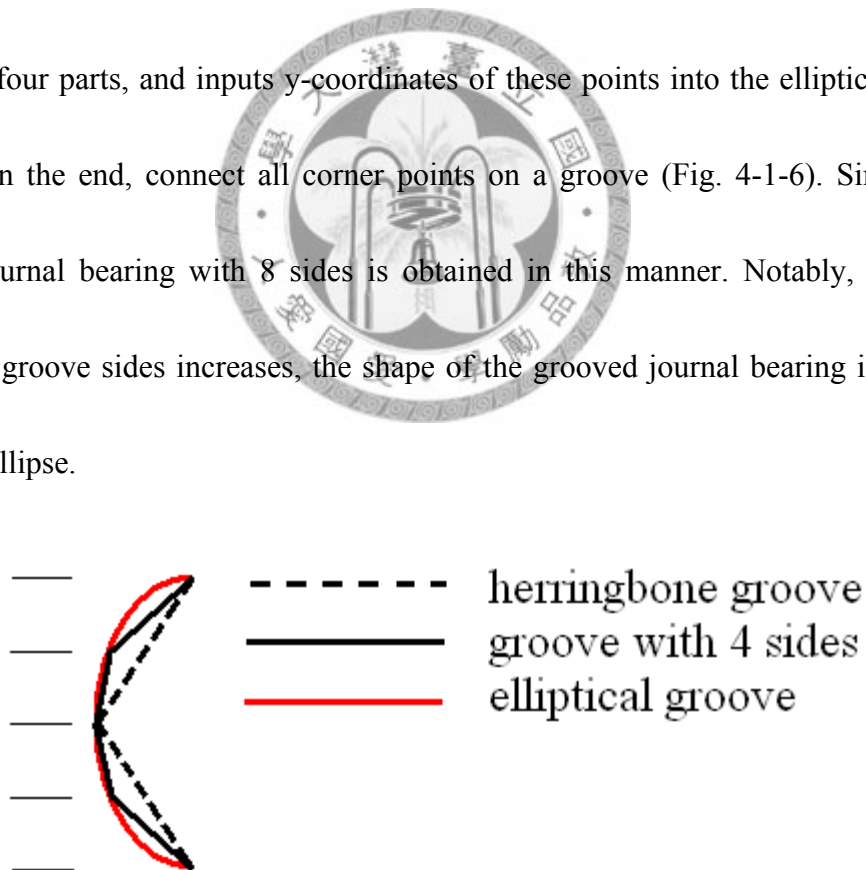


Fig. 4-1-6 Sketch of a herringbone groove, elliptical groove, and groove with four sides

Fig. 4-1-7 and Fig. 4-1-8 list the load capacities and radial stiffness of the EGJB, HGJB, and groove journal bearing with several sides. As the number of groove sides increases, load capacities and radial stiffness asymptotically approach that of the EGJB. From these reasonable values, we conclude that the code developed for analyzing the EGJB performance is also accurate.

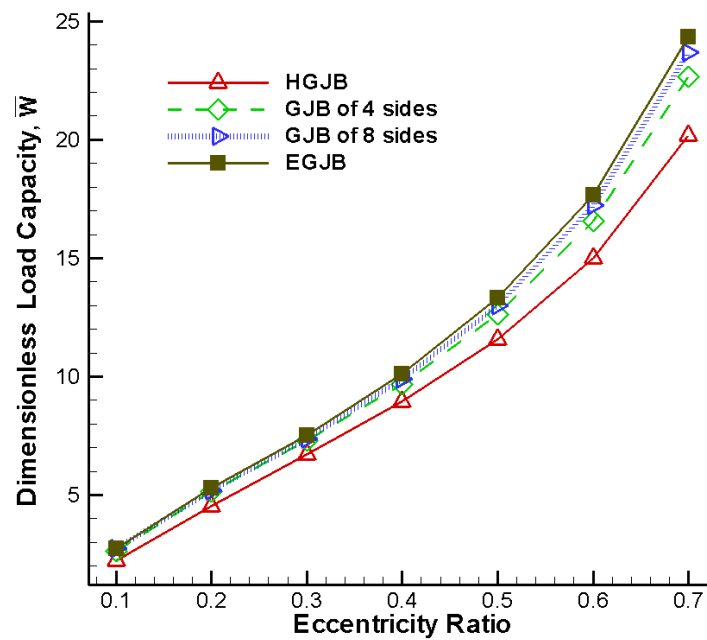


Fig. 4-1-7 Load capacities of the EGJB, HGJB, and groove journal bearing with several sides

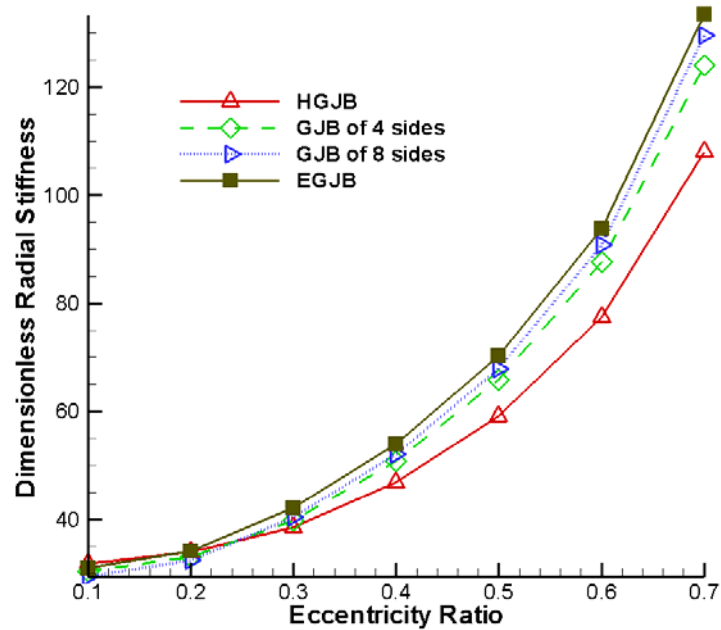


Fig. 4-1-8 Dimensionless radial stiffness of the EGJB, HGJB, and groove journal bearing with several sides



4-2 Validation of Critical Mass

Fig. 4-2-1 and Fig. 4-2-2 compare the attitude angle($=\tan^{-1} (\frac{W_t}{W_r})$) and dynamic coefficients(appendix A) associated with different groove angles with those published by Rao and Sawicki [17]. Our numerical results presented here are different from theirs and have a smoother variation with the groove angle. This difference may result from the disposition of the groove-ridge region when the result of Rao and Sawicki is determined using the FDM.

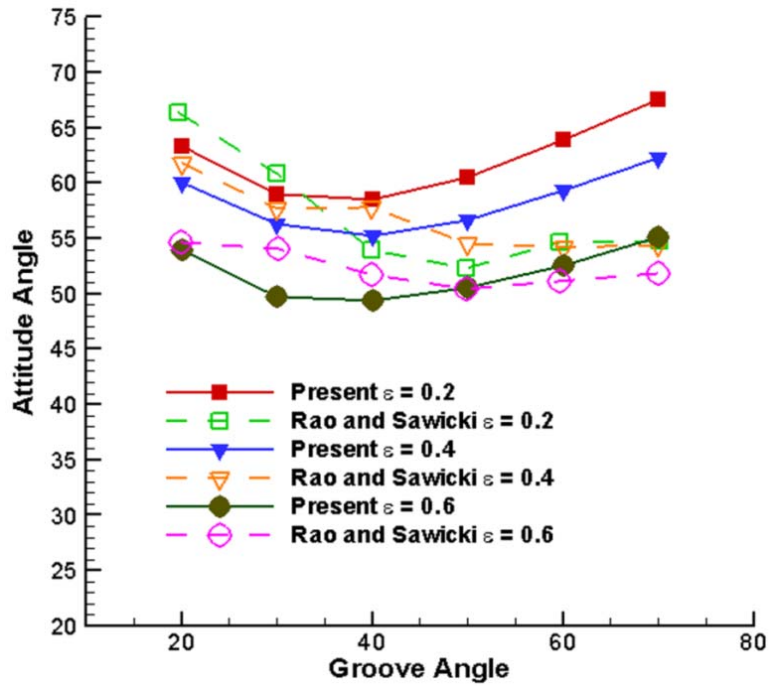


Fig. 4-2-1 Validation of attitude angle of HGJB with Rao and Sawicki [17]

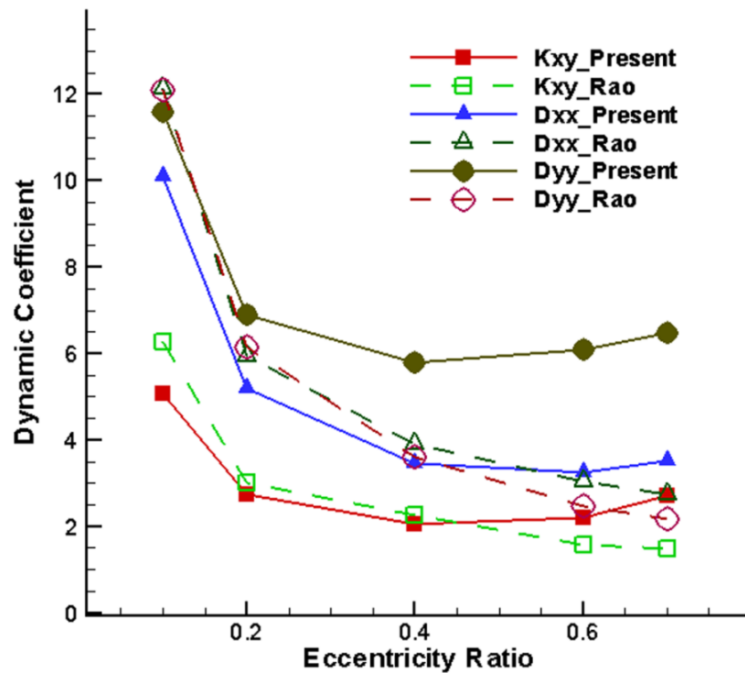


Fig. 4-2-2 Comparisons of HGJBs on dynamic coefficients with Rao and Sawicki [17] at a groove angle of 70°

Critical mass is derived in appendix A. Fig. 4-2-3 indicates that the relationship between critical mass and eccentricity approaches the analytical solution for a short plain journal bearing [35] as λ_k increases. Furthermore, to verify the critical mass of HGJB, the diameter to length ratio λ_k was fixed and the groove depth ratio decreased from 0.1 to 0.01 under the Reynolds condition. As the groove depth ratio was reduced, the critical mass of the HGJB approached that of a plain journal at $\lambda_k = 16$, as plotted in Fig. 4-2-4. Therefore, the code developed to evaluate critical mass is validated.

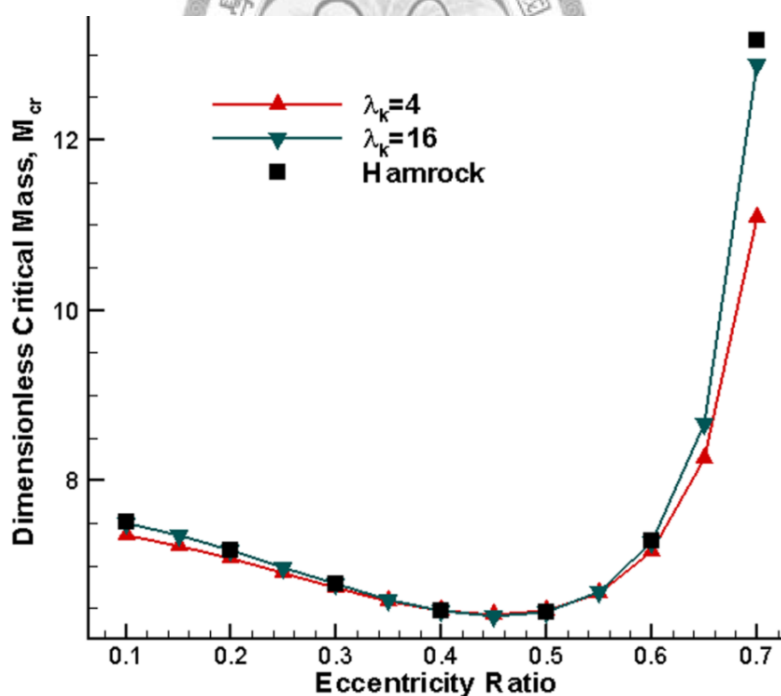


Fig. 4-2-3 Validation of dimensionless critical mass of a plain journal bearing with literature [35]

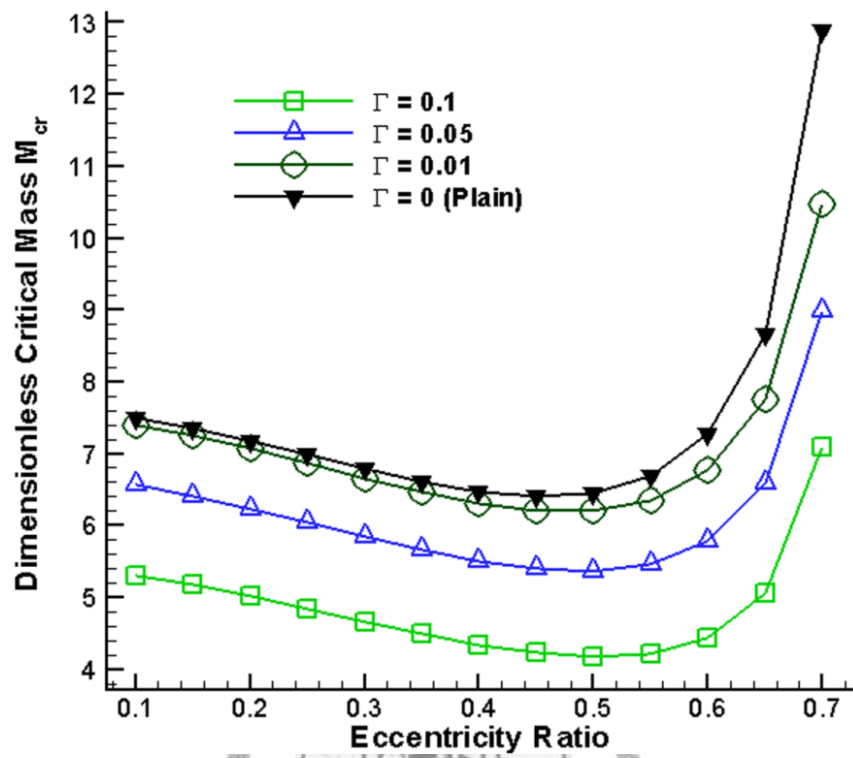


Fig. 4-2-4 Validation of HGJB on dimensionless critical mass





5. Effect of HGJB's Appearance on Stability

In the following, the operating eccentricity of the journal bearing is changed, and the critical mass is observed. Therefore, the influence of variations in the eccentricity and groove shapes on stability can be inferred.

There is no cavitation in the following cases. If cavitation occurs, the critical mass of the HGJB could also be analyzed by applying the perturbation method in the modified Reynolds equation with Elrod's algorithm.

5-1 Effect of Change in Groove Angle on Critical mass

As presented in Fig. 5-1-1, when the eccentricity is lower, the critical mass varies only slightly with groove angle. When the eccentricity ratio exceeds 0.4, the critical mass peaks at a groove angle of 20 degrees.

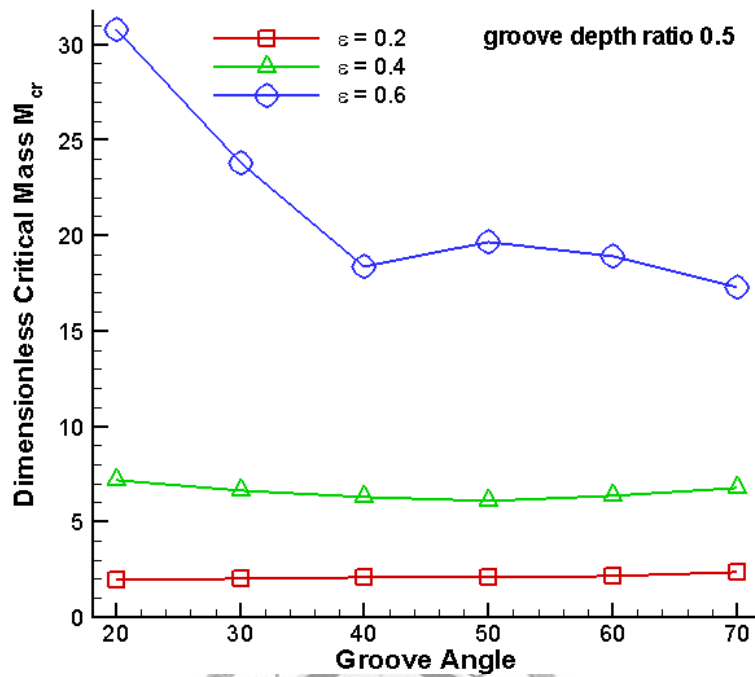


Fig. 5-1-1(a) Dimensionless critical mass at a groove depth ratio of 0.5

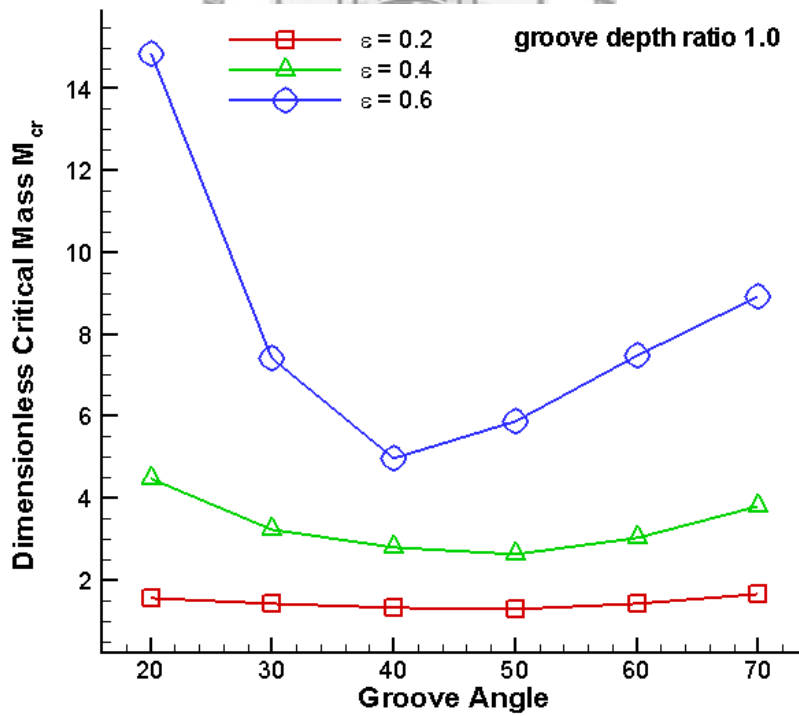


Fig. 5-1-1(b) Dimensionless critical mass at a groove depth ratio of 1.0

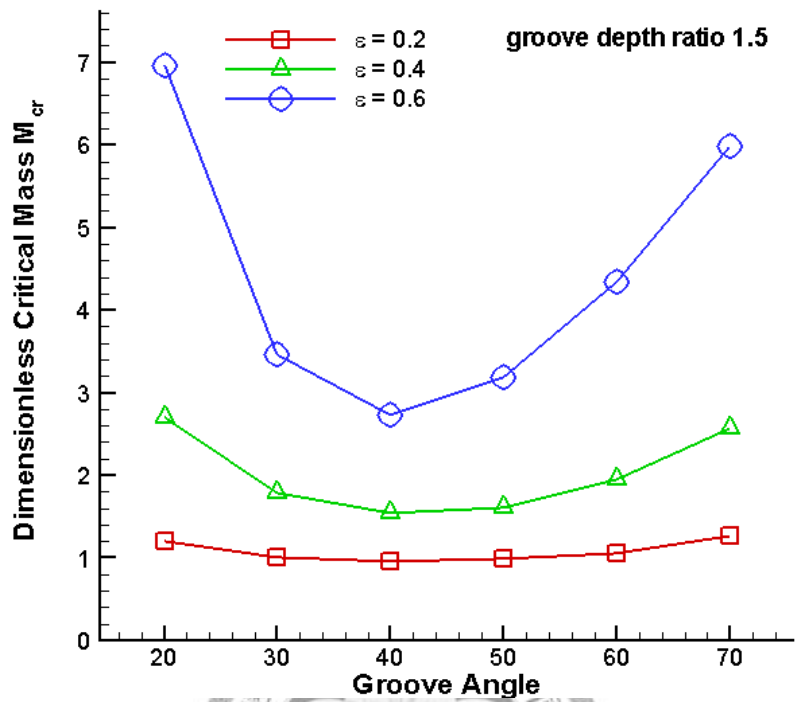


Fig. 5-1-1(c) Dimensionless critical mass at a groove depth ratio of 1.5

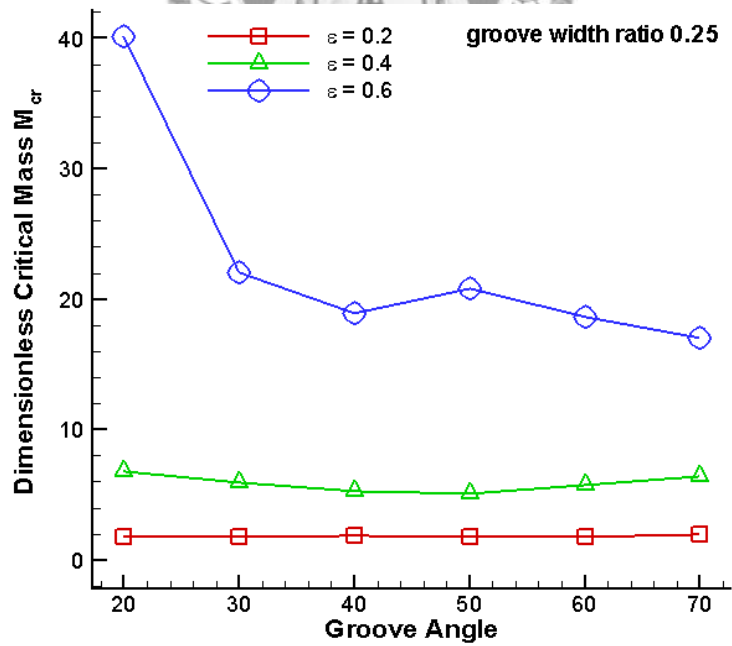


Fig. 5-1-2 (a) Dimensionless critical mass ϵ at a groove width ratio of 0.25

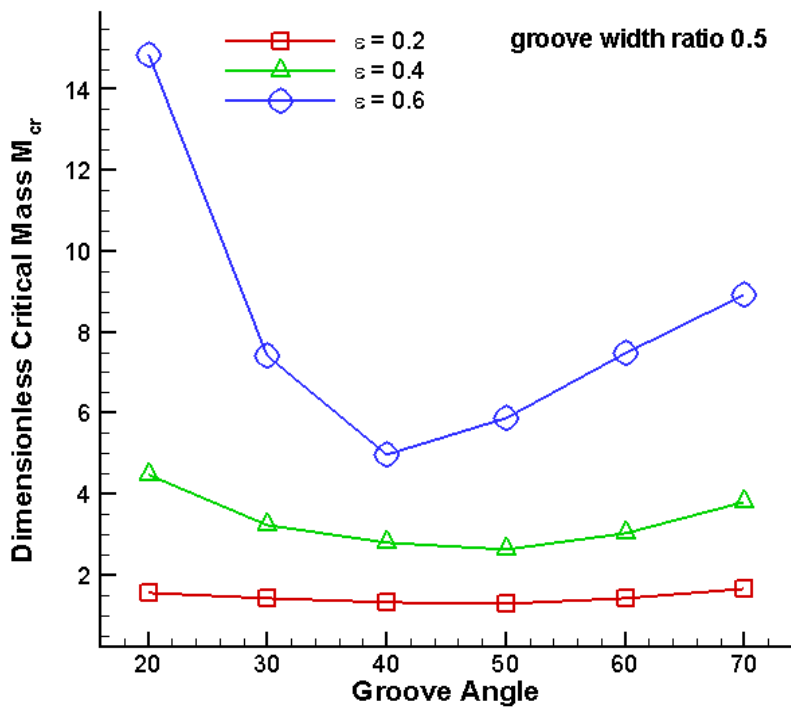


Fig. 5-1-2(b) Dimensionless critical mass at a groove width ratio of 0.5

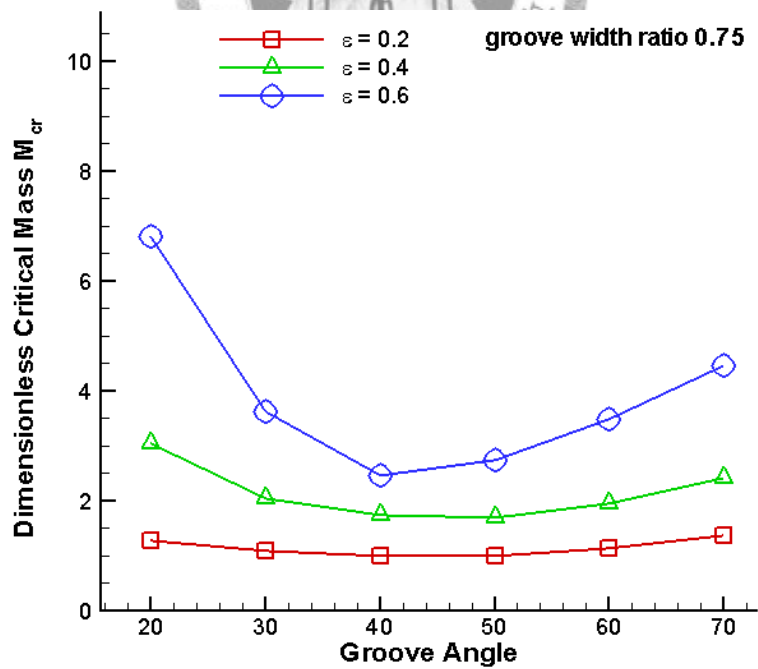
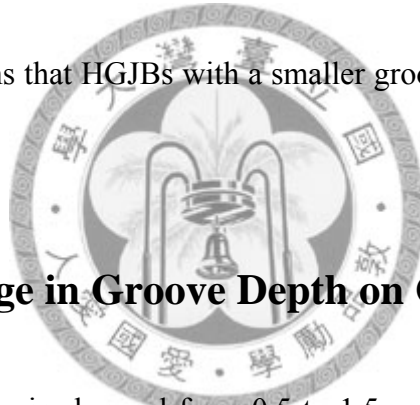


Fig. 5-1-2(c) Dimensionless critical mass at a groove width ratio of 0.75

The distribution of the critical masses associated with a change in groove angles, as reported in another study [17], is less smooth than that determined in the present work. This difference may result from the improper disposal in the groove-ridge region; i.e., the pressure was evaluated using the FDM.

The influence of the groove angle on the critical mass is as follows. As the eccentricity increases, the critical mass of the bearing increases faster as the groove angle decreases. This means that HGJBs with a smaller groove angle are more sensitive to a change in eccentricity.



5-2 Effect of Change in Groove Depth on Critical mass

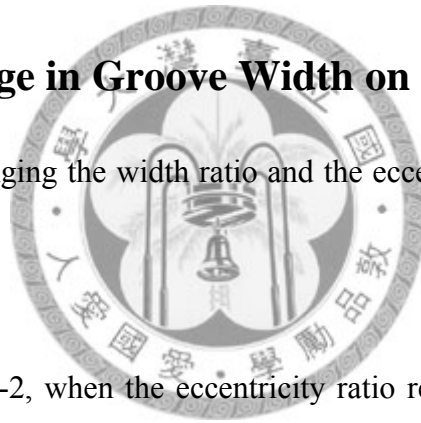
The groove depth ratio is changed from 0.5 to 1.5, with other groove parameters remaining unchanged. The following sections discuss the influence of the groove depth ratio and the eccentricity on the critical mass.

As presented in Fig. 5-1-1, for a fixed eccentricity, the critical mass decreases as the groove depth ratio increases. The critical mass peaks at a groove depth ratio of 0.5; i.e., the bearing with shallower grooves has a larger critical mass. However, as the

eccentricity ratio increases, the critical mass of the HGJBs also increases rapidly with lower groove depth. Hence, for HGJBs with shallow grooves, the critical mass is sensitive to variations in eccentricity ratio when the eccentricity is large. In contrast, for bearings with deeper grooves, the critical mass increases less with an increase in eccentricity, indicating that the critical mass is insensitive to the eccentricity for HGJBs with large groove depths.

5-3 Effect of Change in Groove Width on Critical Mass

The influence of changing the width ratio and the eccentricity on the critical mass are discussed below.



As shown in Fig. 5-1-2, when the eccentricity ratio remains constant, the critical mass decreases as the groove width ratio increases. A larger eccentricity ratio corresponds to greater changes in critical mass.

The critical mass peaks at a groove width ratio of 0.25. The degree of variation in the critical mass varies with the groove width. When the groove width ratio increases over 0.5, the variation in the critical mass decreases.

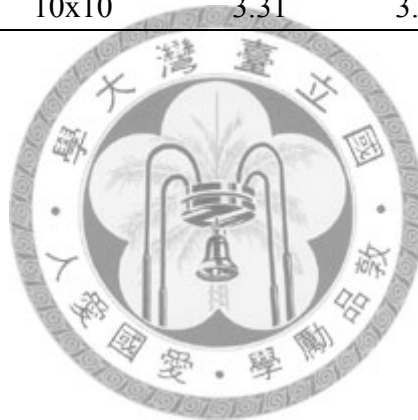
As the eccentricity increases, the critical mass of HGJBs with narrow grooves increases rapidly. Specifically, the critical mass of HGJBs with smaller groove widths is more sensitive to variations in the eccentricity ratio. However, when the eccentricity ratio is high, the critical masses vary little with groove width for HGJBs with large groove widths, even though a larger groove width reduces stability. Restated, at a high eccentricity, the critical mass of a HGJB with wide grooves is insensitive to variations in the eccentricity ratio.

5-4 Efficiency of the Present Method on Critical Mass

In order to show the efficiency of the present method, Table 5-4-1 shows the CPU time needed to obtain the load capacity of a bearing with 8 grooves on the stationary surface, at an eccentricity ratio of 0.5 for various nodal points. This work was compiled with Compaq Visual Fortran 6.6 on a 1.50GHz Intel Pentium M processor. Thus, the present method is efficient for analyzing HGJB problems.

Table 5-4-1 The CPU time needed to obtain the load capacity of a bearing with 8 grooves on the stationary surface, at an eccentricity ratio of 0.5 for various nodal points (groove angle=40°)

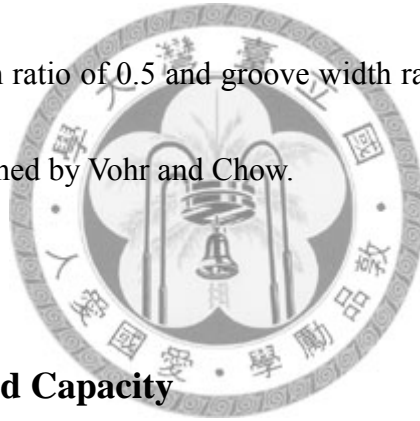
Elements	Nodes	CPU time (s)	Load capacity	Deviation
136	4x4	0.23	3.562	-0.89%
136	5x5	0.39	3.58	-0.39%
136	6x6	0.75	3.587	-0.19%
136	7x7	1.17	3.59	-0.11%
136	8x8	1.48	3.592	-0.06%
136	9x9	2.23	3.593	-0.03%
136	10x10	3.31	3.594	0.00%



6. Performance Enhancement Using Elliptical Grooves

6-1 Performance of EGJB

To assess the utility of the proposed EGJB, the load capacity is compared with the conventional HGJB by Vohr and Chow[29]. Comparisons are obtained using numerical results. The optimum groove parameter for the HGJB obtained by Vohr and Chow with groove angle of 32.8° corresponds the parameter for the EJGB with an elliptical axis ratio of 1.55. Groove depth ratio of 0.5 and groove width ratio of 2.1 used are the same as those of the HGJB obtained by Vohr and Chow.



6-1-1 Effect on Load Capacity

Effect of load capacity on the location of grooves on the HGJB and EGJB are shown in Figs. Fig. 6-1-1 and Fig. 6-1-2. Fig. 6-1-1 shows that when the bearing is grooved, load capacity of the EGJB is about 15% greater than that of the HGJB. Additionally, as bearing length increases, the load capacity of the EGJB increases. When length-diameter ratio is 2, the load capacity of the EGJB is up to 30% more than that of the HGJB.

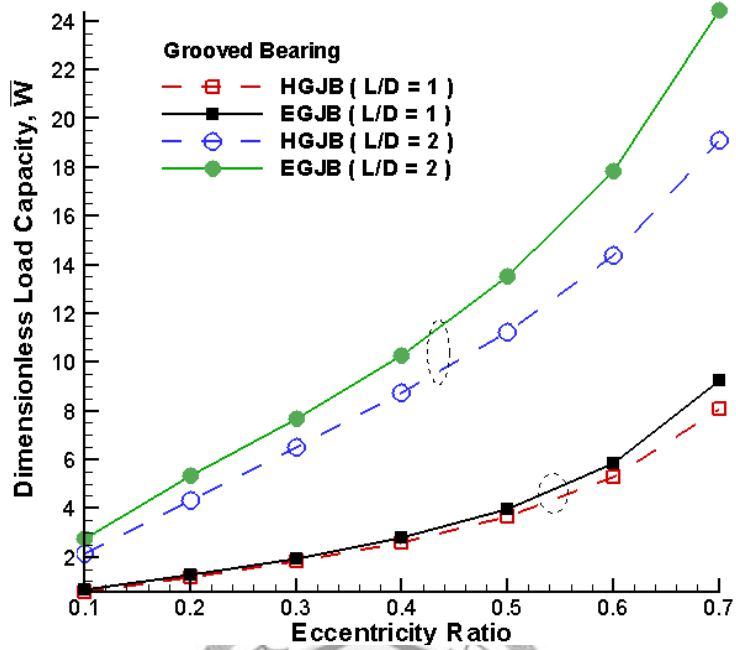


Fig. 6-1-1 Load capacities with various eccentricity ratios for grooved bearings

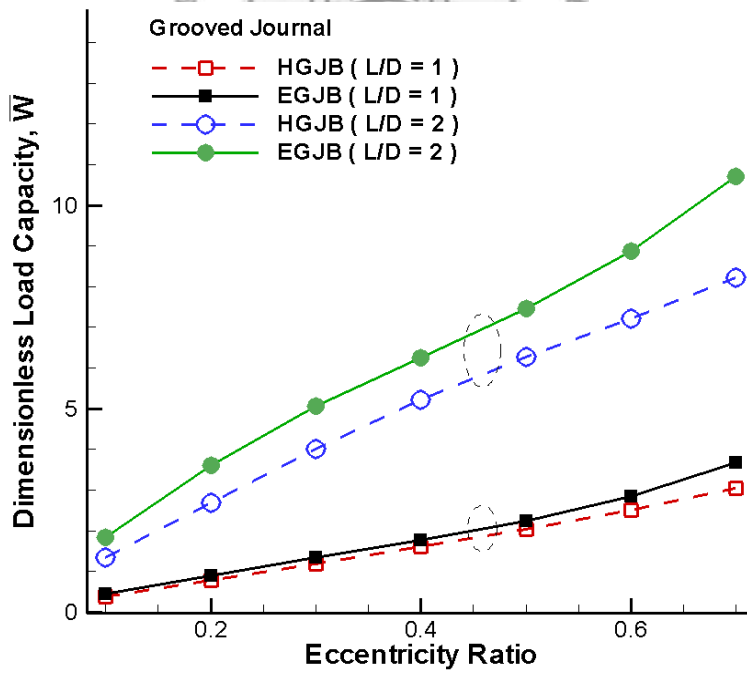
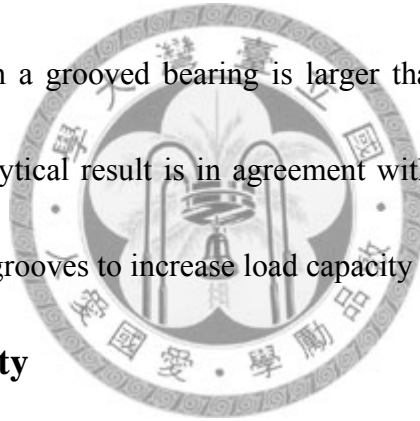


Fig. 6-1-2 Variations in load capacities with different eccentricity ratios for grooved journals

Fig. 6-1-2 shows that the load capacity of the EGJB is larger than that of HGJB when the journal is grooved. Comparing the load capacity of EGJB with that of HGJB indicates that the increase in load capacity of the EGJB with a grooved journal is greater than that of the EGJB with a grooved bearing.

As a summary, more load capacity of the EGJB than that of HGJB can be gained no matter where the grooves are located in the bearing or journal. Additionally, the load capacity of the EGJB with a grooved bearing is larger than that of the EGJB with a grooved journal. This analytical result is in agreement with those in literature [6, 29]. Hence, adopting elliptical grooves to increase load capacity is beneficial.



6-1-2 Effect on Stability

After determining the load capacity of the EGJB, the stability of the HGJB and EGJB are compared. Fig. 6-1-3 compares dimensionless radial stiffness of the EGJB at various eccentricity ratios and length-diameter ratios with those of the HGJB.

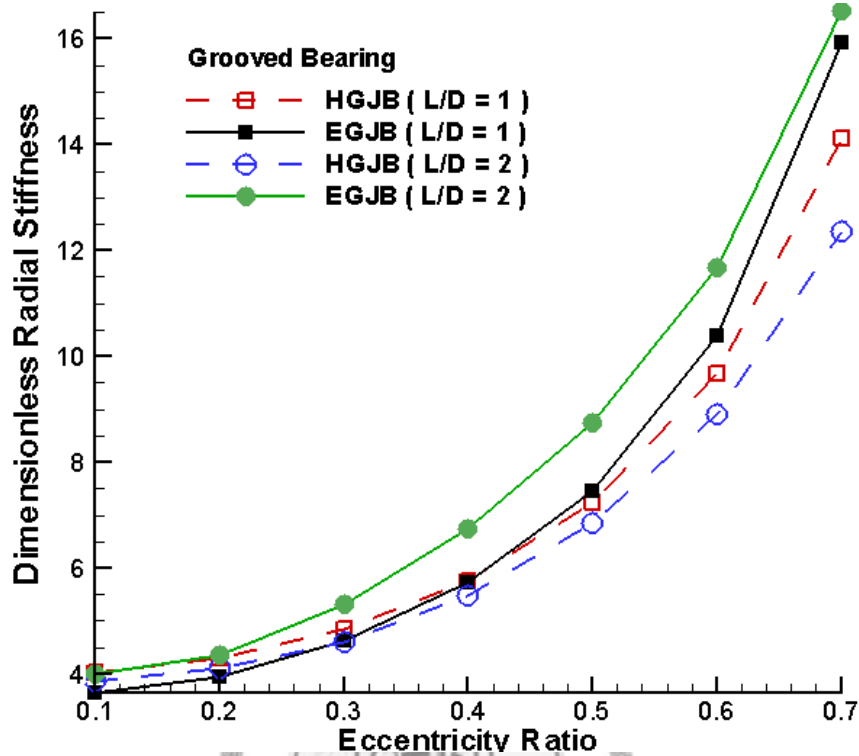


Fig. 6-1-3 Dimensionless radial stiffness of the EGJB and HGJB with various eccentricity ratios and length-diameter ratios and for a grooved bearing

At a low eccentricity ratio, the dimensionless radial stiffness of the EGJB does not differ markedly from that of the HGJB. When the eccentricity ratio exceeds 0.3, the dimensionless radial stiffness of the EGJB is consistently larger than those of the HGJB. At an eccentricity ratio of 0.6, the dimensionless radial stiffness of the EGJB is 25% greater than those for the HGJB. Moreover, for the grooved journal (Fig. 6-1-4), the dimensionless radial stiffness of the EGJB does not differ significantly from those of the HGJB at a low eccentricity ratio, but are consistently greater than those of the HGJB

when the eccentricity ratio exceeds 0.3, which is same as the dimensionless radial stiffness of the grooved bearing.

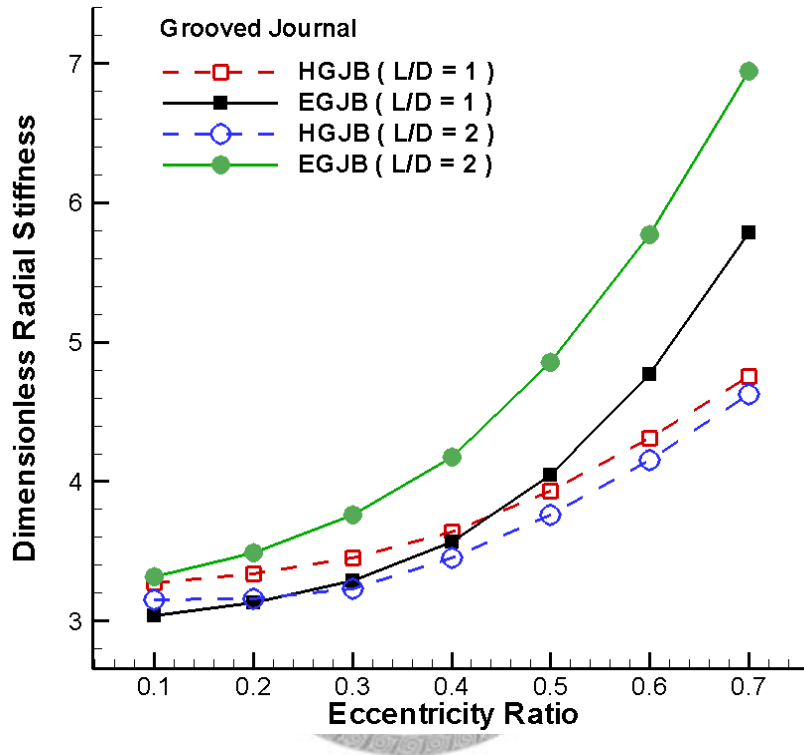


Fig. 6-1-4 Dimensionless radial stiffness of the EGJB and HGJB with various eccentricity ratios and length-diameter ratios for grooved journals

6-1-3 Effect on Side Leakage

Side leakage is also an important characteristic for hydrodynamic journal bearings.

Leakage, which results from the impact between rotating and stationary parts, reduces

load capacity. As shown in Fig. 6-1-5, when the eccentricity ratio is low, side leakage of

the EGJB decreases notably compared with that of the HGJB. This difference may

result from elliptical grooves reducing the leakage in the end of bearing. Therefore, we conclude that in the case of optimum groove geometry of the HGJB, the performance of the EGJB is superior to that of the HGJB in terms of load capacity, radial stiffness, and side leakage.

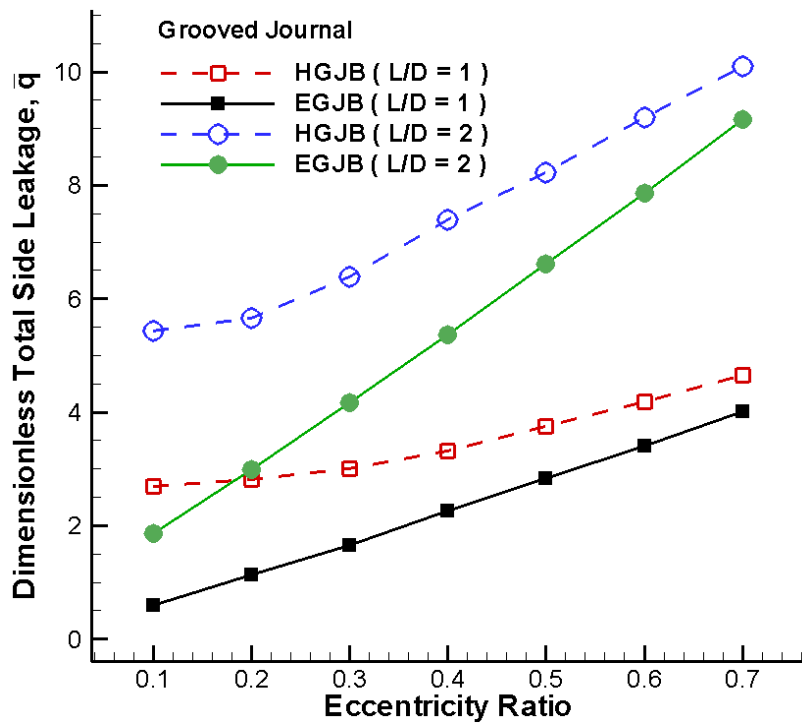


Fig. 6-1-5(a) Dimensionless total side leakage of the EGJB and HGJB with various eccentricity ratios and length-diameter ratios for grooved journals

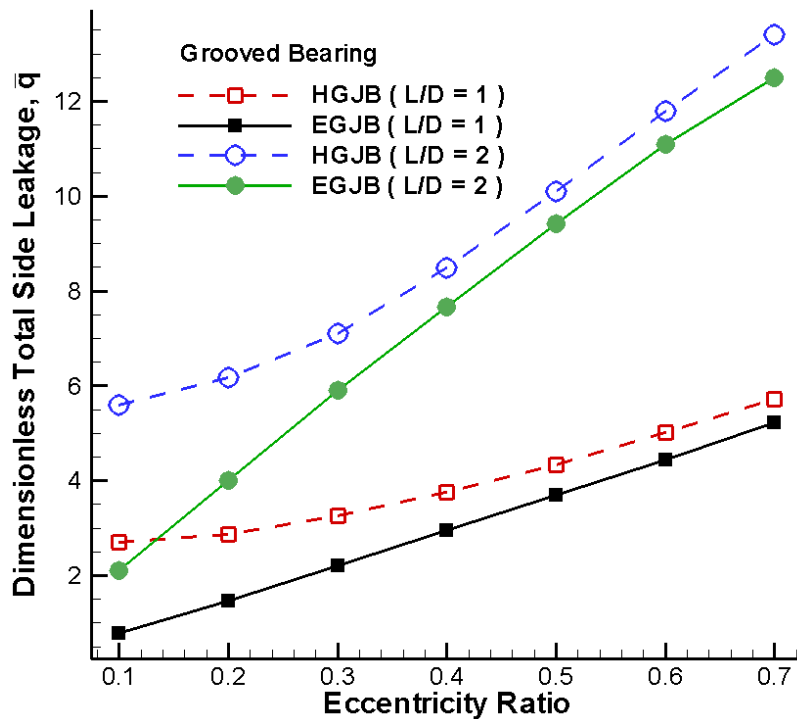


Fig. 6-1-5 (b) Dimensionless total side leakage of the EGJB and HGJB with various eccentricity ratios and length-diameter ratios for grooved bearings

6-1-4 Effect on Reducing Cavitation

The cavitation region in the fluid film of the HGJB and EGJB is discussed in this section. The groove parameter used here for the HGJB is also obtained by Vohr and Chow. Fig. 6-1-6 and Fig. 6-1-7 show the load capacities of the HGJB and EGJB with the increase of eccentricity ratio. It can be seen that when journal load is fixed, the operating eccentricity of EGJB is obviously lower than that of HGJB. This may be because the high pressure region of EGJB is markedly larger than that of HGJB.

Table 6-1-1 and Table 6-1-2 show the cavitation ratio of the HGJB and EGJB at an eccentricity ratio of 0.1 to 0.9. Comparing the cavitation ratio of the EGJB with that of HGJB indicates that the adopting of elliptical groove can reduce the cavitation when the load of HGJB and EGJB is same.

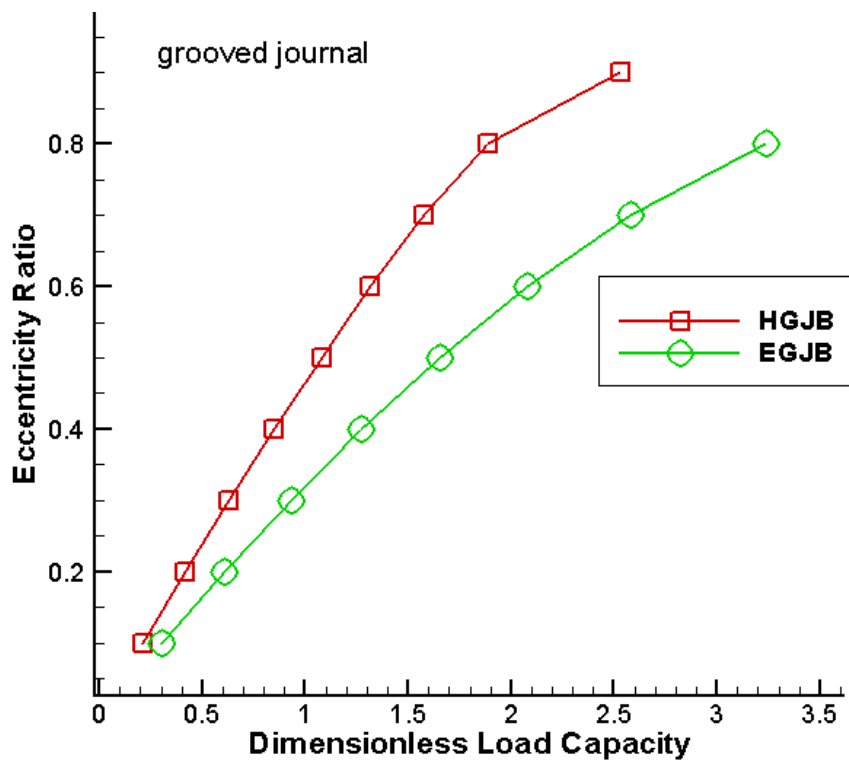


Fig. 6-1-6 Load of the HGJB and EGJB for a grooved journal with optimum groove parameter

Table 6-1-1 The Cavitation ratio of the HGJB and EGJB for a grooved journal with optimum groove parameter

Eccentricity ratio	HGJB	EGJB
0.1	0	0
0.2	0	0
0.3	0	0
0.4	0	0
0.5	0	0
0.6	0	0
0.7	0	0
0.8	0	0.915
0.9	1.31	

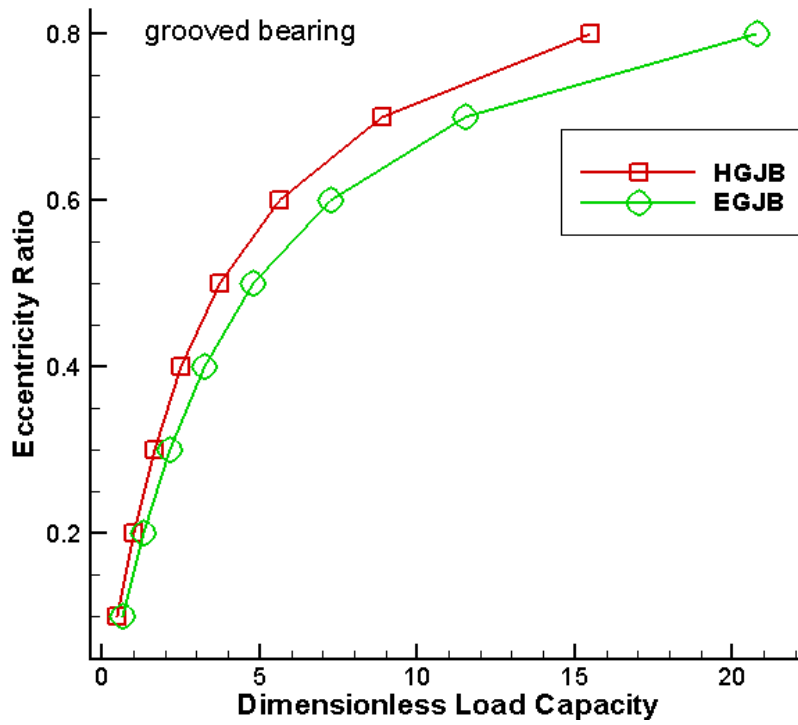


Fig. 6-1-7 Load of the HGJB and EGJB for a grooved bearing with optimum groove parameter

Table 6-1-2 The Cavitation ratio of the HGJB and EGJB for a grooved bearing with optimum groove parameter

Eccentricity ratio	HGJB	EGJB
0.1	0	0
0.2	0	0
0.3	0	0
0.4	0	0
0.5	0	0
0.6	0	0
0.7	0	0
0.8	0.551	1.255

6-2 Optimum Groove Parameters for Stability

The optimum groove parameters for maximum radial force of the EGJB are investigated in this section. Since groove geometry has several parameters, this work simplifies the processes for seeking the optimum groove parameters as follows. Firstly, groove width is fixed, while the elliptical axis ratio and groove depth are varied. Then groove depth is fixed to the value, determined by maximum radial force in the previous step, while the elliptical axis ratio and the groove width are varied. Via these procedures, the optimum groove parameters are identified. Table 6-2-1 presents geometrical

parameters of the EGJB.

Table 6-2-1 Design parameters of the EGJB

Clearance, c	6×10^{-6} (m)
Radius, r	0.002 (m)
Length, L	0.004 (m)
Fluid viscosity, μ	0.00124 (Pa·s)
Number of grooves	8
Groove depth ratio, Γ	1.0
Groove width ratio, δ	0.5
Journal speed, ω	5000 (rpm)
Groove location	on bearing

Fig. 6-2-1 shows the dimensionless radial stiffness with a groove width ratio of 0.5 for various eccentricity ratios. As the groove depth ratio increases from 0.5 to 1.0, the dimensionless radial stiffness increases rapidly. However, when the groove depth ratio increases further, the dimensionless radial stiffness varies a little. It can be seen that the dimensionless radial stiffness reaches the maximum as the groove depth ratio is 2.0. When the groove depth ratio exceeds 2.0, the dimensionless radial stiffness decreases.

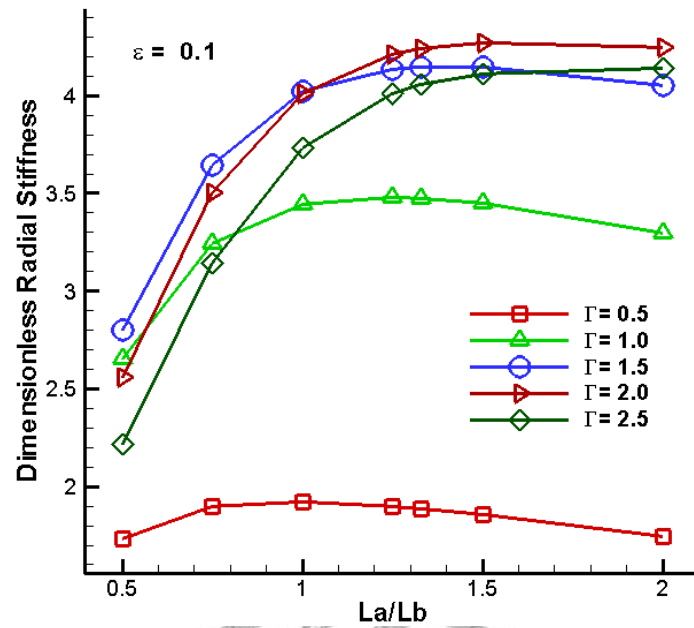


Fig. 6-2-1(a) Dimensionless radial stiffness under a groove width ratio of 0.5 and eccentricity ratio of 0.1

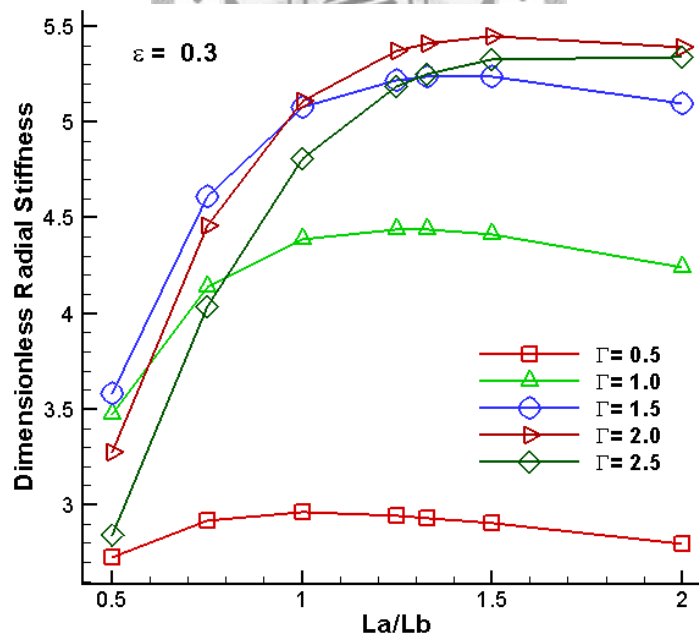


Fig. 6-2-1(b) Dimensionless radial stiffness under a groove width ratio of 0.5 and eccentricity ratio of 0.3

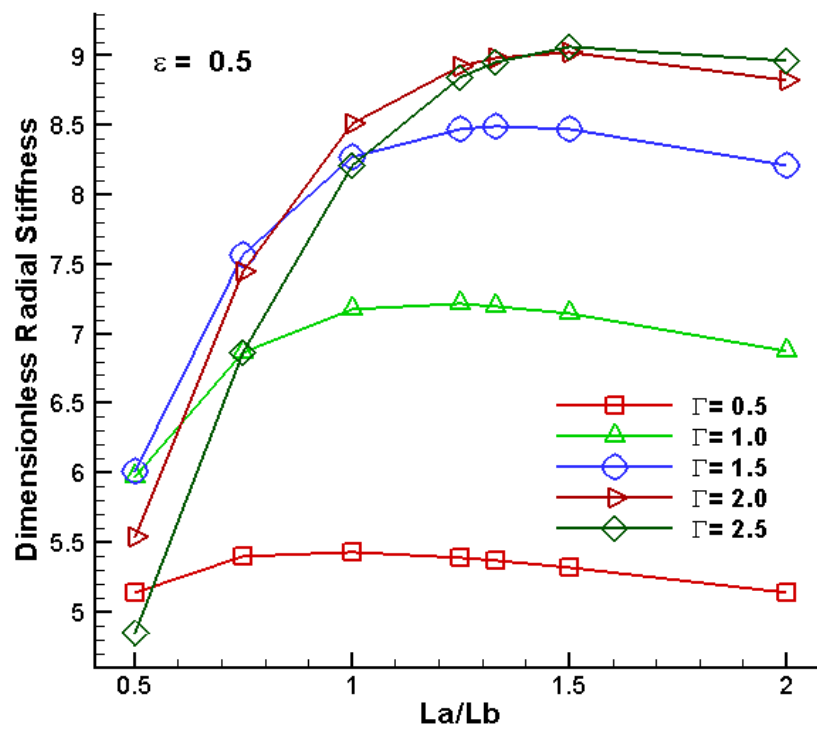


Fig. 6-2-1(c) Dimensionless radial stiffness under a groove width ratio of 0.5 and eccentricity ratio of 0.5

The optimum groove parameters for different groove widths are studied as follows.

The groove depth ratio is fixed at 2.0 which maximize the dimensionless radial stiffness from the discussion above. The elliptical axis ratio is increased from 0.5 to 2 and the groove width ratio is increased from 0.3 to 0.7 (Fig. 6-2-2). It can also be seen that a suitable groove width increases stability for all three eccentricity ratios. When the groove width ratio is 0.5, the dimensionless radial stiffness peaks at an elliptical axis ratio of 1.5. In summary, the optimum groove parameter values for EGJB are a groove

width ratio of 0.5, groove depth ratio of 2.0, and elliptical axis ratio of 1.5. These optimum groove parameters are close to those obtained by Vohr and Chow [29].

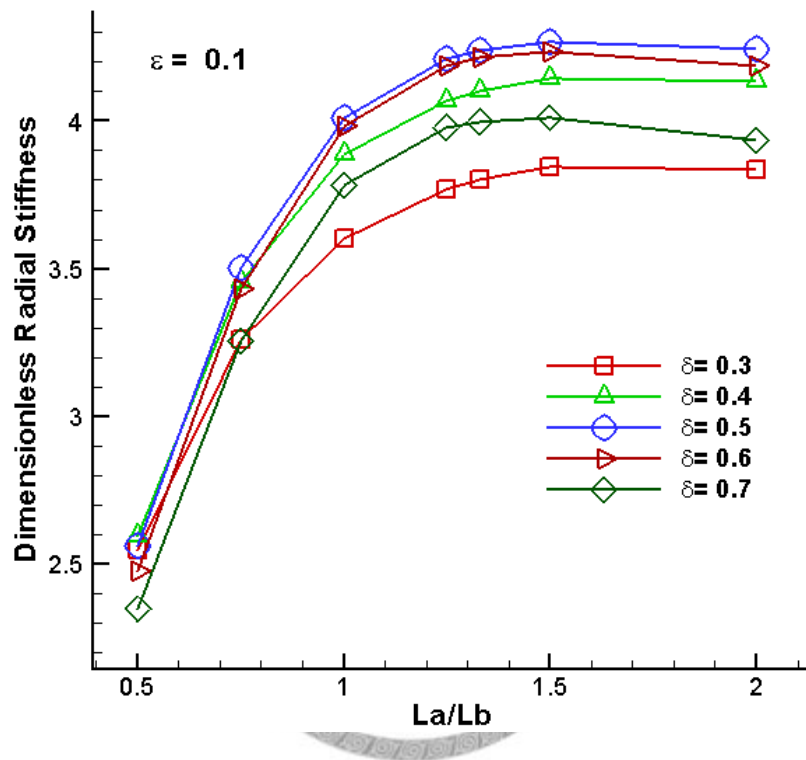


Fig. 6-2-2(a) Dimensionless radial stiffness under a groove depth ratio of 2.0 and eccentricity ratio of 0.1

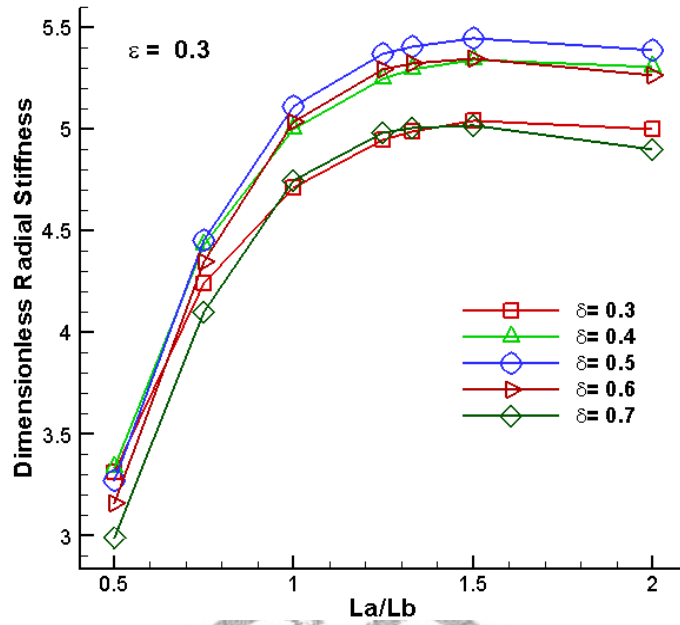


Fig. 6-2-2(b) Dimensionless radial stiffness under a groove depth ratio of 2.0 and eccentricity ratio of 0.3

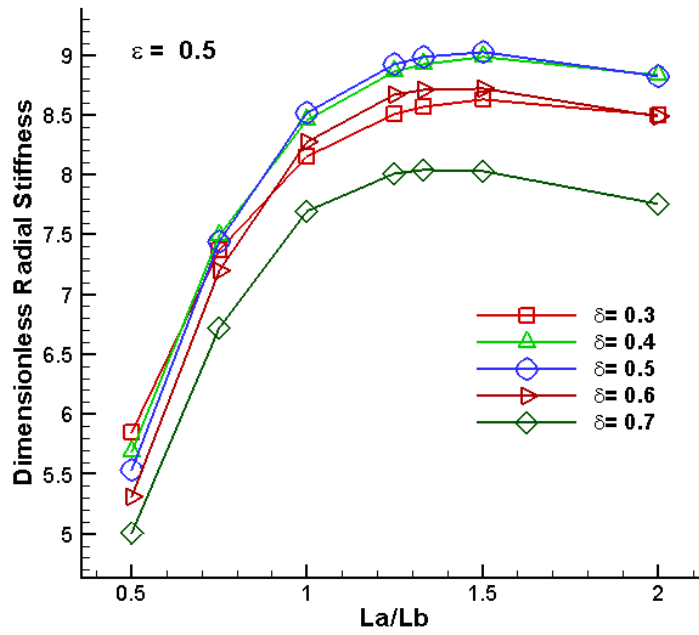
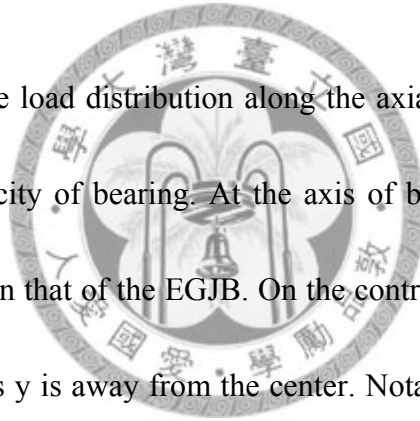


Fig. 6-2-2(c) Dimensionless radial stiffness under a groove depth ratio of 2.0 and eccentricity ratio of 0.5

6-3 Comparison of the Load Distribution

To examine how elliptical grooves impact load characteristics, the multi-sided herringbone-grooved journal bearings with 4 sides and 8 sides, are used to investigate differences in the load distributions of fluid film. Operating conditions used are groove angle of 37° , groove depth ratio of 1.0, groove width ratio of 0.5, and eccentricity ratio of 0.4. The corresponding elliptical axis ratio is 1.327.

Fig. 6-3-1 presents the load distribution along the axial direction. The area below the curve is the load capacity of bearing. At the axis of bearing symmetry ($y=0$), the load of HGJB is higher than that of the EGJB. On the contrary, the load of the HGJB is lower than that of EGJB as y is away from the center. Notably, the load distribution of the grooved journal bearing with 4 sides is close to that of the EGJB.



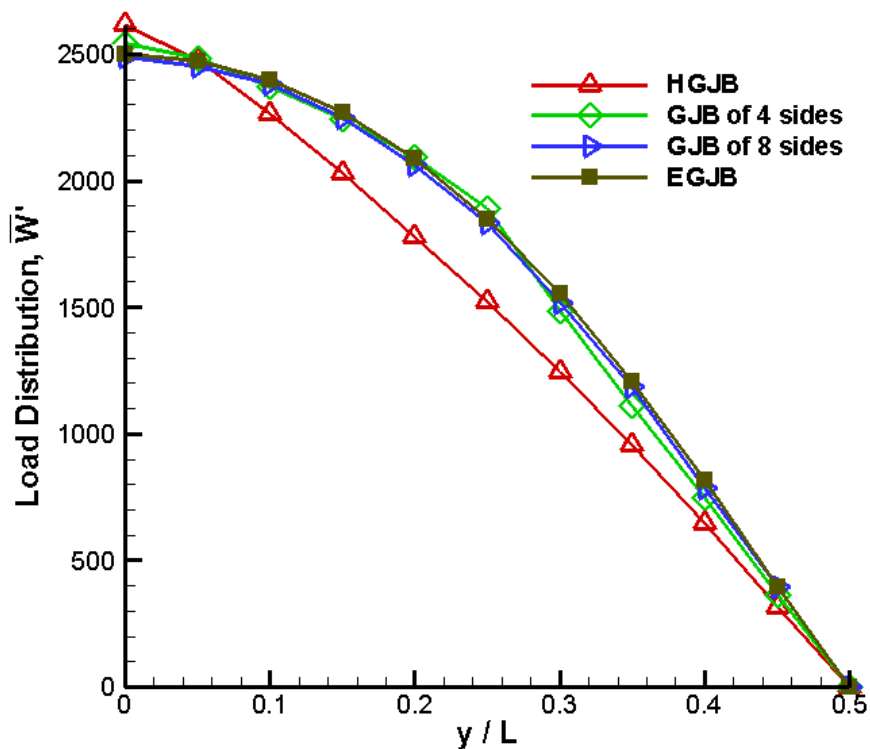
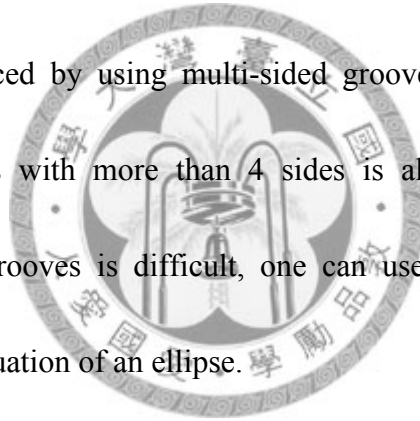


Fig. 6-3-1 The distribution of load capacity along the axial direction

It can also be seen that the load distribution of EGJB along the axial direction is more uniform than that of HGJB. The low load at the bearing center of EGJB may be offset by the load away from the bearing center; thus, a higher total load capacity for the EGJB than that of HGJB is achieved. The same trend of the load distribution along the axial direction for the other operation conditions can also be found. On the other hand, the load capacities of grooved journal bearing with 4 sides are close to that of the EGJB.

Hence, resembling an elliptical shape with grooves with more than 4 sides is unnecessary.

As is well known, axial leakage is proportional to the pressure gradient at both ends of the bearing. Fig. 6-3-2 shows total side leakage of grooved bearings. EGJB can lower the leakages of the lubricants with the curvature variation of the elliptical shape. Accordingly, side leakage of the HGJB is greater than that of EGJB. In addition, side leakage can also be reduced by using multi-sided grooves. However, reducing side leakage by using grooves with more than 4 sides is also unnecessary. Supposing manufacturing elliptical grooves is difficult, one can use multi-side grooves whose corner points are on the equation of an ellipse.



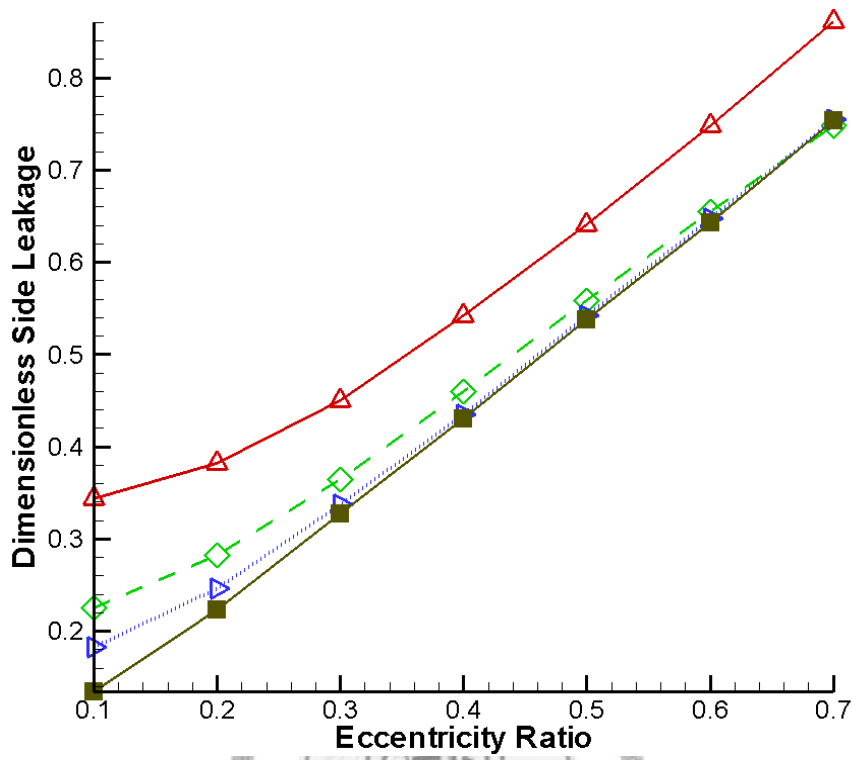


Fig. 6-3-2 Total Side leakage of the EGJB, HGJB and grooved journal bearings with 4 and 8 sides





7. Performance Enhancement on Rev-EGJB

This chapter proposes a novel reversible rotation journal bearing with elliptical grooves (Rev-EGJB). Instead of a helical groove, the elliptical groove is adopted to improve the performance of the reversible rotation HGJB (Rev-HGJB). A numerical program is used to analyze the appearance and characteristics of the Rev-EGJB. To calculate the pressure distribution of a fluid film, the Reynolds equation was solved using the SEM [38]. The load distributions of the reverse rotation grooved journal bearings are compared to elucidate how elliptical grooves enhance load characteristics. Load capacity, power loss, and the stability parameter are compared with those of the Rev-HGJB. Finally, the Rev-EGJB's configuration, which maximizes radial force, is investigated.

7-1 Groove Profile

Fig. 7-1-1 shows the shape of the elliptical grooves. Since variation in elliptical shape affects the pressure distribution of a fluid film, in this work the elliptical axis ratio is varied to investigate how the shapes of elliptical grooves affect Rev-EGJB

performance.

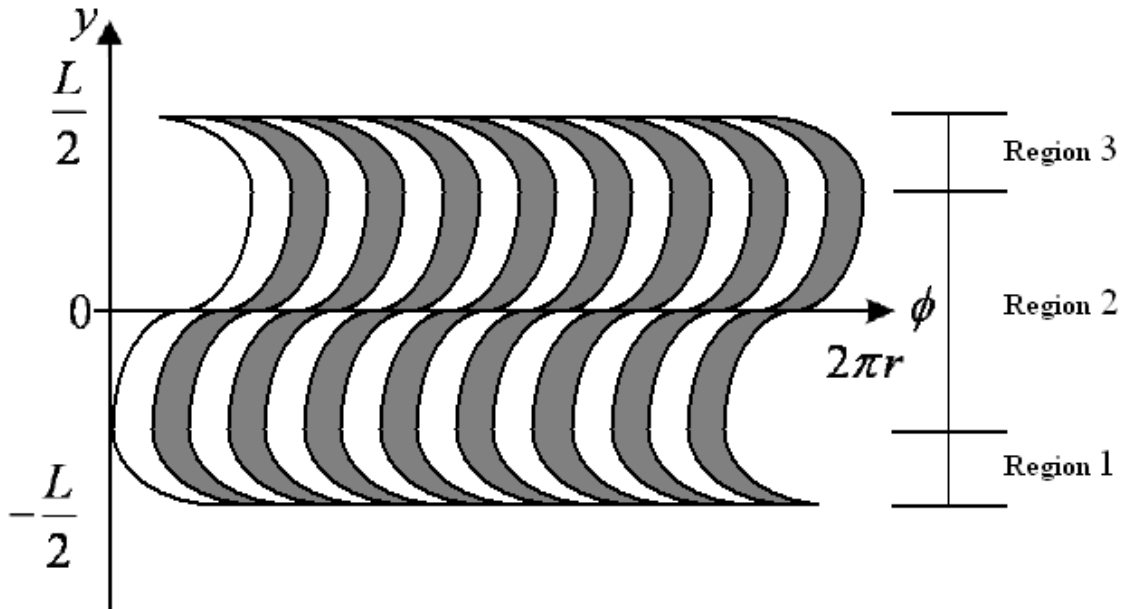


Fig. 7-1-1 The shape of the reversible rotation journal bearing with elliptical grooves

The equation of the ellipse is:

$$\frac{(x-x_0)^2}{L_a^2} + \frac{(y-y_0)^2}{L_b^2} = 1 \quad (7-1),$$

where the center of the ellipse is at (x_0, y_0) , and L_a and L_b are the axis length in the

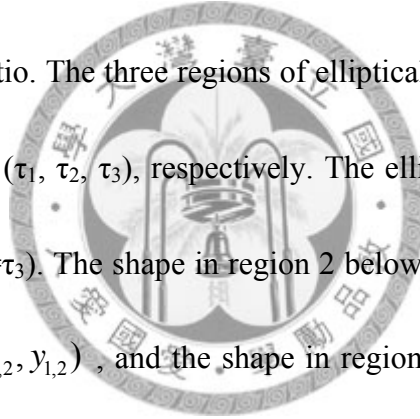
x-direction and y-direction, respectively. The elliptical axis ratio τ is $\frac{L_a}{L_b}$. For example,

the groove parameter for the Rev-HGJB with a groove angle of 32.8° corresponds the

parameter for the Rev-EJGB with an elliptical axis ratio of $1.55 (= \cot 32.8^\circ)$.

The elliptical grooves on the surface of the journal are engraved with three regions. This work varies the bearing length of region 2 (L_2), while the bearing lengths of region 1 (L_1) and region 3 (L_3) are the same. The ellipse has two centers on the groove surface, at the boundary of region 1 and region 2 ($x_{1,2}, y_{1,2}$) and at the boundary of region 2 and region 3 ($x_{2,3}, y_{2,3}$).

After the center of the ellipse is determined, the elliptical shape is obtained by giving the elliptical axis ratio. The three regions of elliptical grooves are of three values of the elliptical axis ratios (τ_1, τ_2, τ_3), respectively. The elliptical axis ratio of region 1 equals that of region 3 ($\tau_1 = \tau_3$). The shape in region 2 below $y=0$ is determined from the center of the ellipse at ($x_{1,2}, y_{1,2}$), and the shape in region 2 above $y=0$ is determined from the center of the ellipse at ($x_{2,3}, y_{2,3}$).



7-2 Validation

Since no study has been done previously to investigate the performance of a Rev-EGJB, either numerically or experimentally, this study validates the Rev-EGJB program based on the numerical results of the Rev-HGJB program. The numerically

determined load capacity for the Rev-HGJB was verified using data from [6]. Fig. 7-2-1 shows that the present numerical results are in good agreement with those in [6]. The differences at the high eccentricity ratio may result from groove discontinuity and the cavitation model [38]. Thus, the numerical program used in this study can be employed to analyze Rev-HGJB performance. In the following, the load capacity of Rev-HGJB is numerically investigated by our program.

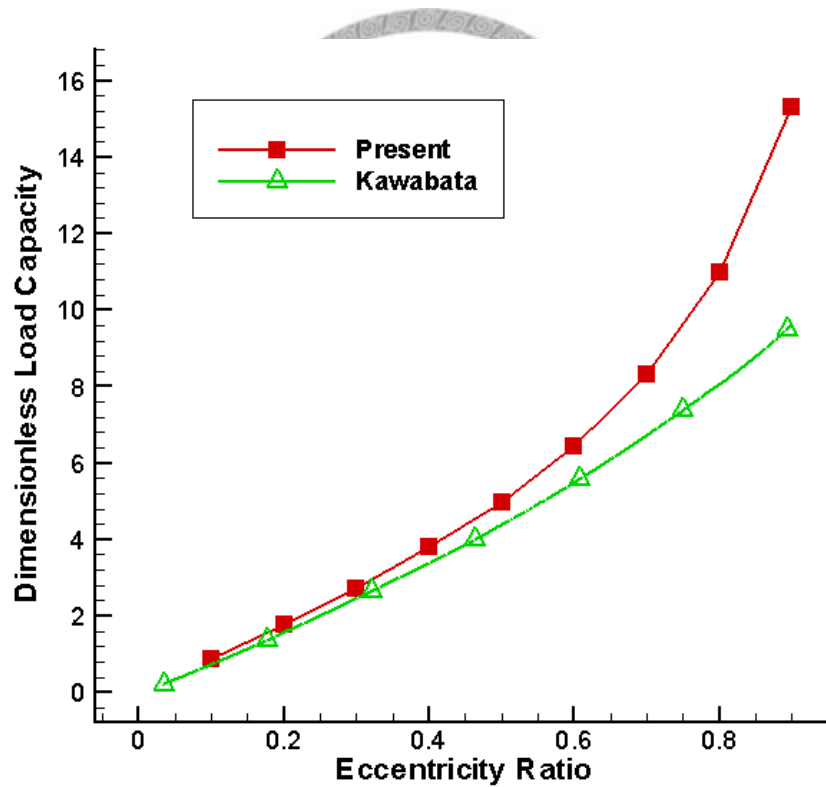
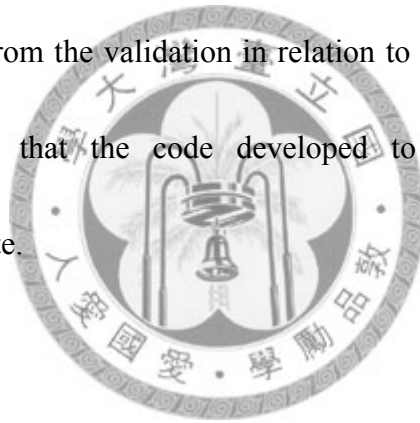


Fig. 7-2-1 The numerical program for the Rev-HGJB was verified using data from [6].

After the numerical program for the Rev-HGJB was validated, the numerical

program of the Rev-EGJB was validated. This study increased the number of the Rev-HGJB's groove sides to asymptotically resemble the elliptical grooves. The details of deriving a groove for eight sides of the Rev-HGJB to resemble the elliptical grooves are found in [36]. Notably, when the number of groove sides increases, the shape of the grooved journal bearing is close to that of an ellipse. Fig. 7-2-2 shows that as the number of groove sides increases, load capacities asymptotically approach that of the Rev-EGJB. In summary, from the validation in relation to the loads of Rev-HGJB and Rev-EGJB, we conclude that the code developed to analyze the Rev-EGJB's performance is also accurate.



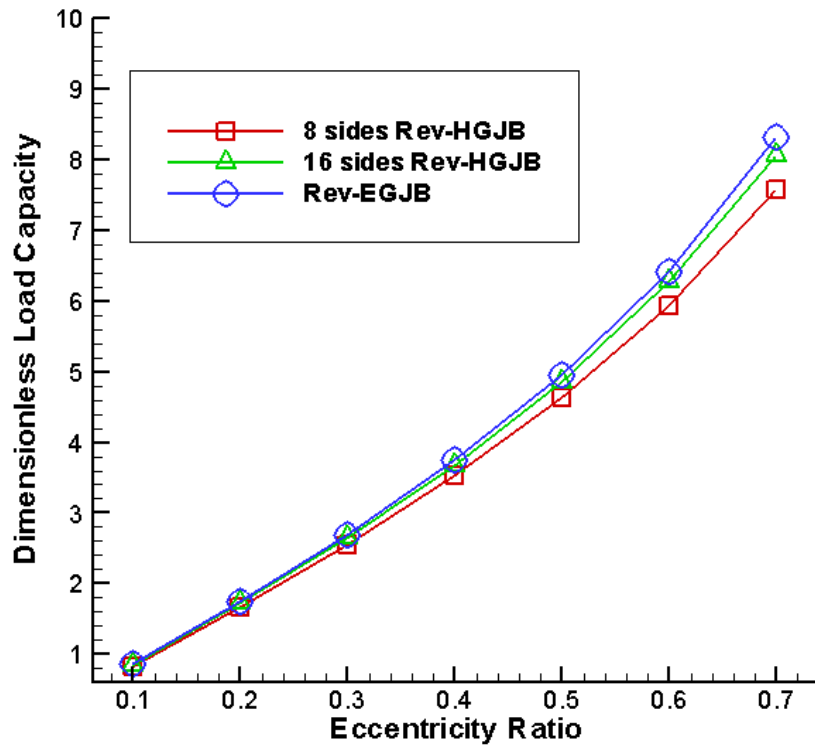


Fig. 7-2-2 The numerical program of the Rev-EGJB was validated by increasing the number of groove sides of the Rev-HGJB.

7-3 Comparison of the Rev-EGJB and the Rev-HGJB

Firstly, the load capacities of the Rev-HGJB and Rev-EGJB are discussed. Then, the pressure distributions on the fluid film are investigated. Finally, the power losses are compared. The bearing parameters in Table 3-3-1 are used; this was applied in reference [6] for the Rev-HGJB.

Table 7-3-1 Parameters of the Rev-GJB (grooved member rotation)

Clearance	6 μm
Radius	0.002 m
Length	0.008 m
Fluid viscosity	0.00124 Pa•s
Number of grooves	8
Groove elliptical axis ratio for Rev-EGJB	1.732
(Groove angle 30 deg for Rev-HGJB)	
Groove depth ratio	1.0
Groove width ratio	0.5
Journal speed	5000 rpm
Bearing length of region 2/ bearing length	0.5

7-3-1 Rev-EGJB Mesh

This work developed numerical codes to evaluate the performance of the Rev-EGJB, and used curvilinear elements to discretize the elliptical grooves. There are 8 grooves on the bearing or journal surface in this work. A simulation was performed with a total of 17 elements in the circumferential direction and 16 elements in the axial direction. Fig. 7-3-1 shows the mesh system used in the program for the Rev-EGJB.

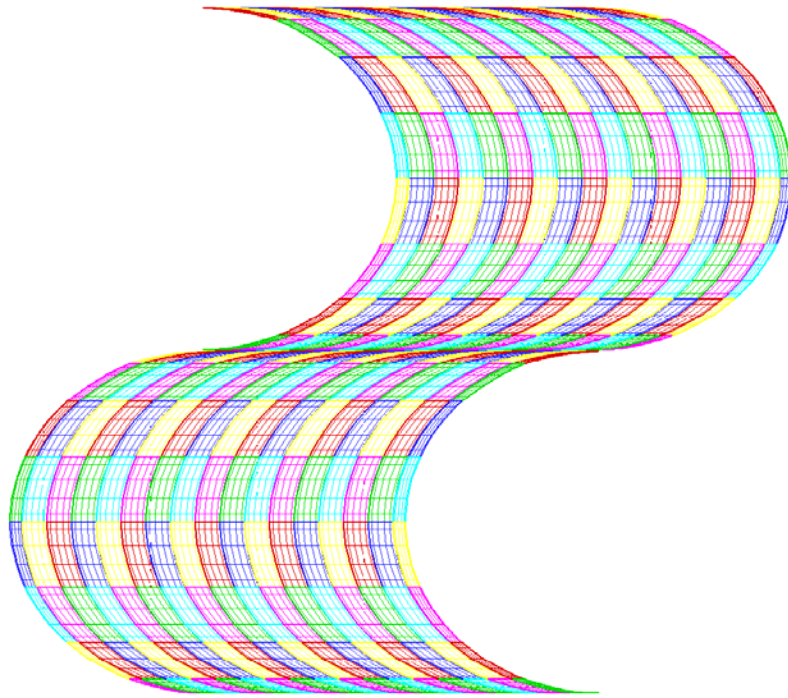


Fig. 7-3-1 The mesh system used in the program for Rev-EGJB

7-3-2 Comparison of the Load Capacities

Fig. 7-3-2 shows the load capacities of the Rev-HGJB and Rev-EGJB with grooved journals for a length-diameter ratio of 1 and 2. It can be seen that the load capacity of the Rev-EGJB does not differ significantly from that of the Rev-HGJB at a low eccentricity ratio, but is consistently greater than that of the Rev-HGJB. Moreover, the larger the length-diameter ratio, the higher the load capacity. This may be because the high pressure region of Rev-EGJB is not markedly larger than that of the Rev-HGJB at a low length-diameter ratio; this is discussed in next section. Hence, the improvements

of adopting the elliptical grooves in the loads of reversible rotation bearings are obvious at a high length-diameter ratio.

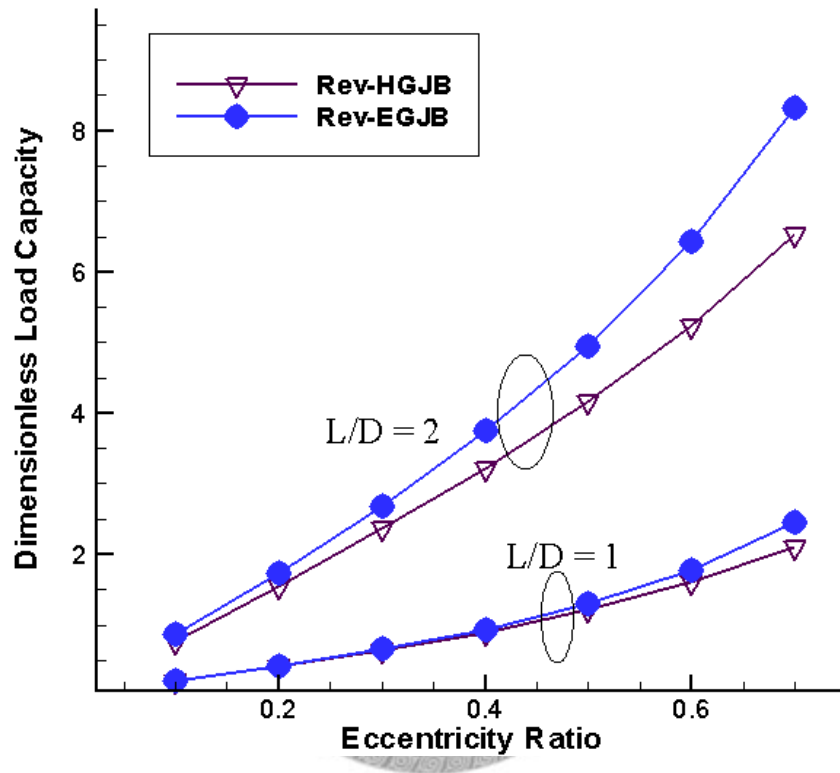
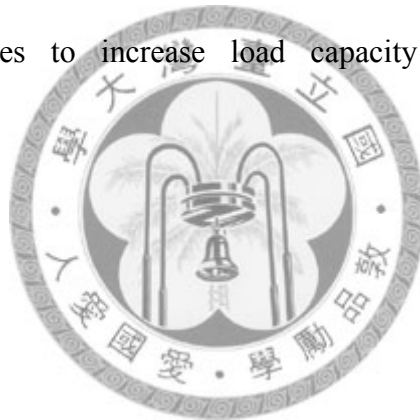


Fig. 7-3-2 Comparison of the load capacities of the conventional HGJB, Rev-HGJB, and Rev-EGJB with the increase of the eccentricity ratio (grooved journal)

The effect of load capacity on the location of grooves on the Rev-HGJB and Rev-EGJB is shown in Fig. 7-3-3. The figure shows that when the bearing is grooved, the load capacity of the Rev-EGJB is about 12-15% greater than that of the Rev-HGJB

at a length-diameter ratio of 2. Comparing the load capacity of the Rev-EGJB with that of Rev-HGJB indicates that the increase in load capacity of the Rev-EGJB with a grooved journal is greater than that of the Rev-EGJB with a grooved bearing. This analytical result is in agreement with those in literature [36]. In summary, this work concludes that more load capacity of the Rev-EGJB than that of Rev-HGJB can be gained no matter where the grooves are located in the bearing or journal. Furthermore, adopting elliptical grooves to increase load capacity is beneficial at a high length-diameter ratio.



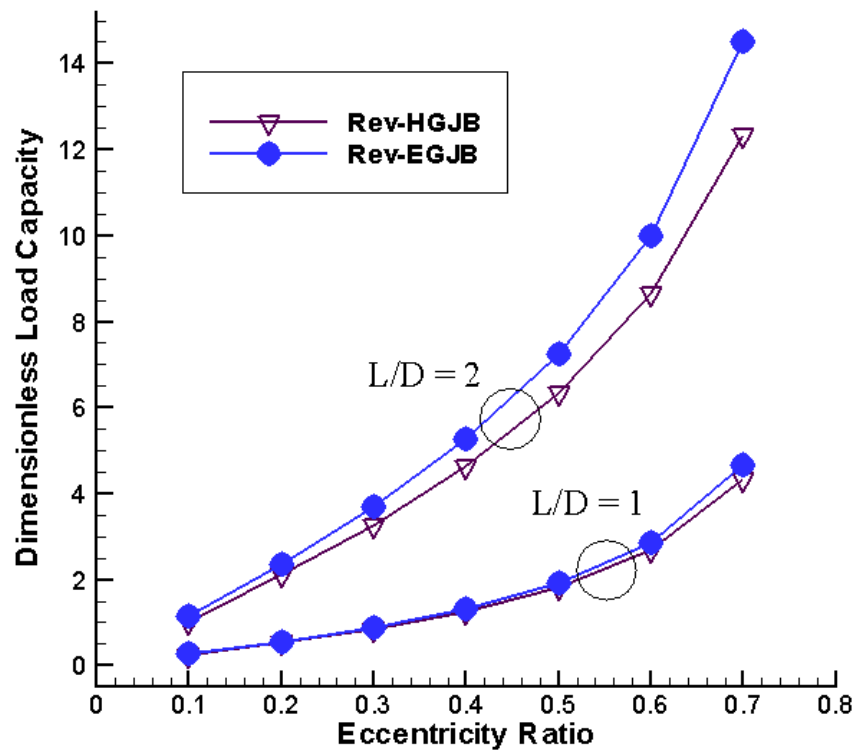


Fig. 7-3-3 The load capacity of the Rev-HGJB and Rev-EGJB with grooved bearing for $L/D = 1, 2$

7-3-3 Comparison of the Pressure Distributions in the Fluid Film

To examine how elliptical grooves profit load characteristics, this work investigates differences in the pressure distributions of fluid film on an Rev-HGJB and Rev-EGJB with the same operating conditions, as shown in Table 1. Fig. 7-3-4 displays the pressure distributions of fluid film. Although the peak pressure in the Rev-HGJB is higher than that in the Rev-EGJB, a larger portion of high pressure is achieved in the pressure-generated region of Rev-EGJB than in that of the Rev-HGJB, since the

elliptical grooves pump more lubricants inward on the bearing than herringbone grooves do. This is similar to the results of a study on the characteristics of EGJBs [36].

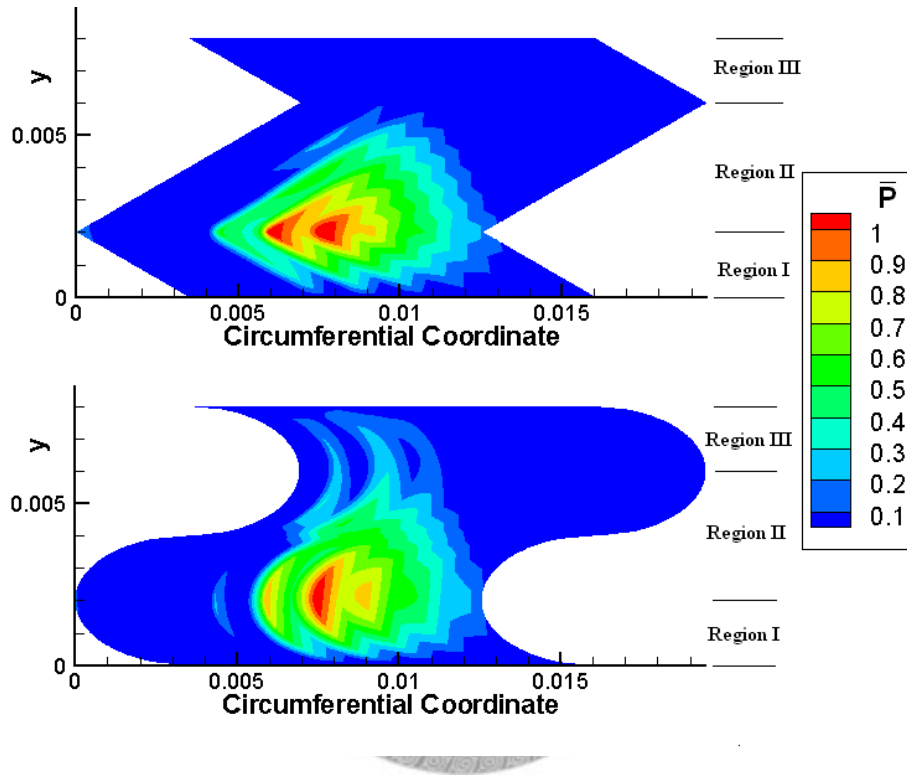


Fig. 7-3-4 The pressure distributions of fluid film of a Rev-EGJB and of a Rev-HGJB under the operating conditions in Fig. 7-3-2 ($\epsilon=0.3$)

Furthermore, a larger high pressure region in Rev-EGJB than that in Rev-HGJB is not only achieved in the pressure-generated region, but also in the pressure-restored region. Notably, the groove shape changes smoothly in the pressure-generated region and pressure-restored region of Rev-EGJB, but that of Rev-HGJB changes abruptly.

Hence, the shape of herringbone is beneficial for the peak pressure, but is not beneficial for the pressure-generated region. In contrast, adopting the elliptical grooves is able to increase the high-pressure area in the fluid film, which contributes to the load of the bearing. Therefore, a high load capacity results from the integration of a large high pressure portion, which can be seen in equation (6), which is for load evaluation.

To understand how the high pressure area contributes to the load, this work investigates differences in the load distributions of fluid film. Fig. 7-3-5 plots the load per unit length along the y direction. The area below the curve is the load capacity of the bearing. The peak of the curve for Rev-HGJB is higher than that for the Rev-EGJB. In contrast, the load of the Rev-HGJB is lower than that of Rev-EGJB, as it is away from the peak of the load curve. Notably, the load in the pressure-restored region of the Rev-EGJB is obviously greater than that in Rev-HGJB, since adopting the elliptical groove increases the pumping effect. Hence, the load of the Rev-EGJB is apparently greater than that of the Rev-HGJB.

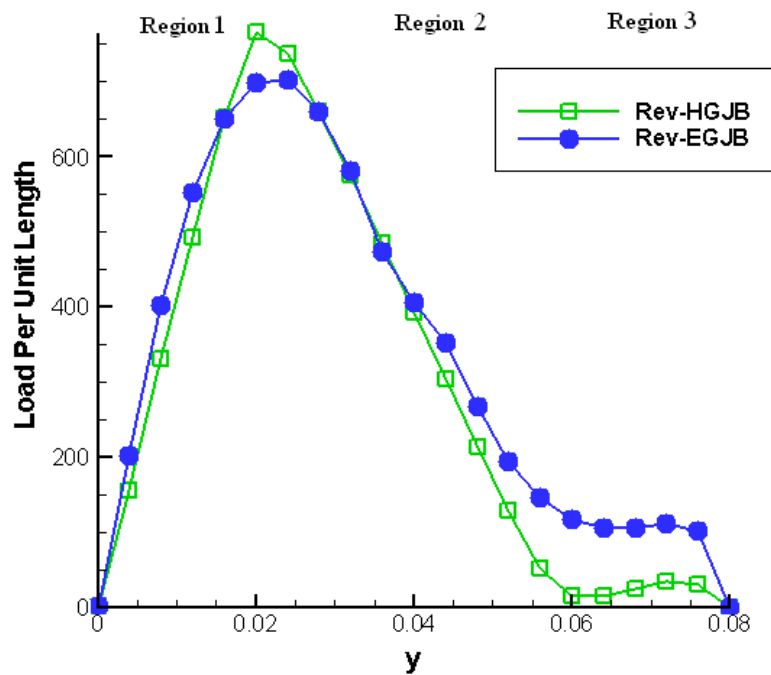


Fig. 7-3-5 The load per unit length along y direction

7-4 Comparison of Power Losses

Power consumption is also an important characteristic for hydrodynamic journal bearings. As shown in Table 2, the power loss of the Rev-EGJB decreases slightly compared to that of the Rev-HGJB. Thus employing the elliptical grooves on reversible rotation bearings causes reduction in the friction in the fluid film, and the power consumption is slightly lower, while the load is enhanced.

Table 7-4-1 Comparison of the power loss of the Rev-HGJB and Rev-EGJB at an eccentricity ratio of 0.1

power loss(W)	Rev-HGJB	Rev-EGJB
groove member rotation	1.62E-02	1.59E-02

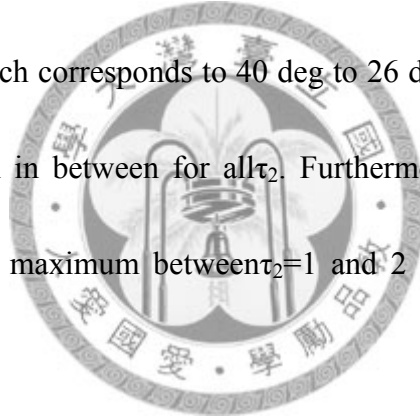
7-5 The Effect of Groove's Appearance on Radial Stiffness

The effects of groove parameters such as the elliptical axis ratio, groove depth ratio, groove width ratio, and length of region 2 on stability are investigated in this section for an eccentricity ratio of 0.1. The groove parametric matrix is given by taking several values in the range of each groove parameter: 7 for an elliptical axis ratio from 0.5 to 2, 9 for a groove width ratio from 0.4 to 0.6, 9 for a groove depth ratio from 0.5 to 2, and 9 for a length of region 2 from 0.4 to 0.6. A total of 35721 cases were used in the groove parametric matrix.

To observe the influence of each groove parameter on stability, only one of the groove parameters is varied while others are fixed. The influence of variations in groove

appearances on stability can be inferred by observing the computed radial stiffness.

Fig. 7-5-1 to Fig. 7-5-4 show the result of the grooved member rotation for $L/D = 2$ and $\varepsilon = 0.1$. To study the effects of the elliptical axis ratio on radial stiffness, the groove elliptical axis ratios of region 1 and region 2, τ_1 and τ_2 , are varied from 0.5 to 2.0, while the groove depth and groove width are fixed at $\Gamma=1.0$ and $\delta=0.5$. Fig. 7-5-1 shows that dimensionless radial stiffness varies less when the elliptical axis ratio of region 1, τ_1 , changes from 1.2 to 2, which corresponds to 40 deg to 26 deg of a herringbone groove, and reaches the maximum in between for all τ_2 . Furthermore, it can be seen that the radial stiffness reaches its maximum between $\tau_2=1$ and 2 when τ_1 is fixed to a value below 2.



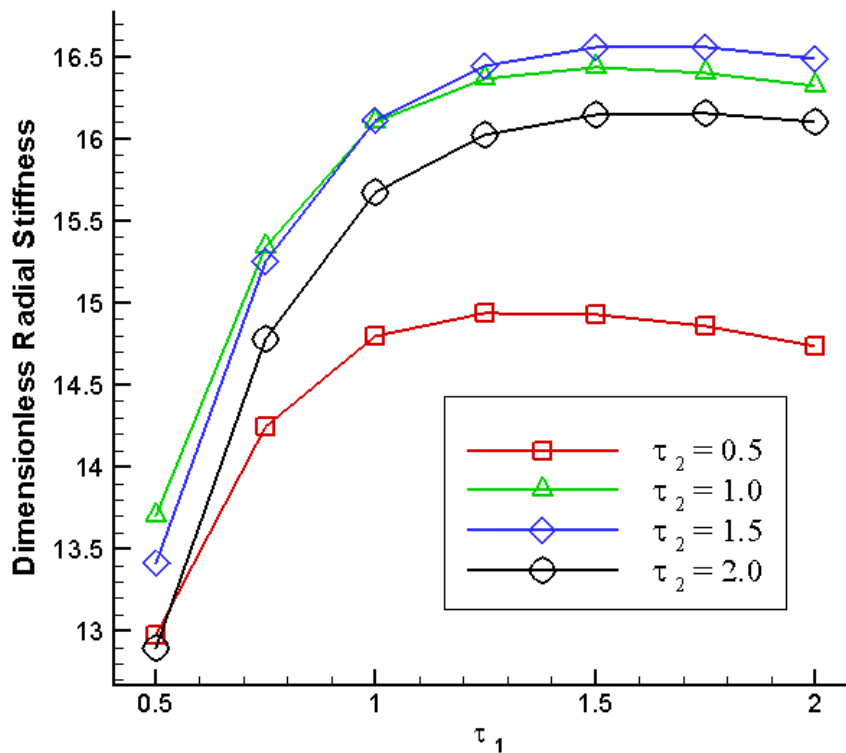


Fig. 7-5-1 The influences of elliptical axis ratio of region 1 and region 2 on dimensionless radial stiffness

To study the influences of groove depth on dimensionless radial stiffness, the groove depth ratio is increased from 0.5 to 2.0, while the groove elliptical axis ratio and groove width are fixed at $\tau_1 = \tau_2 = 1.0$ and $\delta = 0.5$. Fig. 7-5-2 shows that the dimensionless radial stiffness reaches a peak value at $\Gamma = 1$ to 1.5 for all cases.

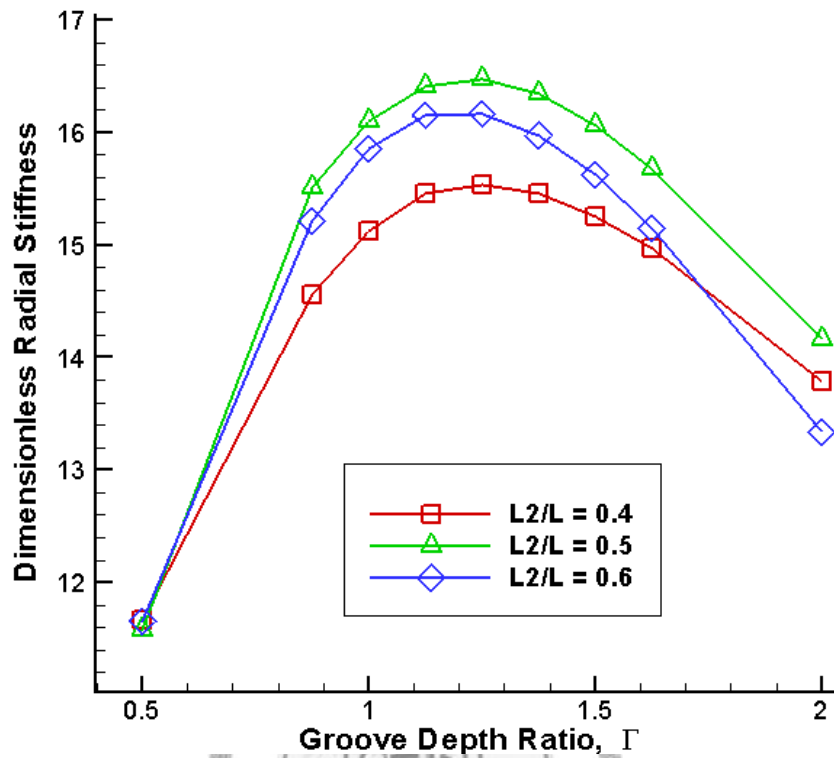


Fig. 7-5-2 The influences of groove depth on dimensionless radial stiffness

To study the effects of groove width on dimensionless radial stiffness, the groove width ratio is increased from 0.4 to 0.6, while the groove elliptical axis ratio and groove depth are fixed at $\tau_1 = \tau_2 = 1.0$ and $\Gamma = 1.0$. Fig. 7-5-3 shows that groove width has little effect on dimensionless radial stiffness when the groove width ratio is less than 0.5, but radial stiffness decreases when the groove width ratio exceeds 0.5. It can also be seen that dimensionless radial stiffness is greater when the length of region 2 is larger than about half of the bearing length.

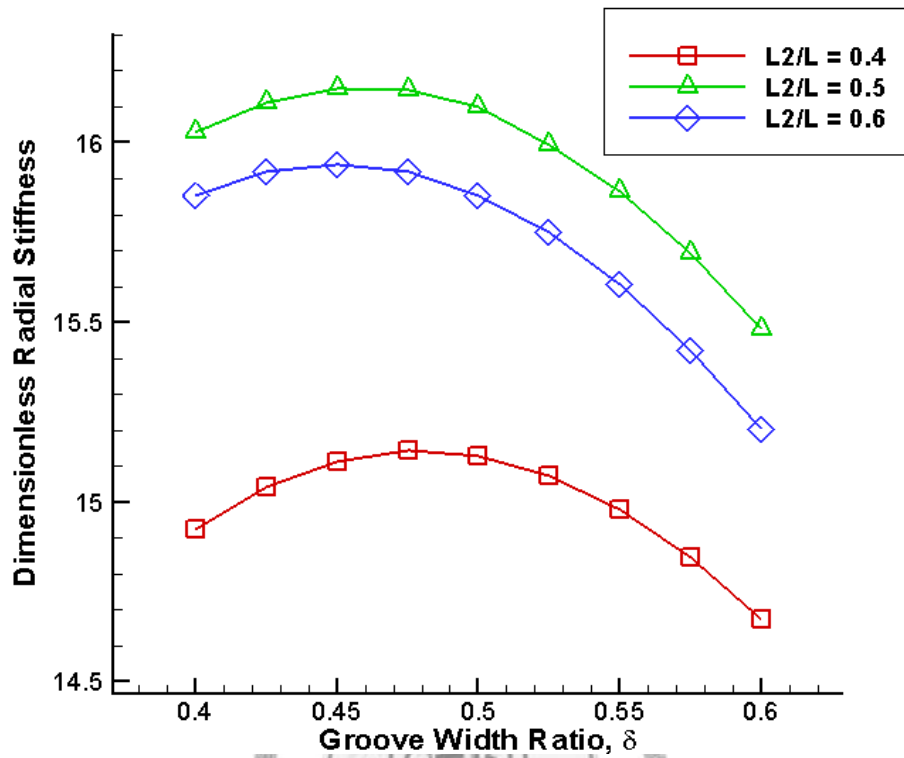


Fig. 7-5-3 The effects of groove width on dimensionless radial stiffness

To study the influences of the length of region 2 on dimensionless radial stiffness, the length of region 2 is increased from $0.4L$ to $0.6L$, while the groove elliptical axis ratio, groove depth, and groove width are fixed at $\tau_1 = \tau_2 = 0.5, 1.0, 1.5$, and 2.0 , $\delta = 0.5$, and $\Gamma = 1.0$. Fig. 7-5-4 shows that the dimensionless radial stiffness reaches a peak at $L_2 = 0.45L$ to $0.55L$ for all cases.

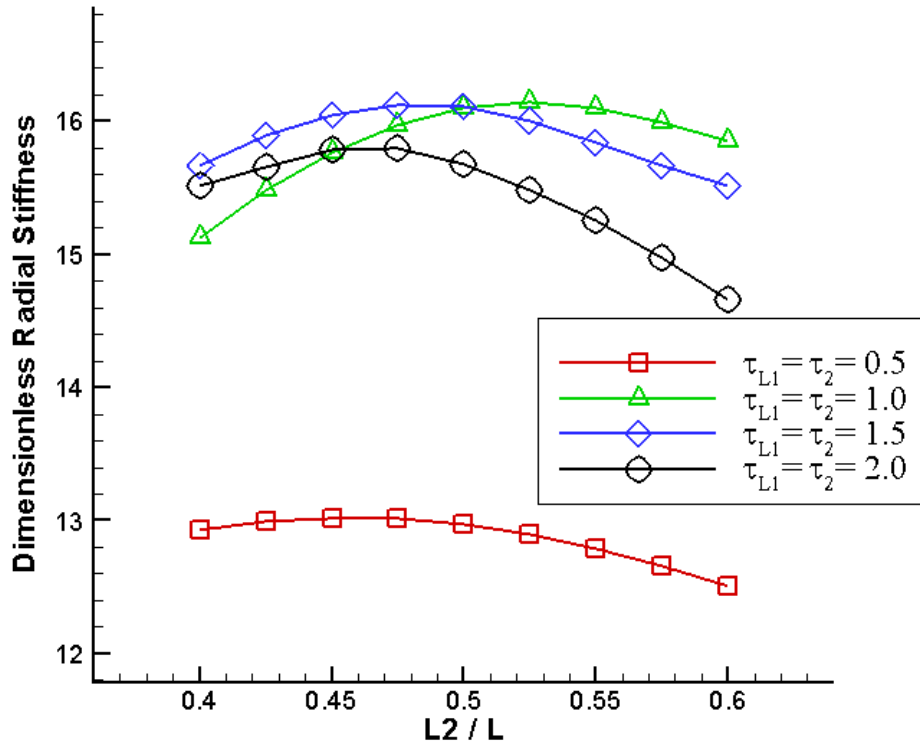


Fig. 7-5-4 The effect of bearing length of region 2 on dimensionless radial stiffness



7-6 The Optimum Parameters of Rev-EGJB for Stability

From the parametric study, the values of the optimum groove parameters, given in Table 3, for the Rev-EGJB to reach the maximum radial force, are a groove width ratio of 0.4, groove depth ratio of 1.5, $L_2/L = 0.575$, and elliptical axis ratio of $\tau_1 = \tau_3 = 2$, $\tau_2 = 1.25$. These optimum groove parameters are different from those obtained by Kawabata *et al.*[6]. The radial stiffness of the Rev-EGJB compared with that of the

Rev-HGJB with the optimum geometry is also shown in Table 7-6-1. It can be seen that the radial stiffness of the Rev-EGJB does not differ markedly from that of the Rev-HGJB. Moreover, for the grooved bearing, the Rev-EGJB is more stable than the Rev-HGJB. The optimum groove parameter values for the Rev-EGJB to reach the maximum radial force are a groove width ratio of 0.575, groove depth ratio of 1.625, $L_2/L = 0.425$, and elliptical axis ratio of $\tau_1=\tau_3=1.0$, $\tau_2=2.0$.

Table 7-6-1 the values of the optimum groove parameters

	grooved journal		grooved bearing	
	Rev-EGJB	Rev-HGJB	Rev-EGJB	Rev-HGJB
Length of Region 2, L_2/L	0.575	0.467	0.425	0.48
Groove depth ratio, Γ	1.5	1.034	1.625	1.068
Groove width ratio, δ	0.4	0.5	0.575	0.5
elliptical axis ratio, $\tau_1=\tau_3$ or groove angle (deg) of region 1 and 3	2	32.18	1.0	148.75
elliptical axis ratio, τ_2 or groove angle (deg) of region 2	1.25	43.09	2.0	135.31
dimensionless radial stiffness	18.7	19.1	10.6	9.1



8. Conclusions

This work developed a numerical program for analyzing the characteristics of the grooved journal bearing. Then a novel elliptical groove is proposed to enhance the performance of the hydrodynamic journal bearing. The conclusions are drawn as follows:

1. The Reynolds equation was solved using the SEM in order to obtain the distribution of pressure in the fluid film. The groove-ridge discontinuity is treated by conservation of mass. It can be shown that the present method can be applied to correctly determine the pressure distribution of the fluid film. Furthermore, employing the present method and incorporating the Elrod's algorithm can improve the accuracy of evaluating loads of HGJBs when cavitation occurs.
2. The performances of the EGJB are superior to that of the HGJB due to the high load capacity, high radial stiffness, and low side leakage of lubricants. For the EGJB, groove parameters can be set at maximum radial force of EGJB. These values are a groove width ratio of 0.5, groove depth ratio of 2.0, and elliptical axis ratio of 1.5. These optimum groove parameters are similar to those obtained by

Vohr and Chow [29].

3. The load distribution of EGJB along the axial direction is more uniform than that of HGJB. The low load at the bearing center of EGJB may be offset by the load away from the bearing center; thus, a higher load capacity for the EGJB than that of HGJB is achieved.
4. Adopting the elliptical grooves on reversible rotation journal bearings can enhance the pumping effect to a greater extent than adopting herringbone grooves. The performance of the Rev-EGJB is superior to that of the Rev-HGJB due to its high load capacity and slight low-power loss.
5. Observing the load distribution along the axial direction, the lower peak load of Rev-EGJB than that of Rev-HGJB may be offset by the load away from the lower peak load. In addition, the load in the pressure-restored region of the Rev-EGJB is obviously greater than that in the Rev-HGJB. Thus, a higher load capacity is achieved for the Rev-EGJB than that of the Rev-HGJB.
6. The Rev-EGJB is also more stable than the Rev-HGJB.

9. Future Work

1. The loads evaluated are more accurate when cavitation occurs, which may result from the consideration of conservation of mass at the groove-ridge region and at the cavitation inception concurrently by Elrod's algorithm. Further investigation is needed to understand this coupling effect.
2. The oil inlet conditions are also important parameters to affect the bearing pressure and cavitation region[39], and should be further investigated.
3. The effect of temperature of the lubricant on the characteristics of the bearings may be more significant than that of the HGJB due to less leakage, and should be further investigated.
4. The enhancements of elliptical grooves on air journal bearings and elastohydrodynamic journal bearings are warranted.
5. The critical mass incorporates to Elrod's algorithm is needed to derive as by the small perturbation to Elrod's Universal Equation.
6. The performances of the EGJB and the Rev-EGJB can be verified experimentally

using a prototype spindle motor built in the laboratory.



References

1. Asada T, Saito H, Asaida Y, Itoh K. Design of hydrodynamic bearings for high-speed hdd. *Microsystem Technologies* 2002; 8(2-3): 220-226.
2. Liu CS, Lin PD, Tsai MC. A miniature spindle motor with fluid dynamic bearings for portable storage device applications. *Microsystem Technologies* 2009; 15(7): 1001-1007.
3. Ohmi T. Non-repeatable runout of ball-bearing spindle-motor for 2.5 double prime hdd. *IEEE Transactions on Magnetics* 1996; 32(3-2): 1715-1720.
4. Chao PCP, Huang JS. Calculating rotordynamic coefficients of a ferrofluid-lubricated and herringbone-grooved journal bearing via finite difference analysis. *Tribology Letters* 2005; 19(2): 99-109.
5. Muijderland EA. Grease-lubricated spiral groove bearings. *Tribology international* 1979; 12: 131-137.
6. Kawabata N, Ozawa Y, Kamaya S, Miyake Y. Static characteristics of the regular and reversible rotation type herringbone grooved journal bearing. *Journal of Tribology, Transactions of the ASME* 1989; 111(3): 484-490.
7. Zhang QD, Winoto SH, Chen SX, Yang JP. A bi-directional rotating fluid bearing system. *Microsystem Technologies* 2002; 8(2002): 271-277.
8. Junmei W, Jiankang W, Lee TS, Shu C. A numerical study of cavitation foot-prints in liquid-lubricated asymmetrical herringbone grooved journal bearings. *International Journal of Numerical Methods for Heat and Fluid Flow* 2002; 12(5): 518-540.
9. Leuthold H, Jennings DJ, Nagarathnam L, Grantz A, Parsoneault S. Sinusoidal grooving pattern for grooved journal bearing. 1999: U. S. Patent 5,908,247.
10. Liu CS, Tsai MC, Yen RH, Lin PD, Chen CY. Analysis and validations of a novel hydrodynamic grooved journal bearing. *Journal of Chinese Society of Mechanical Engineers*: (submitted, in revise).
11. Kang K, Rhim Y, Sung K. A study of the oil-lubricated herringbone-grooved journal

bearing-part 1: Numerical analysis. *Journal of Tribology, Transactions of the ASME* 1996; 118(4): 906-911.

12. Gad AM, Nemat-Alla MM, Khalil AA, Nasr AM. On the optimum groove geometry for herringbone grooved journal bearings. *Journal of Tribology, Transactions of the ASME* 2006; 128(3): 585-593.

13. Kirk RG, Gunter EJ. Stability and transient motion of a plain journal mounted in flexible damped supports. *Journal of Engineering for Industry-Transactions of the ASME* 1976; 98(2): 576-592.

14. Lund JW. Review of the concept of dynamic coefficients for fluid film journal bearings. *Journal of Tribology, Transactions of the ASME* 1987; 109(1): 37-41.

15. Bonneau D, Absi J. Analysis of aerodynamic journal bearings with small number of herringbone grooves by finite element method. *Journal of Tribology, Transactions of the ASME* 1994; 116(4): 698-704.

16. Zirkelback N, San Andrés L. Finite element analysis of herringbone groove journal bearings: A parametric study. *Journal of Tribology, Transactions of the ASME* 1998; 120(2): 234-240.

17. Rao TVVLN, Sawicki JT. Stability characteristics of herringbone grooved journal bearings incorporating cavitation effects. *Journal of Tribology, Transactions of the ASME* 2004; 126(2): 281-287.

18. Jakobsson B, Floberg L. The finite journal bearing considering vaporization. *Charmers Tekniska Hoegskolas Handlingar* 1957; 190: 1-116.

19. Lee TS, Liu YG, Winoto SH. Analysis of liquid-lubricated herringbone grooved journal bearings. *International Journal of Numerical Methods for Heat and Fluid Flow* 2004; 14(3): 341-365.

20. Jang GH, Chang DI. Analysis of a hydrodynamic herringbone grooved journal bearing considering cavitation. *Journal of Tribology, Transactions of the ASME* 2000; 122(1): 103-109.

21. Patera AT. A spectral element method for fluid dynamics: Laminar flow in a channel expansion. *Journal of Computational Physics* 1984; 54: 468-488.

22. Korczak KZ, Patera AT. An isoparametric spectral element method for solution of the navier-stokes equations in complex geometry. *Journal of Computational Physics* 1986; 62: 361-382.
23. Schneidesch CR, Deville MO. Chebyshev collocation method and multi-domain decomposition for navier-stokes equations in complex curved geometries. *Journal of Computational Physics* 1993; 106: 234-257.
24. Gordon WJ, Hal CA. Transfinite element methods: Blending-function interpolation over arbitrary curved element domains. *Numerische Mathematik* 1973; 21(2): 109-129.
25. Karniadakis GE. Spectral element simulations of laminar and turbulent flows in complex geometries. *Applied Numerical Mathematics* 1989; 6: 85-105.
26. Gerritsma M, van der Bas R, De Maerschalck B, Koren B, Deconinck H. Least-squares spectral element method applied to the euler equations. *International Journal for Numerical Methods in Fluids* 2008; 57(9): 1371-1395.
27. Stiller J, Fladrich U. Factorization techniques for nodal spectral elements in curved domains. *SIAM Journal on Scientific Computing* 2008; 30(5): 2286-2301.
28. Kopriva DA. Metric identities and the discontinuous spectral element method on curvilinear meshes. *Journal of Scientific Computing* 2006; 26(3): 301-327.
29. Vohr JH, Chow CY. Characteristics of herringbone grooved gas lubricated journal bearings. *Journal of Basic Engineering* 1965; 87: 568-578.
30. Faria MTC. Some performance characteristics of high speed gas lubricated herringbone groove journal bearings. *JSME International Journal, Series C* 2001; 44(3): 775-781.
31. Arghir M, Alsayed A, Nicolas D. The finite volume solution of the reynolds equation of lubrication with film discontinuities. *International Journal of Mechanical Sciences* 2002; 44(10): 2119-2132.
32. Hernandez P, Boudet R. Modelling of the behavior of dynamical gas seals: Calculation with a finite element method implicitly assuring the continuity of flow. *Proceedings of the Institution of Mechanical Engineers, Part J: Journal of Engineering Tribology* 1995; 209(3): 195-201.

33. Hirayama T, Sakurai T, Yabe H. A theoretical analysis considering cavitation occurrence in oil-lubricated spiral-grooved journal bearings with experimental verification. *Journal of Tribology, Transactions of the ASME* 2004; 126(3): 490-498.
34. Elrod HG. A cavitation algorithm. *ASME Journal of Lubrication Technology* 1981; 103: 350-354.
35. Hamrock BJ, *Fundamentals of fluid film lubrication*. McGraw-Hill, 1994.
36. Yen RH, Chen CY. Enhancement of journal bearings characteristics using a novel elliptical grooves. *Proceedings of the Institution of Mechanical Engineers, Part J Journal of Engineering Tribology* 2009: in press.
37. Hirs GG. The load capacity and stability characteristics of hydrodynamic grooved journal bearings. *ASLE Transactions* 1965; 8: 296-305.
38. Chen CY, Yen RH, Chang CC. Spectral element analysis of herringbone grooved journal bearings with groove-ridge discontinuity. *International Journal for Numerical Methods in Fluids* 2010: in press.
39. Wang JK, Khonsari MM. Effects of oil inlet pressure and inlet position of axially grooved infinitely long journal bearings. Part i: Analytical solutions and static performance. *Tribology international* 2008; 41: 119-131.

Appendix A Evaluation of Dimensionless Critical Mass

When the journal position is changed slightly from the equilibrium state by the excitation force, the journal vibration may increase and result in instability. Based on the assumption that a small reaction occurs in the equilibrium state, the pressure and the thickness of the fluid film can be expressed as first-order functions of a small perturbation, as follows:

$$p = p_0 + p_x \Delta x + p_z \Delta z + p_{\dot{x}} \Delta \dot{x} + p_{\dot{z}} \Delta \dot{z} \quad (\text{A1})$$

$$h = h_0 + \Delta x \cos \phi + \Delta z \cos \phi \quad (\text{A2})$$

Substituting Eqs. (A1) and (A2) into Eq. (2-1) yields the changes in the pressure of the journal close to an equilibrium position:

$$\begin{aligned} & \frac{1}{r^2} \frac{\partial}{\partial \phi} \left[\frac{(h_0 + \Delta x \cos \phi + \Delta z \cos \phi)^3}{12\mu} \frac{\partial(p_0 + p_x \Delta x + p_z \Delta z + p_{\dot{x}} \Delta \dot{x} + p_{\dot{z}} \Delta \dot{z})}{\partial \phi} \right] \\ & + \frac{\partial}{\partial y} \left[\frac{(h_0 + \Delta x \cos \phi + \Delta z \cos \phi)^3}{12\mu} \frac{\partial(p_0 + p_x \Delta x + p_z \Delta z + p_{\dot{x}} \Delta \dot{x} + p_{\dot{z}} \Delta \dot{z})}{\partial y} \right] \quad (\text{A3}) \\ & = \frac{\omega}{2} \frac{\partial(h_0 + \Delta x \cos \phi + \Delta z \cos \phi)}{\partial \phi} + \Delta \dot{x} \cos \phi + \Delta \dot{z} \cos \phi \end{aligned}$$

Once the perturbation pressure is known, dynamic coefficients can be calculated by integrating the pressure over the bearing area [35]. For example, the non-dimensional coefficient K_{xx} can be obtained using:

$$K_{xx} = \frac{c}{W} \int_y \int_\phi p_x \cos \phi r dy d\phi \quad (\text{A4})$$

The perturbation pressure p_x is determined by collecting the terms of $O(\Delta x)$ in

Eq. (A3):

$$\begin{aligned} \frac{1}{r^2} \frac{\partial}{\partial \phi} \left[\frac{h_0^3}{12\mu} \frac{\partial p_x}{\partial \phi} \right] + \frac{\partial}{\partial y} \left[\frac{h_0^3}{12\mu} \frac{\partial p_x}{\partial y} \right] = \\ -\frac{\omega}{2} \left(\sin \phi + \frac{3 \cos \phi}{h_0} \frac{\partial h_0}{\partial \phi} \right) - \frac{h_0^3}{4\mu r^2} \frac{\partial p_0}{\partial \phi} \frac{\partial}{\partial \phi} \left(\frac{\cos \phi}{h_0} \right) \end{aligned} \quad (\text{A5})$$

Notably, the linear perturbation equation, Eq. (A5), is similar to the Reynolds equation, Eq. (2-1), so the code developed for the equilibrium state can be directly applied.

The dimensionless critical mass is derived from the eigenvalue for “threshold of instability“ of the equation of motion [14]:

$$M_{cr} = \frac{\kappa_0}{\omega_0^2} \quad (\text{A6})$$

$$\text{with } \omega_0^2 = \frac{(K_{xx} - \kappa_0)(K_{zz} - \kappa_0) - K_{xz}K_{zx}}{D_{xx}D_{zz} - D_{xz}D_{zx}} \quad (\text{A7})$$

$$\text{and } \kappa_0 = \frac{K_{xx}D_{zz} + K_{zz}D_{xx} - K_{xz}D_{zx} - K_{zx}D_{xz}}{D_{xx} + D_{zz}} \quad (\text{A8})$$

